Numerical simulation of the shallow water equations coupled with a precipitation system driven by random forcing

Philip James Andrew Townsend

Department of Mathematics, University of Sussex

Thesis submitted for the Degree of Doctor of Philosophy

May 2018

Abstract

Quantification of flood risk and flood inundation requires accurate numerical simulations, both in terms of the mathematical theory that underpins the methods used and the manner in which the meteorological phenomena that cause flooding are coupled to such systems. Through our research, we have demonstrated how rainfall and infiltration effects can be incorporated into existing flood models in a rigorous and mathematically consistent manner; this approach departs from preceding methods, which neglect terms representing such phenomena in the conservation or balancing of momentum. We demonstrate how the omission of these terms means the solution derived from such models cannot a priori be assumed to be the correct one, which is in contrast to solutions from the extended system we have developed which respect the energetic consistency of the problem.

The second issue we address is determining how we can model these meteorological phenomena that lead to flooding, with a specific interest in how existing observation data from rain gauges can be incorporated into our modelling approach. To capture the random nature of the precipitation, we use stochastic processes to model the complex meteorological interactions, and demonstrate how an accurate representation of the precipitation can be built. Given the specific industrial applications we have mind in regards to flood modelling and prediction, there will be a high computational cost associated with any such simulations, and so we consider techniques which can be used to reduce the computational cost whilst maintaining the accuracy of our solutions. Having such an accurate flood model, coupled with a stochastic weather model designed for efficient computational modelling, will enable us to make useful predictions on how future climate change and weather patterns will impact flood risk and flood damage.

Declaration

I declare that this thesis has been composed by myself and that the work has not been submitted for any other degree or professional qualification. I confirm that the work submitted is my own, except where work which has formed part of jointly-authored publications has been included. My contribution and those of the other authors to this work have been explicitly indicated below. I confirm that appropriate credit has been given within this thesis where reference has been made to the work of others.

The work presented in Chapters 3 and 4 was previously published on arXiv[1] as *A Saint-Venant shallow water model for overland flows with precipitation and recharge* by Mehmet Ersoy, Omar Lakkis (supervisor), and Philip Townsend (student and author of declaration). This study was conceived by all of the authors, and I, the student, contributed to development of the Navier-Stokes boundary conditions; derivation of the extended shallow water system through vertical averaging; derivation of the extended shallow water theorem; formulation of the kinetic scheme; and numerical testing of the model.

Signed .....

[1] Available at `arxiv.org/abs/1705.05470`

Acknowledgements

This work would not have been possible without the financial support of the Engineering and Physical Sciences Research Council (EPSRC) or Ambiental Technical Solutions Ltd. through their joint CASE studentship. I would particularly like to thank Dr. Justin Butler and David Martin, Managing Director and Technical Director, respectively, of Ambiental for their support, assistance, and input during my studies. I am also thankful to all those I worked with during my time at Ambiental for making me feel welcome.

I am grateful to all those with whom I have had the pleasure of working with during this project. I would especially like to thank my supervisor, Dr. Omar Lakkis, who has provided me with extensive personal and professional guidance; it has been a pleasure to work side-by-side with him and he has taught me more than I can credit him for during our time together. I would also like to thank my second supervisors, Prof. Martin Todd and Prof. Charalambos Makridakis, whose knowledge and expertise have been invaluable in determining the direction of my research.

The support of my family has been paramount during my studies and I would not be where I am without their help and guidance. I can never thank them enough for all they have done for me.

Contents

Chapter 1

Introduction

A review by the World Resource Institute (WRI) in 2014 ranked 163 countries by the average size of their population affected annually by river flooding [Luo et al., 2015]. The United Kingdom was ranked 61st, with an average of 24,670 people affected each year; this was far below the United States, ranked 18th with 167,210 people, and 1st placed India, with 4.8 million people.

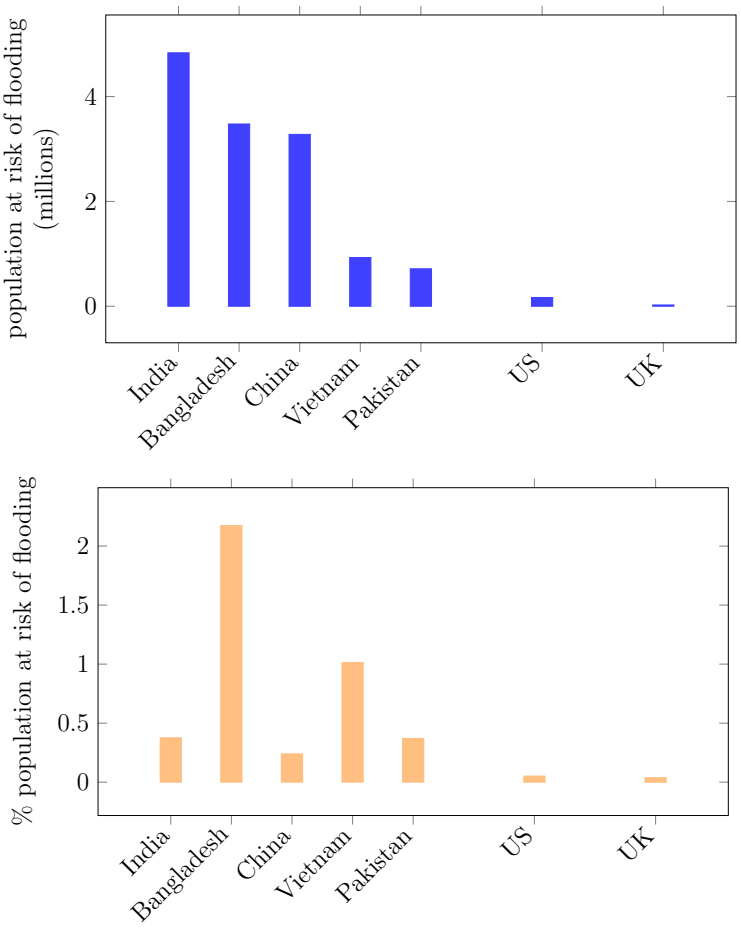

Figure 1.1: Top 5 ranked countries by population affected by river flooding, together with the US and UK.

With the UK ranked so comparatively low on the global flood risk scale (both by raw figures and % of population, as shown in Figure 1.1), we might ask why it is worth considering questions regarding flood risk, flood defences, and flood modelling in the UK. The answer to this question can be addressed as follows:

- the WRI ranking was based on an assumed 100-year flood protection level across the entire UK
- climate change projections suggest extreme flood events will become more common, and thus the return period afforded by the protection will decrease
- spending on flood defences has not increased consistently year-on-year and is not determined on a long-term basis

Therefore, while the UK might be comparatively well-placed on the global flood risk scale now, with climate change leading to more and more extreme flood events there is significant uncertainty on whether it can consistently maintain the level of defence required.

1.1 Flood risk in the UK

The average annual cost of flooding in the UK is around £1.1bn, but the flood risk landscape in the UK has undergone a large shift in recent years: in the summer of 2007, flooding caused £3.2bn of damage, and winter flooding in 2013-14 and 2015-16 caused £1-£1.5bn and £5-£5.8bn of damage, respectively. Figures from Priestley and Rutherford [2017] suggest that approximately 1-in-6 properties in England (around 5.4m) are considered at risk from river, sea, or surface water flooding:[1]

- 2.4 million properties are at risk of flooding from rivers or the sea
- 3 million properties are susceptible to surface water flooding
- 0.6 million properties are at risk of river, sea, and surface flooding

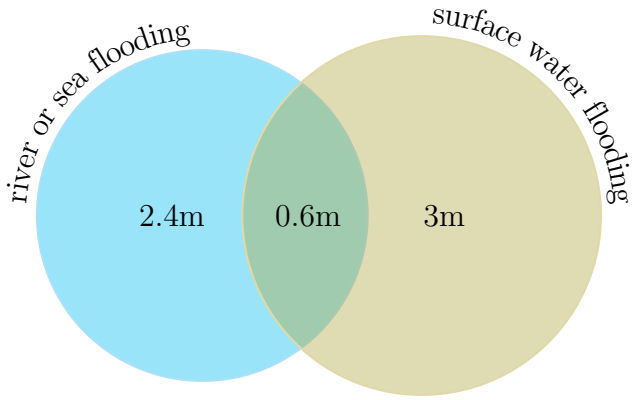

Figure 1.2: Venn diagram of the number of UK properties at risk from flooding.

[1]The WRI figures quoted above represent the number of people in the UK *affected* on average each year by river flooding, while the 1-in-6 figure quoted here represents the number of properties *at risk*; of those properties at risk of flooding, only some will be affected in any one year.

However, these figures are not predicted to remain unchanged. Projections suggest that in 2035 around 1-in-2 properties could be at risk of flooding, with annual flood damage costs potentially rising to as much as £27bn by 2080 [Bennett and Hartwell-Naguib, 2014].

1.2 Flood defence expenditure

As high intensity flood events can result in widespread damage, both in terms of loss of life and destruction to property, significant amounts of government spending is allocated to try and reduce their impact.

As shown below in Figure 1.3, spending on flood defences increased annually from 2007-08 to 2010-11, before falling in real terms by 15.68% for the 2011-12 period. Real terms spending remained reasonably flat for the next two years before increasing sharply in 2014-15 following the 2013-14 winter flooding. Spending for the 2016-17 period is around the levels seen in 2010-11, but remains 9.77% below the peak value [Priestley and Rutherford, 2017].

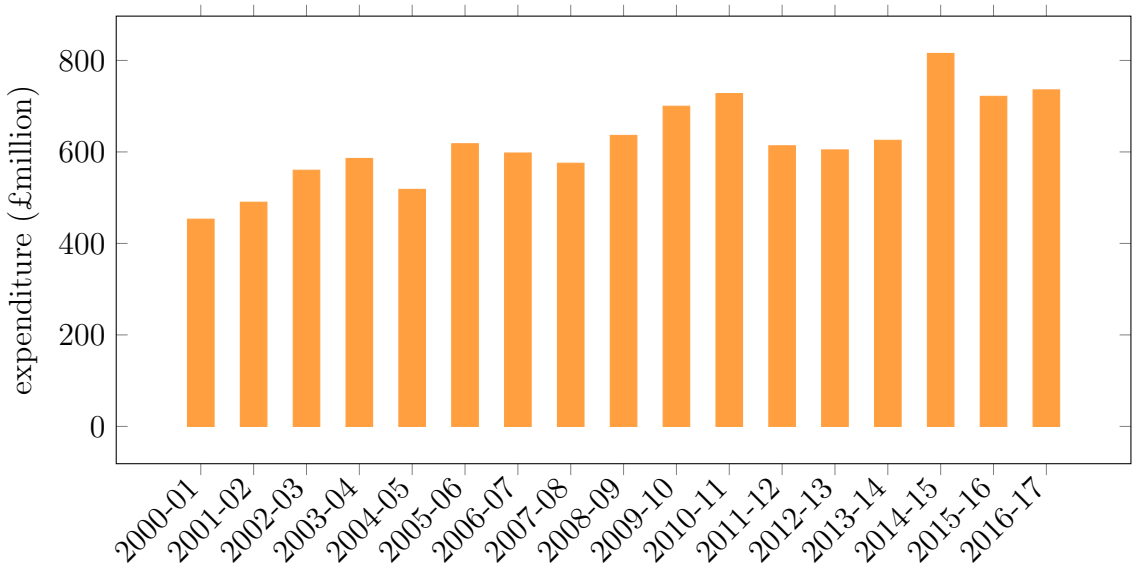

Figure 1.3: UK flood defence expenditure from 2000 - 2017 (given according to 2016-17 prices).

Whether this level of spending is adequate, and in particular whether the year on year increase is sufficient to simply maintain current defences, remains a contentious issue. The government has defended their flood defence policy and total flood defence expenditure did increase for the five year period under the 2010 Coalition government compared to the previous five years; it is worth noting, however, that expenditure was originally set to decrease and the increase was only due to additional funding provided following the 2013-14 winter floods.

1.3 The impact of climate change

In 2017, the UK government published the *Climate Change Risk Assessment* report in which they looked at the predictions of global temperature increases due to climate change and how it would impact the country [Sayers et al., 2015, CCRA, 2017]. Since 1880, global temperatures have increased by 0.85°C (which is consistent with observed temperature increases in the UK) and 14 of the 16 warmest years on record have occurred since the turn of the century. Attempts to curb this temperature increase were put forward in the *Paris Climate Agreement*, which endeavours to limit the increase to 2°C; predictions suggest, however, that without changes being made current policies will lead to at least a 2.7°C rise.

For the UK, the greatest climate change related threats will come from increases in flood risk; as the temperature increases, the atmosphere becomes warmer and it is able to hold more moisture, leading to heavier rainfall (see Table 1.1) and more frequent flooding.

Table 1.1: Increase in intense short-duration (less than 6hrs) rainfall under the three climate change scenarios [Sayers et al., 2015, p. 40].

Climate change scenario	**Temp. increase**	**2020s**	**2050s**	**2080s**
L	2°C	0	10%	20%
M	4°C	10%	20%	50%
H	> 4°C	17%	35%	70%

These increases in rainfall will also have an impact on the number of properties at risk of flooding; under the predicted scenarios:

- a 2°C increase will see the number of properties at significant chance of flooding rise from 860k to 1.2m by the 2080s
- a 4°C increase will see the number of properties at significant chance of flooding rise to 1.7m by the 2080s

Under a 4°C rise, there is a limit to the amount of flood risk that can be avoided through investment in flood defences, and there would also be irreversible damage done to the natural environment.

1.4 Addressing the problem

The issue and debate around the level government funding for flood defences is one that will always exist, and there is little that can be done to quell that. Instead, we will consider ways in which the actual modelling of flood inundation can be improved; even if real terms investment in flood defences does not change, being able to more accurately model flooding will mean an improvement in our ability to predict flood extents.

The standard approach to modelling water-body flow and flood inundation is through the shallow water equations, which model the *height* and *momentum* as conserved variables over time. However, if we want our flood model to be accurate, we need to ensure we also account for the various phenomena that influence or result in flooding. The primary drivers of flood inundation are *precipitation* (through either rain falling directly onto the water-body or runoff from the surrounding catchment) and *infiltration* (with water lost from the system when the soil is unsaturated or added to the system as recharge when the soil is saturated). There are a number of other water sources and sinks, some of which we have highlighted in Figure 1.4, that can also be considered.

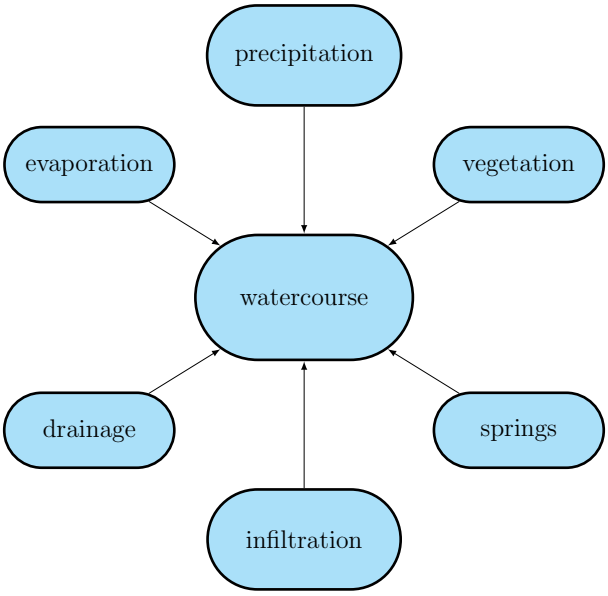

Figure 1.4: Our focus will be on the precipitation and infiltration processes, but there are a number of other sources and sinks that impact upon the hydrology of a watercourse.

It is not enough, however, to simply include these terms as either sources (when water is added) or sinks (when water is lost) in our shallow water system; we also need to ensure that their inclusion and the derivation of the extended flood model is consistent and mathematically rigorous. Since the shallow water equations are derived by applying a vertical averaging approach to the Navier-Stokes equations (under certain assumptions), it makes sense to use this as our starting point and include the precipitation and infiltration terms as boundary conditions in Navier-Stokes; this ensures we account for the effect the additional terms will have on the derivation.

As our desire is to apply the flood model we develop to real-world problems, we would like to go beyond modelling the flood inundation with just some assumed precipitation term. While we could model the phenomena using an ordinary deterministic equation, such an approach cannot accurately capture the random behaviour that the rainfall exhibits; therefore, if we want to ensure accuracy of our solutions, we will have to instead approach the problem from a stochastic viewpoint. There are a number of different methods that we can use to define the stochastic equation, and so we will have to consider and compare how well each approach reflects reality.

In addition to the stochastic behaviour, the precipitation rate at any given location is influenced by a number of meteorological phenomena that we would like to reflect, including the path and intensity of rain-bearing low pressure systems, variability in the jet stream, and the probability of particular weather patterns emerging. The impact of these effects will be available through observation data collected by weather stations or gauges, and so we will need to consider how we can include real-world data in our stochastic precipitation term; we may also need to consider what to do when such data is unavailable.

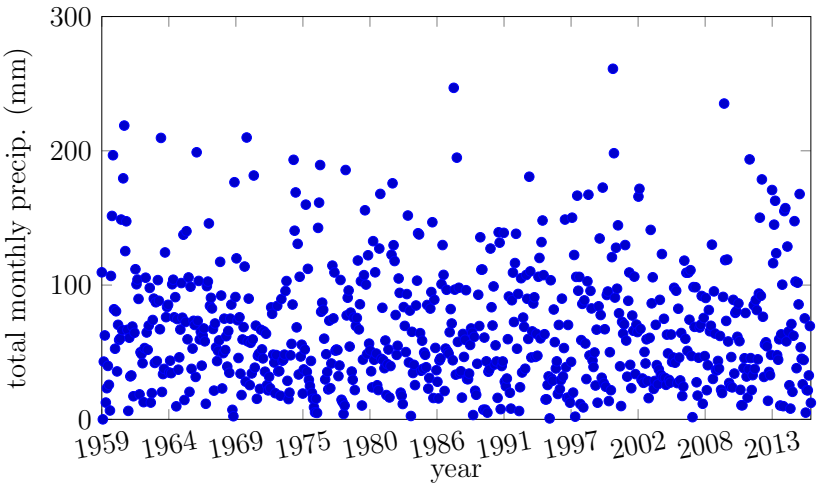

Figure 1.5: Total monthly precipitation for an example rain gauge.

The final consideration we will give is to how we simulate the flood modelling system that we have derived. Standard approaches of running multiple simulations and then combining the statistics of these outputs in some way will be possible but computationally (and thus monetarily) expensive; since our desire is to maximise the accuracy we can achieve for the same cost, techniques to speed up or improve the simulations will be required. We will have to take some care, however, to ensure that these techniques can be applied to our coupled system, in which the precipitation acts as a random forcing term on our shallow water model.

1.5 Summary

The motivation for this research can be summarised by the following question: *how can we better model flood inundation caused by precipitation?*

Our approach will be to model the problem using the shallow water equations with a stochastically perturbed source term designed to reflect precipitation statistics from observation data and knowledge of weather patterns. We will also consider techniques for speeding up numerical simulation of the model, to enable the maximum accuracy to be achieved for a given cost. This research can be applied to give a greater and more accurate understanding of the risk of flooding subject to knowledge of weather patterns and statistics.

Chapter 2

Literature review

The research, results, observations, and discussions that we will present below on flood modelling and stochastic precipitation do not exist in isolation and will build upon a breadth of existing literature and prior research. The topics that we will cover can be broadly divided into the following areas:

- shallow water equations
- numerical modelling of conservation laws
- kinetic scheme for the shallow water equations
- stochastic modelling of precipitation
- Monte Carlo methods

We will present here an overview of this existing literature and research, which we will make references to whilst developing our flood modelling and stochastic precipitation approach.

2.1 Shallow water equations

The shallow water equations are a system of hyperbolic conservation laws that model the flow of water in a river, ocean, or channel. The classical one-dimensional shallow water equations were developed by Adhémar Jean Claude Barré de Saint-Venant in the 19th Century as a reduction of the Navier-Stokes equations under certain assumptions on the horizontal and vertical scales [de Saint-Venant, 1871]. For the specific problem of modelling flood inundation caused by precipitation, the inclusion of such effects in the shallow water equations turns it from a conservation law into a balance. Existing approaches such as Sochala [2008] and Delestre et al. [2012] model this system as

$$\begin{aligned} \partial_t h + \partial_x q &= S \\ \partial_t q + \partial_x \left[\frac{q^2}{h} + \frac{\mathrm{g}\, h^2}{2} \right] &= -\,\mathrm{g}\, h \partial_x Z - k_0(q/h), \end{aligned} \tag{2.1.0.1}$$

where the unknowns $h(x,t)$ and $q(x,t) = hu$ model, respectively, the *height* and *momentum* of the water column at a space-time point (x,t), whilst $u(x,t)$ models

the water *velocity*. For the remaining terms, S is the source term defined as the net difference between water entering the flow (such as through rainfall) and water exiting the flow (such as through infiltration), g is the gravitational acceleration (considered a constant $\approx 9.81\text{m/s}^2$), $Z(x)$ the topography of the channel bed with slope $\partial_x Z(x)$, and $k_0(\cdot)$ an empirical fluid-wall friction. The first equation in (2.1.0.1) models the conservation of mass (in this case represented by the water height) whilst the second models the conservation of momentum. These equations can be extended to include additional terms representing the Coriolis force [Abarbanel et al., 2003] or viscosity ν [Ersoy, 2013].

This adaptation make sense from a physical perspective - the addition or loss of water from the flow will cause a corresponding change to the mass (*height*) of the water - but it does not entirely respect the derivation of the shallow water equations from Navier-Stokes. The research that we present below will look to solve this problem by going back to the original Navier-Stokes equations and adjusting the boundary conditions to account for the additional terms. In doing so, we will demonstrate how a new, extended shallow water model can be derived; this derivation from first principles has not, to our knowledge, been considered thus far in the literature.

The form we considered above presented the shallow water system in one spatial dimension, but these equations can also be considered in two-dimensions [Delis and Katsaounis, 2005, LeVeque et al., 2011, Delestre et al., 2014], extending the system above to include an additional equation for the conservation of momentum hv in the new spatial dimension y, as well as additional flux terms in the existing equations. For the application of two-dimensional pipe flow considered in Ersoy [2013], for example, the two-dimensional system can be modelled by the one-dimensional free surface model

$$\begin{aligned} \partial_t A + \partial_x Q &= 0 \\ \partial_t Q + \partial_x \left[\frac{Q^2}{A} + \mathrm{g}\, I_1(x, A) \cos\theta \right] &= -\,\mathrm{g}\, A \sin\theta + \mathrm{g}\, I_2(x, A) \cos\theta \end{aligned} \tag{2.1.0.2}$$

where A is the wet area, Q the discharge, I_1 the hydrostatic pressure, I_2 the pressure source term, and $\sin\theta$ the slope variation.

In the work we present below, we will consider the shallow water equations in one-dimension only; for the modelling applications we wish to consider (in which we assume there is no or negligible variation in the y spatial dimension) the one-dimensional system will be sufficient and indeed the reduction from two-dimensions will reduce the computational complexity required for our numerical modelling. These techniques and extensions, however, can be readily applied to the two-dimensional shallow water system by instead starting from the three-dimensional Navier-Stokes system for variables (h, hu, hv) or the three-dimensional Euler equations for the variables (A, Q); this derivation will be considered for future research.

2.2 Numerical modelling

In modelling mathematical systems, it is important that we have a numerical method which is stable and will give us a reasonably accurate solution. This is particularly

true in modelling conservation laws such as flood inundation: the outputs from such numerical simulations may be used as the basis for policy decisions or predictions on future events. Unlike other classes of equations, conservation laws have their own specific difficulties (such as the formation of shocks) that require careful attention when developing a numerical method. A number of approaches have therefore been derived that attempt to overcome these particular problems, including the introduction of numerical viscosity, shock tracking, and entropy conditions [LeVeque, 1992].

Perhaps the simplest approach to model shallow water is the finite difference method, whereby the solution at time-step $n+1$ is calculated as a combination of solutions at the current time n.

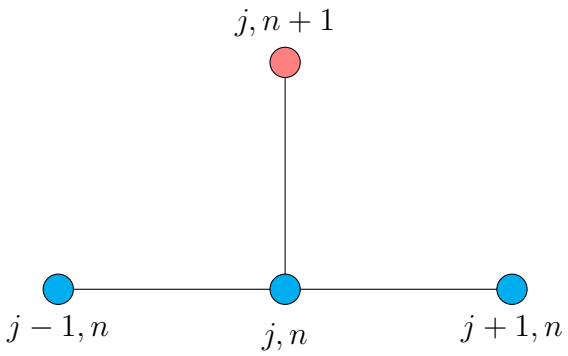

Figure 2.1: Stencil for an explicit finite difference method.

The finite difference method was applied to the problem of two-dimensional shallow water in de Almeida et al. [2012], giving the following explicit numerical scheme:

$$\begin{aligned} y_i^{n+1} &= y_i^n + \frac{\Delta t}{\Delta x}\left(q_{i-1/2}^{n+1} - q_{i+1/2}^{n+1}\right) \\ q_{i-1/2}^{n+1} &= \frac{q_{i-1/2}^n - \mathrm{g}\, h_f \frac{\Delta t}{\Delta x}\left(y_i^n - y_{i-1}^n\right)}{1 + \mathrm{g}\,\Delta t n^2 \left|q_{i-1/2}^n\right| / h_f^{7/3}} \end{aligned} \tag{2.2.0.1}$$

where $y = h + Z$. This scheme was intended to overcome certain problems that occur when modelling water flow on high-resolution topography and to address certain stability problems that can occur in low friction areas.

Another approach which is more accurate than the finite difference method but harder to implement computationally is the finite volume method [Kröner, 1997, LeVeque, 1992, 2002, Toro, 2009]. The finite volume method evaluates divergence terms in the differential equation as fluxes across boundaries between grid cells: as the flux into one cell will be equal to the flux leaving the adjacent cell, the method is conservative and so well suited to modelling conservation laws.

A finite volume scheme for the one-dimensional shallow water system (2.1.0.1) was presented in Delestre et al. [2008], given by

$$U_i^{n+1} = U_i^n - \frac{\Delta t}{\Delta x_i}\left(F_{i+1/2,L}^n - F_{i-1/2,R}^n - Fc_i^n\right) \tag{2.2.0.2}$$

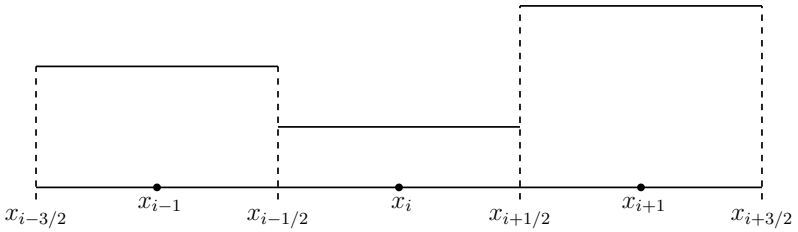

Figure 2.2: Finite volume mesh of the spatial domain with uniform cell size Δx.

where $F^n_{i+1/2,L}$ and $F^n_{i-1/2,R}$ are the left and right numerical fluxes, respectively, and Fc^n_i a cell-centred source term. This scheme was applied to a number of numerical tests and showed good consistency against both analytical and experimental data. For the two-dimensional shallow water, Singh et al. [2015] presented a method for simulating overland flows generated by rainfall from storm events, and which included infiltration simulated using the Green-Ampt equation. This method was applied to simulate historical storm events, and showed good capability in recreating the hydrological processes associated with rainfall-generated overland flows.

Due to its applicability to modelling conservation laws, we will use a finite volume scheme to model our extended shallow water system, similar to the model considered by Delestre et al. [2008]. However, since our shallow water system goes beyond the model considered therein, there will be added complications in ensuring the additional terms are appropriately included in the model; we will develop upon this approach, therefore, and calculate the numerical fluxes using a kinetic scheme, an overview of which is provided in §2.3.

2.3 Kinetic schemes

One of the challenges of modelling with finite volume methods is determining how to define the numerical fluxes between cells. A drawback of the approaches we presented in §2.2 which compute the flux between cells through approximate Riemann solvers (e.g. Roe, Godunov, HLL) is that they do not provide all the properties we would want our scheme to have. In modelling water and river flows, we would like our system to preserve equilibrium states, usually referred to as the *lake at rest*, which are given by

$$h + Z = \text{constant} \quad \text{and} \quad u = 0. \tag{2.3.0.1}$$

If we wish to maintain this property, we cannot rely on the usual finite difference or finite volume methods, and thus a new (so called well-balanced) approach is required. One such technique that has been developed uses ideas from kinetic theory, the basis of which comes from the description of a gas as a large number of particles (e.g. atoms or molecules) that are in constant rapid (and random) motion as a result of collisions between the particles that make up the gas.

This idea was originally developed by Daniel Bernoulli in the 18th Century [Bernoulli, 1738], though it wasn't until the start of the 20th Century (before which atoms were still considered theoretical) when work by Einstein and Smoluchowski solidified the idea [Einstein, 1905, von Smoluchowski, 1906]. Within the kinetic framework,

certain macroscopic properties (such as pressure or temperature) are explained or defined by considering the molecular composition and motion of the substance; temperature, for example, is defined as proportional to the average kinetic energy of the atoms that make up the substance.

Though the kinetic framework outlined above is concerned with describing gas particle motion, we will make use below of the ideas developed therein for our problem (that is, the motion of water in a channel). Such an approach for the shallow water equations can be found by going back to the first proof of the existence of weak solutions after shocks for hyperbolic systems, which was achieved by a kinetic interpretation of the system, as detailed in Audusse et al. [2000] and Perthame and Simeoni [2001], and further developed by Bourdarias et al. [2014] and Ersoy [2015]. Properties of the kinetic scheme for the shallow water equations (though without rainfall and precipitation terms) are presented in Xu [2002].

The method we use for the derivation of our kinetic scheme will follow much the same approach, though with the added complication of accounting for the additional terms. We will show in our approach that the derivation of the kinetic scheme for the shallow water equations can be extended to include the additional source terms S and Su in the mass and momentum equations, respectively, and that the additional friction terms can be appropriately packed with the existing friction and topography terms as already considered in the literature.

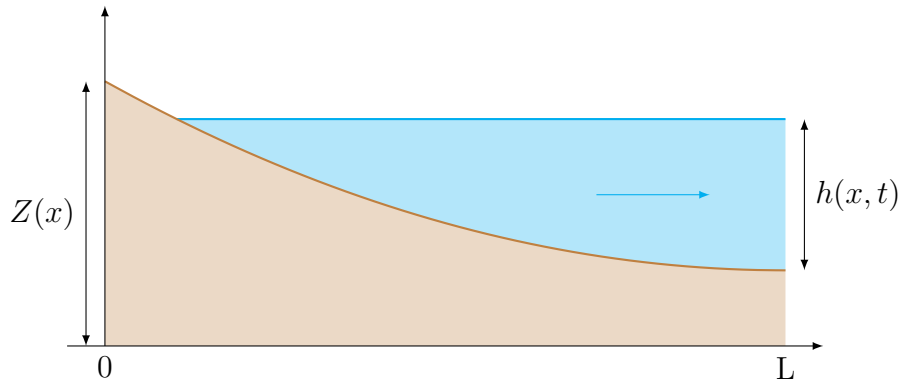

Figure 2.3: Kinetic solvers are well suited to dealing with cases when the water height $h(x,t) = 0$, such as water flowing away from a beach front.

One of the direct benefits of using such a approach for the shallow water system is the ability of the kinetic solver to deal with dry soil cases (that is, when $h = 0$) [Audusse et al., 2000], which will be of importance in ensuring our model continues to function if infiltration causes the water level to fall close to zero, or if we consider cases such as water flowing away from a beach front as depicted in Figure 2.3.

2.4 Stochastic modelling of precipitation

In modelling physical systems mathematically, the most general approach is to model the system as the time derivative of a variable $X(t)$ which is equal to some given

function $a(X,t)$:

$$\frac{dX}{dt} = a(X,t), \qquad X(t_0) = X_0. \tag{2.4.0.1}$$

The problem with this formulation is that, for certain systems, the physical reality exhibits random behaviour or interactions that are too complex to be represented by a single deterministic function a; this discovery was made concurrently by Einstein [1905] and von Smoluchowski [1906], developing previous work by Robert Brown.

If we want our representation to be accurate, we need some way to model this. The solution comes through stochastic differential equations, whereby the right-hand side of our ordinary differential equation (the *drift* term a) is perturbed by a random forcing (or *diffusion*) term:

$$\begin{cases} dX(t) = a(X(t),t)dt + b(X(t),t)dW_t \\ X(t_0) = X_0, \end{cases} \tag{2.4.0.2}$$

where $b(X(t),t)$ is the intensity and $W(t)$ a Wiener process. In integral form this equation becomes

$$X(t,\omega) = X(t_0,\omega) + \int_{t_0}^{t} a\left(X(s,\omega),s\right) ds + \int_{t_0}^{t} b\left(X(s,\omega),s\right), dW_s(\omega) \tag{2.4.0.3}$$

for a given sample path ω. The problem, however, is that the second integral does not exist as an ordinary integral, and thus we require a new stochastic calculus to make sense of the integral; the two most common approaches are Itô calculus and Stratonovich calculus, though it is possible to convert from one approach to the other [Brzezniak and Zastawniak, 1999, Øksendal, 2003, Klebaner, 2012].

For certain choices of $a(X,t)$ and $b(X,t)$ it is possible to solve the stochastic differential equation explicitly, but in general this is not possible. The most basic approach to solving the equation numerically is the *Euler-Maruyama* method [Kloeden and Platen, 1999]: we partition our time domain $[t_0,T]$ into a sequence of discretisation points

$$t_0 = \tau_0 < \tau_1 < \cdots < \tau_N = T \tag{2.4.0.4}$$

given by

$$\tau_n = \tau_{n-1} + \Delta\tau_n \quad \text{for } n = 1,\ldots,N \tag{2.4.0.5}$$

and approximate the stochastic process $X(\tau_n)$ by Y_n and the integrals as

$$\begin{aligned} \int_{\tau_n}^{\tau_{n+1}} a(X(t),t)dt &\approx a(Y_n,\tau_n)\left(\tau_{n+1}-\tau_n\right) = a(Y_n,\tau_n)\Delta\tau_{n+1} \\ \int_{\tau_n}^{\tau_{n+1}} b(X(t),t)dW_t &\approx b(Y_n,\tau_n)(W_{\tau_{n+1}} - W_{\tau_n}), \end{aligned} \tag{2.4.0.6}$$

giving us the Euler-Maruyama approximation

$$\begin{cases} Y_{n+1} = Y_n + a(Y_n,\tau_n)\Delta\tau_{n+1} + b(Y_n,\tau_n)(W_{\tau_{n+1}} - W_{\tau_n}) \\ Y_0 = X_0. \end{cases} \tag{2.4.0.7}$$

Higher-order methods such as the *Milstein* method or *Runge-Kutta* method for stochastic differential equations can also be used.

In modelling stochastic precipitation, a useful technique for creating such data are weather generators, which model the precipitation using a cluster of stochastic processes. A review of the underlying background and research into weather generators was provided in Onof et al. [2000], focusing on the two main cluster models, the Bartlett-Lewis and Neyman-Scott models, and recent developments in the field. Of particular interest for our research and its applicability in modelling rainfall in a variety of locations is the regionalisation of the parameters that drive the weather generator models. Such a regionalisation was considered in Cowpertwait et al. [2013], in which a superposition of two Neyman-Scott models fitting to daily temperature data was used to model spatiotemporal rainfall in the Basque Country, Spain, while Srikanthan and McMahon [2001] demonstrated how transition probability matrices could be used for the parameters to account for whether the rainfall was occurring in a wet or a dry period.

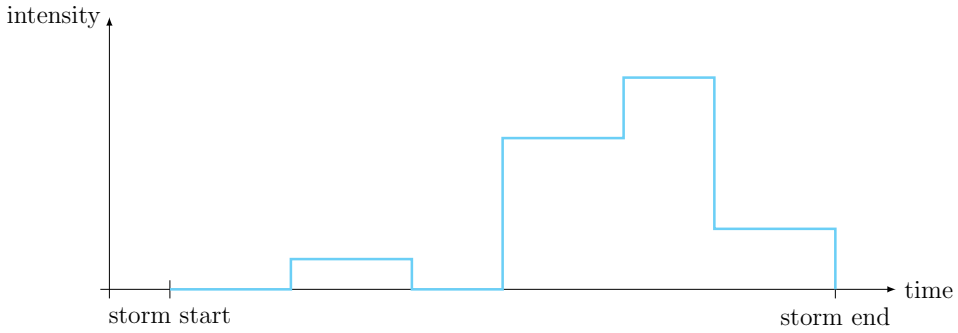

Figure 2.4: Aggregated rain function for an example storm at a given location.

Our aim in this thesis will be to combine these two approaches together: we will use a weather generator to determine the location and timing of the precipitation, thereby capturing the physical occurrence and patterning of rainfall more accurately, and then model the intensity using a stochastic equation with a drift term derived from observation data and a diffusion term with appropriate noise process.

2.5 Monte Carlo methods

As we are looking to model the precipitation as a stochastic process, each simulation we run of the system will generate a different sample path ω and thus lead to a different end solution. Though the solution from a single simulation may tell us something, it cannot tell us what the entire distribution of solutions may look like. The obvious solution is to run multiple simulations, generating a distribution of possible solutions, and then calculate statistical values from this.

The most common method to generating such a distribution of solutions is the Monte Carlo methods, a class of algorithms used extensively in numerical simulations when one wishes to repeatedly sample from a given distribution. As we sample from the distribution more and more, the statistics for these samples will tend to the statistics of the true solution. An early variant of the Monte Carlo method was Buffon's needle experiment, a method proposed by Georges-Louis Leclerc, Comte de Buffon, which can be used to estimate the value of π, while what we would view as the modern

Monte Carlo method was first introduced and used by researchers at *Los Alamos National Laboratory* in the 1940s [Liu, 2004].

Though the Monte Carlo methods are very simple to run and implement, a major drawback of the methods is that they are very computationally expensive. If we wish to achieve $\mathrm{O}(\varepsilon)$ accuracy for our solution, we require the number of samples of the discretisation $N = \mathrm{O}(\varepsilon^{-2})$ and the time step $\Delta t = \mathrm{O}(\varepsilon)$; thus the computational cost can be calculated as

$$\text{cost} = \frac{MT}{\Delta t} = \frac{\mathrm{O}(\varepsilon^{-2})}{\mathrm{O}(\varepsilon)} = \mathrm{O}\left(\varepsilon^{-3}\right). \tag{2.5.0.1}$$

This means that if we want to achieve a 10x increase in accuracy, the computational cost will increase by 1000. This increase in computational complexity will become highly restrictive if we desire a high level of accuracy, and thus it is desirable to consider how this can be improved upon.

Several methods have been proposed as an improvement on the standard approach. Quasi Monte Carlo [Niederreiter, 1992] attempts to address the problem of a high computational cost by changing the manner in which the random numbers are generated, ensuring a more equal distribution of points over the domain. The benefit of Quasi Monte Carlo over the standard method is that the rate of convergence is increased to $\mathrm{O}(N^{-1})$ from $\mathrm{O}(N^{-0.5})$ and hence we have a lower computational cost. Quasi Monte Carlo has been applied to a number of problems, including finance [Giles et al., 2008] and elliptic PDEs [Graham et al., 2011, 2013].

Another approach which attempts to address the problem of high computational cost is Multilevel Monte Carlo, which was introduced in Giles [2006], building on a similar two-level approach that had previously been considered by Kebaier [2005]. Unlike Quasi Monte Carlo, which adjusts the random inputs for the simulations in a particular way, Multilevel Monte Carlo exploits our ability to run simulations at different grid levels. On the coarser grids, simulations are run a large number of times while on the finer grids only a small number of simulations are run. The resulting combined estimator then has a lower computational cost for the standard Monte Carlo method.

Research into Multilevel Monte Carlo and its application to particular problems is wide-ranging; an extensive list of researchers, project groups, and papers can be found at [MLMC research]. For the specific application of modelling shallow water flows with random source terms, a multilevel approach was considered in Mishra et al. [2012] for a two-dimensional shallow water system to improve upon the convergence rate of the standard Monte Carlo method. In this case, the randomness was assumed to be due to possible measurement errors in the initial data and bottom topography.

For our approach, however, the stochasticity in our shallow water equations will come from the rainfall, and our aim is to use the Multilevel Monte Carlo method to model the extended shallow water system coupled with a stochastic precipitation term; to our knowledge, this is the first such application of MLMC to stochastic precipitation thus far.

Chapter 3

A rigorous extension of the shallow water equations

In quantifying the dynamics of a watercourse, the most important component of the hydrologic recharge and loss is the precipitation and infiltration process, respectively. Modelling these processes and predicting the motion of water is a difficult task to which substantial effort has been devoted [Grace and Eagleson, 1966, Woolhiser and Liggett, 1967, Zhang and Cundy, 1989, Esteves et al., 2000, Weill et al., 2009, Rousseau et al., 2012].

Our goal is to derive a model akin to (2.1.0.1) via vertical averaging under the shallow water assumption, starting from the Navier–Stokes equations with a permeable Navier boundary condition to account for the infiltration and a kinematic boundary condition to consider the precipitation. The obtained averaged model extends this system in a unique manner through an additional momentum source term of the form

$$Su - (k_R - k_I)\, u, \quad \text{with } S = R - I, \tag{3.0.0.1}$$

where $R \geq 0$ denotes the recharge rate on the free surface (accounting for both rain and runoff effects) and I denotes the infiltration rate from the water to the ground (when $I > 0$) or the ground to the water (when $I < 0$). The terms k_R and k_I, which will be discussed in detail in §3.1, model the friction caused by the addition of water (at zero velocity), which attaches to and is advected by the flow. We will see below that these friction terms are necessary to avoid paradoxical outcomes such as perpetual motion.

In this chapter we provide an overview of the construction of the extended shallow water system for overland flows, extending the standard shallow water system to account for the addition of water through rainfall and runoff processes. In §3.1, we present the geometric setup of the system and the adjusted boundary conditions from the typical Navier–Stokes equations, before introducing the first order approximation which leads to the extended shallow water system in §3.2. Finally, we discuss several theoretical results and corollaries that can be derived for the system in §3.3.

3.1 Geometric setup and boundary conditions

We consider an incompressible fluid moving in the space-time box

$$\left\{ \begin{array}{c} [0,L]\times[0,T]\times\mathbb{R} \text{ with typical point } (x,t,z) \\ \text{where } L>0 \text{ is the } \textit{horizontal length} \text{ of the domain} \end{array} \right\}. \tag{3.1.0.1}$$

The *absolute height* of the surface of the water course and the *topography* of the river-bed are modelled, respectively, by functions

$$H : [0,L]\times[0,T]\to\mathbb{R}, \qquad Z : [0,L]\to\mathbb{R} \tag{3.1.0.2}$$

whose values measure the *water height* with respect to a *reference horizontal height 0*. We define the *local height* of the water by

$$h(x,t) := H(x,t) - Z(x). \tag{3.1.0.3}$$

The *wet region* is defined as the area in which the fluid resides at each time $t\in[0,T]$

$$\Omega(t) := \{(x,z)\in\mathbb{R}^2 : x\in(0,L), Z(x)<z<H(x,t)\} \tag{3.1.0.4}$$

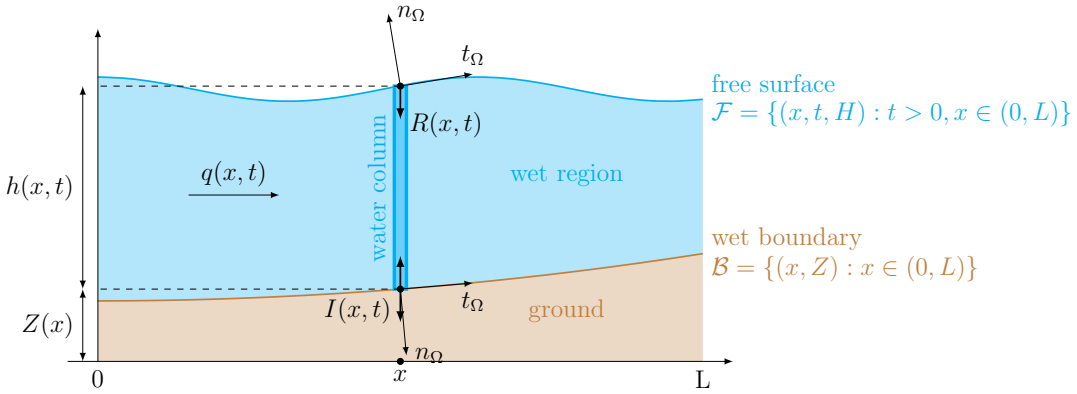

Figure 3.1: Diagram of a river and river bed depicting the variables of interest

As we can see in Figure 3.1, the wet region has two boundaries; the first is the wet boundary between the wet region and the ground, denoted by

$$\mathcal{B} = \{(x,Z) : x\in(0,L)\}, \tag{3.1.0.5}$$

and the second is the free surface between the wet region and the surrounding air, denoted by

$$\mathcal{F} = \{(x,t,H) : t>0, x\in(0,L)\}. \tag{3.1.0.6}$$

We assume that the viscous flow $\boldsymbol{u}$ satisfies, on the space-time domain Ω, the two-dimensional incompressible Navier Stokes equation

$$\begin{aligned} \operatorname{div}[\rho_0\boldsymbol{u}^\intercal] &= 0, \\ \partial_t[\rho_0\boldsymbol{u}] + \operatorname{div}[\rho_0\boldsymbol{u}\otimes\boldsymbol{u}] - \operatorname{div}\boldsymbol{\sigma}[\boldsymbol{u}] - \rho_0\boldsymbol{F} &= 0, \end{aligned} \tag{3.1.0.7}$$

where $\boldsymbol{u} = (u, v)$ is the velocity field, ρ_0 is the density of the fluid (taken to be constant), $\boldsymbol{F} = (0, -\mathrm{g})$ is the external force of gravity with constant g, and $\boldsymbol{\sigma}[\boldsymbol{u}]$ is the total stress tensor whose matrix is given by

$$\boldsymbol{\sigma}[\boldsymbol{u}] := \begin{bmatrix} -p + 2\mu\partial_x u & \mu\left(\partial_z u + \partial_x v\right) \\ \mu\left(\partial_z u + \partial_x v\right) & -p + 2\mu\partial_z v \end{bmatrix} \tag{3.1.0.8}$$

where p is the pressure and $\mu > 0$ the dynamic viscosity. The tensor product of two vectors $\boldsymbol{a} \otimes \boldsymbol{b}$ is defined as $\boldsymbol{a}\boldsymbol{b}^\intercal$ (all vectors are displayed as columns) and the div of a covector/tensor is taken as the row-wise divergence of the associated matrix.

To work with the wet region, we introduce its *indicator function*

$$\Phi(x, t, z) := \mathbb{I}_{\Omega(t)}(x, z) = \mathbb{I}[Z(x) \leq z \leq H(x, t)] \text{ for all } x, t, z \in \mathbb{R}. \tag{3.1.0.9}$$

The function Φ is advected by the flow so its material derivative, with respect to the flow $\boldsymbol{u}$, must therefore be zero. Moreover, thanks to the incompressibility condition, Φ satisfies the following *indicator transport equation*

$$\partial_t \Phi + \partial_x[\Phi u] + \partial_z[\Phi v] = 0 \text{ on } \Omega. \tag{3.1.0.10}$$

3.1.1 The wet boundary

On the wet boundary the topography is assumed to be rough and hence produces friction. We take this into account by considering the following *Navier boundary condition*:

$$\left(\boldsymbol{\sigma}[\boldsymbol{u}]\, n_\Omega\right) \cdot t_\Omega = -\rho_0 \left(k(\boldsymbol{u}) - k_I\right) \boldsymbol{u} \cdot t_\Omega \qquad \text{on } \mathcal{B}, \tag{3.1.1.1}$$

where t_Ω and n_Ω are, respectively, the unit tangential and normal vectors to the wet boundary. We will leave defining k_I for the moment and note that the scalar function $k(\boldsymbol{u})$ models a general friction law on the channel bed:

$$k(\boldsymbol{\xi}) := \left(C_{\mathrm{lam}} + C_{\mathrm{tur}}|\xi|\right) \quad \forall \xi \in \mathbb{R}^2, \tag{3.1.1.2}$$

with friction coefficients C_{lam} and C_{tur} (which by definition are always non-negative) corresponding, respectively, to the laminar and turbulent friction factors.

The ground may also, due to porosity, absorb water (by infiltration) or inject water (through recharge) from and into the bulk. This mechanism is modelled with the following *permeable boundary condition*:

$$\boldsymbol{u} \cdot n_\Omega = I(x, t, h(x, t)) \qquad \text{on } \mathcal{B}, \tag{3.1.1.3}$$

where the infiltration function I models the amount of water that leaves ($I > 0$) or enters ($I < 0$) the flow per elementary boundary element. The friction effect of the water recharging through the ground on the flow itself is modelled by

$$k_I = \alpha \, \min(0, I) \tag{3.1.1.4}$$

with α representing the magnitude of the friction effect. We note that the recharge-induced friction only occurs when water is entering the flow (i.e. $I < 0$), and is zero otherwise. We define Ω's tangential and outward unit normal vectors on $\mathcal{B}$ by

$$t_\Omega(x, Z(x)) = \frac{1}{\sqrt{1 + |\partial_x Z(x)|^2}} \begin{bmatrix} -1 \\ -\partial_x Z(x) \end{bmatrix} \tag{3.1.1.5}$$

and

$$n_\Omega(x, Z(x)) = \frac{1}{\sqrt{1+|\partial_x Z(x)|^2}} \begin{bmatrix} \partial_x Z(x) \\ -1 \end{bmatrix} \tag{3.1.1.6}$$

respectively, following the convention that the outward normal is the tangential vector rotated by $\pi/2$ counterclockwise. We can use these definitions to simplify equations (3.1.1.1) and (3.1.1.3); considering first the left-hand side of (3.1.1.1), we have:

$$\begin{aligned} \sigma[\boldsymbol{u}]\, n_\Omega &= \frac{1}{\sqrt{1+|\partial_x Z|^2}} \begin{bmatrix} (-p + 2\mu\partial_x u)\,\partial_x Z - \mu\,(\partial_z u + \partial_x v) \\ \mu\,(\partial_z u + \partial_x v)\,\partial_x Z + p - 2\mu\partial_z v \end{bmatrix} \\ (\sigma[\boldsymbol{u}]\, n_\Omega)\cdot t_\Omega &= \frac{\mu\,(\partial_z u + \partial_x v)\left(1-|\partial_x Z|^2\right) + 2\mu\,(\partial_z v - \partial_x u)\,\partial_x Z}{1+|\partial_x Z|^2}. \end{aligned} \tag{3.1.1.7}$$

On the right hand side we have

$$\begin{aligned} \rho_0\,(k(\boldsymbol{u}) - k_I)\,\boldsymbol{u} &= \rho_0\,(k(u,v) - k_I) \begin{bmatrix} u \\ v \end{bmatrix} \\ -\rho_0\,(k(\boldsymbol{u}) - k_I)\,\boldsymbol{u}\cdot t_\Omega &= \frac{\rho_0\,(k(u,v) - k_I)\,(u + v\partial_x Z)}{(1+|\partial_x Z|^2)^{1/2}}. \end{aligned} \tag{3.1.1.8}$$

Bringing these two equations together, (3.1.1.1) simplifies to

$$\begin{aligned} &\frac{\mu\,(\partial_x v + \partial_z u)\left(1-|\partial_x Z|^2\right) + 2\mu\,(\partial_z v - \partial_x u)\,\partial_x Z}{\left(1+|\partial_x Z|^2\right)^{1/2}} \\ &\qquad = \rho_0\,(k(u,v) - k_I)\,(u + v\partial_x Z)\,. \end{aligned} \tag{3.1.1.9}$$

Similarly, (3.1.1.3) can be rewritten as

$$\boldsymbol{u}\cdot n_\Omega = \begin{bmatrix} u \\ v \end{bmatrix} \cdot \frac{1}{\sqrt{1+|\partial_x Z|^2}} \begin{bmatrix} \partial_x Z \\ -1 \end{bmatrix} = \frac{u\partial_x Z - v}{\sqrt{1+|\partial_x Z|^2}} = I. \tag{3.1.1.10}$$

Simplifying and moving all terms to one-side, (3.1.1.10) becomes

$$v - u\partial_x Z(x) + I\sqrt{1+|\partial_x Z|^2} = 0. \tag{3.1.1.11}$$

3.1.2 The free surface

On the free surface we neglect all other meteorological phenomena (such as evaporation) and consider only the addition of water in the form of direct rainfall and runoff. Assuming a kinematic boundary condition, we set

$$\boldsymbol{u}\cdot n_\Omega = \frac{\partial_t H - R}{\sqrt{1+|\partial_x H|^2}} \text{ on } \mathcal{F} := \{(x,t,H(x,t)) : 0 < x < L \text{ and } t > 0\} \tag{3.1.2.1}$$

where $R(x,t)$ is the recharge rate due to rainfall. The unit tangential and normal vectors t_Ω and n_Ω to the free surface can be explicitly computed in terms of H as

$$t_\Omega(x,H(x,t)) = \frac{1}{\sqrt{1+|\partial_x H(x,t)|^2}}\begin{bmatrix}1\\ \partial_x H(x,t)\end{bmatrix} \tag{3.1.2.2}$$

and

$$n_\Omega(x,H(x,t)) = \frac{1}{\sqrt{1+|\partial_x H(x,t)|^2}}\begin{bmatrix}-\partial_x H(x,t)\\ 1\end{bmatrix} \tag{3.1.2.3}$$

which leads to the following explicit form of (3.1.2.1):

$$\partial_t H + u\partial_x H - v = R \text{ on } \mathcal{F}. \tag{3.1.2.4}$$

We also assume a stress condition on the free surface, given by

$$(\boldsymbol{\sigma}[\boldsymbol{u}]\, n_\Omega)\cdot t_\Omega = -\rho_0 k_R \boldsymbol{u}\cdot t_\Omega, \tag{3.1.2.5}$$

where $k_R = \alpha R$ models the friction effect of the rain droplets on the free surface, with α again representing the magnitude of this effect. Using the tangential and normal vectors (3.1.2.2) and (3.1.2.3), respectively, this condition simplifies as follows:

$$\begin{aligned}\sigma[\boldsymbol{u}]\, n_\Omega &= \frac{1}{\sqrt{1+|\partial_x H|^2}}\begin{bmatrix}(p-2\mu\partial_x u)\,\partial_x H + \mu\,(\partial_z u+\partial_x v)\\ -\mu\,(\partial_z u+\partial_x v)\,\partial_x H - p + 2\mu\partial_z v\end{bmatrix}\\ (\sigma[\boldsymbol{u}]\, n_\Omega)\cdot t_\Omega &= \frac{\mu\,(\partial_z u+\partial_x v)\left(1-|\partial_x H|^2\right) + 2\mu\,(\partial_z v-\partial_x u)\,\partial_x H}{1+|\partial_x H|^2}\end{aligned} \tag{3.1.2.6}$$

and

$$-\rho_0 k_R \boldsymbol{u}\cdot t_\Omega = -\frac{\rho_0 k_R\,(u+v\partial_x H)}{(1+|\partial_x H|^2)^{1/2}}. \tag{3.1.2.7}$$

Bringing these two equations together, (3.1.2.5) simplifies to

$$\frac{\mu\,(\partial_x v+\partial_z u)\left(1-|\partial_x H|^2\right) + 2\mu\,(\partial_z v-\partial_x u)\,\partial_x H}{\left(1+|\partial_x H|^2\right)^{1/2}} = -\rho_0 k_R\,(u+v\partial_x H)\,. \tag{3.1.2.8}$$

3.2 Shallow water system with precipitation

We now proceed to write the Navier–Stokes equations with adapted boundary conditions in non-dimensional form. Under an assumption on the shallowness of the ratio of the water height to the horizontal domain (represented by small parameter ε), we formally make an asymptotic expansion of the Navier–Stokes system to the hydrostatic approximation at first order. Finally, we derive the shallow water system through an integration on the water height.

This approach follows one established by Gerbeau and Perthame [2001] and also found in Ersoy [2015]; the difference in our application, however, is that we will be using as our starting point a two-dimensional rather than three-dimensional system, and we will also have to take extra care in how we non-dimensionalise our additional precipitation, infiltration, and friction terms.

3.2.1 Non-dimensionalisation approach and assumptions

To derive the shallow water model, we make the following assumptions:

- the water height is small with respect to the horizontal length of the domain
- vertical variations in velocity are small compared to the horizontal variations

This is achieved by postulating a *small parameter* ratio

$$\varepsilon := \frac{D}{L} = \frac{V}{U} \ll 1 \tag{3.2.1.1}$$

where D, L, V, and U are the scales of water height, domain length, vertical fluid velocity, and horizontal fluid velocity, respectively. As a consequence, the time scale T is such that

$$T = \frac{L}{U} = \frac{D}{V}. \tag{3.2.1.2}$$

We also choose the pressure scale to be

$$P := \rho_0 U^2. \tag{3.2.1.3}$$

The rationale for this choice is that we are focusing on the effect of the horizontal forces as mass per horizontal acceleration, which has a force scale of

$$F := (DL^{2-1}\rho_0)(UT^{-1}), \tag{3.2.1.4}$$

and these forces are applied to vertical boundary scale to give the pressure scale

$$F\big(DL^{2-2}\big)^{-1} = DL\rho_0 UT^{-1}D^{-1} = \rho_0 ULT^{-1} = \rho_0 U^2. \tag{3.2.1.5}$$

It is convenient to define the domain length, L, and horizontal velocity, U, (and by definition T) as finite constants with respect to $\varepsilon \to 0$, while the water height and vertical velocity are defined as $D = \varepsilon L$ and $V = \varepsilon U$, respectively. This allows us to introduce the dimensionless quantities of time $\tilde{t}$, space $(\tilde{x}, \tilde{z})$, pressure $\tilde{p}$, and velocity field $(\tilde{u}, \tilde{v})$ via the following scaling relations:

$$\left\{ \begin{array}{ll} \tilde{t} := \dfrac{t}{T}, & \tilde{p}(\tilde{x},\tilde{t},\tilde{z}) := \dfrac{p(x,t,z)}{P}, \\ \tilde{x} := \dfrac{x}{L}, & \tilde{u}(\tilde{x},\tilde{t},\tilde{z}) := \dfrac{u(x,t,z)}{U}, \\ \tilde{z} := \dfrac{z}{D} = \dfrac{z}{\varepsilon L}, & \tilde{v}(\tilde{x},\tilde{t},\tilde{z}) := \dfrac{v(x,t,z)}{V} = \dfrac{v(x,t,z)}{\varepsilon U} \end{array} \right\}. \tag{3.2.1.6}$$

We also rescale the laminar and turbulent friction factors as, respectively,

$$C_{\text{lam},0} := \frac{C_{\text{lam}}}{V} = \frac{C_{\text{lam}}}{\varepsilon U} \quad \text{and} \quad C_{\text{tur},0} := \frac{C_{\text{tur}}}{\varepsilon}, \tag{3.2.1.7}$$

and the infiltration and rainfall rates as, respectively,

$$\tilde{I}(\tilde{x},\tilde{t}) := \frac{I(x,t)}{V} \quad \text{and} \quad \tilde{R}(\tilde{x},\tilde{t}) := \frac{R(x,t)}{V}. \tag{3.2.1.8}$$

Note that in the assumed asymptotic setting, $C_{\text{lam},0}$ and $C_{\text{tur},0}$ are constants with respect to ε, thus implying that C_{lam} and C_{tur} vanish linearly with $\varepsilon \to 0$. Finally, we define the following non-dimensional numbers:

$$\begin{aligned} &\text{Froude's number,} && \text{Fro} := U/\sqrt{\mathrm{g}\, D}, \\ &\text{Reynolds's number with respect to } \mu, && \text{Rey} := \rho_0 U L/\mu. \end{aligned} \tag{3.2.1.9}$$

and consider the following asymptotic setting

$$\text{Rey}^{-1} = \varepsilon \mu_0, \tag{3.2.1.10}$$

where μ_0 is the *viscosity*.

3.2.2 Dimensionless Navier-Stokes equations

We now proceed to apply these dimensionless variables to the Navier–Stokes equations (3.1.0.7) and (3.1.0.8).

Equation 1

For the first equation we have:

$$0 = \operatorname{div}[\rho_0 \boldsymbol{u}] = \rho_0 \cdot \operatorname{div}[\boldsymbol{u}] = \rho_0 \left(\frac{\partial u}{\partial x} + \frac{\partial v}{\partial z} \right) = \rho_0 \left(\frac{U}{L} \frac{\partial \tilde{u}}{\partial \tilde{x}} + \frac{\varepsilon U}{\varepsilon L} \frac{\partial \tilde{v}}{\partial \tilde{z}} \right) \tag{3.2.2.1}$$

$$\rho_0 \frac{U}{L} \left(\frac{\partial \tilde{u}}{\partial \tilde{x}} + \frac{\partial \tilde{v}}{\partial \tilde{z}} \right) = 0 \to \left(\frac{\partial \tilde{u}}{\partial \tilde{x}} + \frac{\partial \tilde{v}}{\partial \tilde{z}} \right) = \operatorname{div}[\tilde{\boldsymbol{u}}] = 0. \tag{3.2.2.2}$$

Equation 2

For the second equation we have:

$$\begin{aligned} &\frac{\partial (\rho_0 u)}{\partial t} + \frac{\partial (\rho_0 u^2)}{\partial x} + \frac{\partial (\rho_0 uv)}{\partial z} \\ &\qquad - \left(-\frac{\partial p}{\partial x} + 2\mu \frac{\partial}{\partial x} \left[\frac{\partial u}{\partial x} \right] + \mu \frac{\partial}{\partial z} \left[\frac{\partial u}{\partial z} + \frac{\partial v}{\partial x} \right] \right) = 0. \end{aligned} \tag{3.2.2.3}$$

This becomes:

$$\begin{aligned} &\frac{\rho_0 U}{T} \frac{\partial \tilde{u}}{\partial \tilde{t}} + \frac{\rho_0 U^2}{L} \frac{\partial (\tilde{u}^2)}{\partial \tilde{x}} + \frac{\rho_0 \varepsilon U^2}{\varepsilon L} \frac{\partial (\tilde{u}\tilde{v})}{\partial \tilde{z}} + \frac{\rho_0 U^2}{L} \frac{\partial \tilde{p}}{\partial \tilde{x}} \\ &\qquad = \frac{2\mu U}{L^2} \frac{\partial}{\partial \tilde{x}} \left[\frac{\partial \tilde{u}}{\partial \tilde{x}} \right] + \frac{\mu U}{\varepsilon L^2} \frac{\partial}{\partial \tilde{z}} \left[\frac{1}{\varepsilon} \frac{\partial \tilde{u}}{\partial \tilde{z}} + \varepsilon \frac{\partial \tilde{v}}{\partial \tilde{x}} \right]. \end{aligned} \tag{3.2.2.4}$$

Recalling that $T = {}^{L}/_{U}$, $\mathrm{Rey} = {}^{\rho_0 U L}/_{\mu}$, and $\mathrm{Rey}^{-1} = \varepsilon\mu_0$, we multiply each term by ${}^{L}/_{\rho_0 U^2}$, giving us

$$\begin{aligned}\frac{\partial\tilde{u}}{\partial\tilde{t}} + \frac{\partial\left(\tilde{u}^2\right)}{\partial\tilde{x}} + \frac{\partial\left(\tilde{u}\tilde{v}\right)}{\partial\tilde{z}} + \frac{\partial\tilde{p}}{\partial\tilde{x}} \\ &= \frac{2\mu}{\rho_0 U L}\frac{\partial}{\partial\tilde{x}}\left[\frac{\partial\tilde{u}}{\partial\tilde{x}}\right] + \frac{\mu}{\rho_0 U L}\frac{\partial}{\partial\tilde{z}}\left[\frac{1}{\varepsilon^2}\frac{\partial\tilde{u}}{\partial\tilde{z}} + \frac{\partial\tilde{v}}{\partial\tilde{x}}\right] \\ &= \frac{2}{\mathrm{Rey}}\frac{\partial}{\partial\tilde{x}}\left[\frac{\partial\tilde{u}}{\partial\tilde{x}}\right] + \frac{1}{\mathrm{Rey}}\frac{\partial}{\partial\tilde{z}}\left[\frac{1}{\varepsilon^2}\frac{\partial\tilde{u}}{\partial\tilde{z}} + \frac{\partial\tilde{v}}{\partial\tilde{x}}\right] \\ &= \frac{\partial}{\partial\tilde{z}}\left[\frac{\mu_0}{\varepsilon}\frac{\partial\tilde{u}}{\partial\tilde{z}}\right] + \varepsilon\mu_0\left(\frac{\partial}{\partial\tilde{x}}\left[2\frac{\partial\tilde{u}}{\partial\tilde{x}}\right] + \frac{\partial}{\partial\tilde{z}}\left[\frac{\partial\tilde{v}}{\partial\tilde{x}}\right]\right).\end{aligned} \tag{3.2.2.5}$$

Equation 3

For the third equation we have:

$$\begin{aligned}\frac{\partial\left(\rho_0 v\right)}{\partial t} + \frac{\partial\left(\rho_0 uv\right)}{\partial x} + \frac{\partial\left(\rho_0 v^2\right)}{\partial z} \\ - \left(\mu\frac{\partial}{\partial x}\left[\frac{\partial u}{\partial z} + \frac{\partial v}{\partial x}\right] - \frac{\partial p}{\partial z} + 2\mu\frac{\partial}{\partial z}\left[\frac{\partial v}{\partial z}\right]\right) = -\rho_0\,\mathrm{g}\,.\end{aligned} \tag{3.2.2.6}$$

This becomes

$$\begin{aligned}\frac{\rho_0\varepsilon U}{T}\frac{\partial\tilde{v}}{\partial\tilde{t}} + \frac{\rho_0\varepsilon U^2}{L}\frac{\partial\left(\tilde{u}\tilde{v}\right)}{\partial\tilde{x}} + \frac{\rho_0\varepsilon^2 U^2}{\varepsilon L}\frac{\partial\left(\tilde{v}^2\right)}{\partial\tilde{z}} + \frac{\rho_0 U^2}{\varepsilon L}\frac{\partial\tilde{p}}{\partial\tilde{z}} \\ = \frac{2\mu\varepsilon U}{\varepsilon^2 L^2}\frac{\partial}{\partial\tilde{z}}\left[\frac{\partial\tilde{v}}{\partial\tilde{z}}\right] + \frac{\mu U}{L^2}\frac{\partial}{\partial\tilde{x}}\left[\frac{1}{\varepsilon}\frac{\partial\tilde{u}}{\partial\tilde{z}} + \varepsilon\frac{\partial\tilde{v}}{\partial\tilde{x}}\right] - \rho_0\,\mathrm{g}\,.\end{aligned} \tag{3.2.2.7}$$

Multiplying each term by ${}^{\varepsilon L}/_{\rho_0 U^2}$ and noting that $\mathrm{Fro} = {}^{U}/_{\sqrt{\varepsilon\,\mathrm{g}\,L}}$, we get

$$\begin{aligned}\varepsilon^2\frac{\partial\tilde{v}}{\partial\tilde{t}} + \varepsilon^2\frac{\partial\left(\tilde{u}\tilde{v}\right)}{\partial\tilde{x}} + \varepsilon^2\frac{\partial\left(\tilde{v}^2\right)}{\partial\tilde{z}} + \frac{\partial\tilde{p}}{\partial\tilde{z}} \\ = \frac{2\mu}{\rho_0 U L}\frac{\partial}{\partial\tilde{z}}\left[\frac{\partial\tilde{v}}{\partial\tilde{z}}\right] + \frac{\mu}{\rho_0 U L}\frac{\partial}{\partial\tilde{x}}\left[\frac{\partial\tilde{u}}{\partial\tilde{z}} + \varepsilon^2\frac{\partial\tilde{v}}{\partial\tilde{x}}\right] - \frac{\varepsilon\,\mathrm{g}\,L}{U^2} \\ = \frac{2}{\mathrm{Rey}}\frac{\partial}{\partial\tilde{z}}\left[\frac{\partial\tilde{v}}{\partial\tilde{z}}\right] + \frac{1}{\mathrm{Rey}}\frac{\partial}{\partial\tilde{x}}\left[\frac{\partial\tilde{u}}{\partial\tilde{z}} + \varepsilon^2\frac{\partial\tilde{v}}{\partial\tilde{x}}\right] - \frac{1}{\mathrm{Fro}^2}.\end{aligned} \tag{3.2.2.8}$$

Grouping terms with respect to ε we have

$$\begin{aligned}\frac{\partial\tilde{p}}{\partial\tilde{z}} = -\frac{1}{\mathrm{Fro}^2} + \varepsilon\mu_0\left(\frac{\partial}{\partial\tilde{x}}\left[\frac{\partial\tilde{u}}{\partial\tilde{z}} + \varepsilon^2\frac{\partial\tilde{v}}{\partial\tilde{x}}\right] + \frac{\partial}{\partial\tilde{z}}\left[2\frac{\partial\tilde{v}}{\partial\tilde{z}}\right]\right) \\ - \varepsilon^2\left(\frac{\partial\tilde{v}}{\partial\tilde{t}} + \frac{\partial\left(\tilde{u}\tilde{v}\right)}{\partial\tilde{x}} + \frac{\partial\left(\tilde{v}^2\right)}{\partial\tilde{z}}\right).\end{aligned} \tag{3.2.2.9}$$

The overall dimensionless incompressible Navier–Stokes system thus reads as follows:

$$\operatorname{div}[\tilde{\boldsymbol{u}}] = 0, \tag{3.2.2.10}$$

$$\frac{\partial \tilde{u}}{\partial \tilde{t}} + \frac{\partial\left(\tilde{u}^2\right)}{\partial \tilde{x}} + \frac{\partial\left(\tilde{u}\tilde{v}\right)}{\partial \tilde{z}} + \frac{\partial \tilde{p}}{\partial \tilde{x}} = \frac{\partial}{\partial \tilde{z}}\left[\frac{\mu_0}{\varepsilon}\frac{\partial \tilde{u}}{\partial \tilde{z}}\right] + \varrho_1(\tilde{\boldsymbol{u}}), \tag{3.2.2.11}$$

$$\frac{\partial \tilde{p}}{\partial \tilde{z}} = -\frac{1}{\mathrm{Fro}^2} + \varrho_2(\tilde{\boldsymbol{u}}), \tag{3.2.2.12}$$

where

$$\varrho_1(\tilde{\boldsymbol{u}}) := \varepsilon\mu_0\left(2\frac{\partial^2 \tilde{u}}{\partial \tilde{x}^2} + \frac{\partial^2 \tilde{v}}{\partial \tilde{x}\partial \tilde{z}}\right) \tag{3.2.2.13}$$

and

$$\varrho_2(\tilde{\boldsymbol{u}}) := \varepsilon\mu_0\left(\frac{\partial^2 \tilde{u}}{\partial \tilde{x}\partial \tilde{z}} + \varepsilon^2\frac{\partial^2 \tilde{v}}{\partial \tilde{x}^2} + 2\frac{\partial^2 \tilde{v}}{\partial \tilde{z}^2}\right) - \varepsilon^2\left(\frac{\partial \tilde{v}}{\partial \tilde{t}} + \frac{\partial\left(\tilde{u}\tilde{v}\right)}{\partial \tilde{x}} + \frac{\partial\left(\tilde{v}^2\right)}{\partial \tilde{z}}\right). \tag{3.2.2.14}$$

Assuming $\widetilde{\boldsymbol{u}}$ has bounded second derivatives, definitions (3.2.2.13) and (3.2.2.14) formally lead to

$$\varrho_1(\tilde{\boldsymbol{u}}),\ \varrho_2(\tilde{\boldsymbol{u}}) = \mathrm{O}\left(\varepsilon\right). \tag{3.2.2.15}$$

Wet boundary

For the Navier boundary condition (3.1.1.9) on the wet boundary $\mathcal{B}$, we recall the scaling relations (3.2.1.6) and note that

$$\frac{\partial Z}{\partial x} \to \frac{\varepsilon L}{L}\frac{\partial \tilde{Z}}{\partial \tilde{x}} = \varepsilon\partial_{\tilde{x}}\tilde{Z}, \quad k_I \to f_{\tilde{I}} = \alpha\ \min(0, \tilde{I}). \tag{3.2.2.16}$$

Applying the dimensionless variables, on the left hand side we have

$$\begin{aligned}\mathrm{LHS} &= \frac{\mu\left(\frac{U}{\varepsilon L}\frac{\partial \tilde{u}}{\partial \tilde{z}} + \frac{\varepsilon U}{L}\frac{\partial \tilde{v}}{\partial \tilde{x}}\right)\left(1-\varepsilon^2(\partial_{\tilde{x}}\tilde{Z})^2\right) + 2\mu\varepsilon\left(\frac{\varepsilon U}{\varepsilon L}\frac{\partial \tilde{v}}{\partial \tilde{z}} - \frac{U}{L}\frac{\partial \tilde{u}}{\partial \tilde{x}}\right)\partial_{\tilde{x}}\tilde{Z}}{\left(1+\varepsilon^2(\partial_{\tilde{x}}\tilde{Z})^2\right)^{1/2}} \\ &= \frac{\mu U}{L}\frac{\left(\frac{1}{\varepsilon}\frac{\partial \tilde{u}}{\partial \tilde{z}} + \varepsilon\frac{\partial \tilde{v}}{\partial \tilde{x}}\right)\left(1-\varepsilon^2(\partial_{\tilde{x}}\tilde{Z})^2\right) + 2\varepsilon\left(\frac{\partial \tilde{v}}{\partial \tilde{z}} - \frac{\partial \tilde{u}}{\partial \tilde{x}}\right)\partial_{\tilde{x}}\tilde{Z}}{\left(1+\varepsilon^2(\partial_{\tilde{x}}\tilde{Z})^2\right)^{1/2}}\end{aligned} \tag{3.2.2.17}$$

while the right hand side becomes

$$\begin{aligned}\mathrm{RHS} &= \rho_0\left(UC_{\mathrm{lam}}\tilde{u} + U^2C_{\mathrm{tur}}\left(|\tilde{u}| + \varepsilon|\tilde{v}|\right)\tilde{u} - \varepsilon U^2 f_{\tilde{I}}\tilde{u}\right) \\ &\qquad + \rho_0\varepsilon^2\partial_{\tilde{x}}\tilde{Z}\left(UC_{\mathrm{lam}}\tilde{v} + U^2C_{\mathrm{tur}}\left(|\tilde{u}| + \varepsilon|\tilde{v}|\right)\tilde{v} - \varepsilon U^2 f_{\tilde{I}}\tilde{v}\right) \\ &= \rho_0 U\left(C_{\mathrm{lam}}\tilde{u} + UC_{\mathrm{tur}}\left(|\tilde{u}| + \varepsilon|\tilde{v}|\right)\tilde{u} - \varepsilon U f_{\tilde{I}}\tilde{u}\right) \\ &\qquad + \rho_0 U\varepsilon^2\partial_{\tilde{x}}\tilde{Z}\left(C_{\mathrm{lam}}\tilde{v} + UC_{\mathrm{tur}}\left(|\tilde{u}| + \varepsilon|\tilde{v}|\right)\tilde{v} - \varepsilon U f_{\tilde{I}}\tilde{v}\right).\end{aligned} \tag{3.2.2.18}$$

Equating and simplifying we have

$$\frac{\mu}{\rho_0 L}\left(\frac{1}{\varepsilon}\partial_{\tilde{z}}\tilde{u}+\varepsilon\partial_{\tilde{x}}\tilde{v}\right)+\frac{2\mu\varepsilon}{\rho_0 L}\frac{\partial_{\tilde{x}}\tilde{Z}\left(\partial_{\tilde{z}}\tilde{v}-\partial_{\tilde{x}}\tilde{u}\right)}{1-\varepsilon^2(\partial_{\tilde{x}}\tilde{Z})^2}$$

$$=\left(C_{\text{lam}}\tilde{u}+UC_{\text{tur}}\left(|\tilde{u}|+\varepsilon|\tilde{v}|\right)\tilde{u}-\varepsilon U f_{\tilde{I}}\tilde{u}\right)\frac{\sqrt{1+\varepsilon^2(\partial_{\tilde{x}}\tilde{Z})^2}}{1-\varepsilon^2(\partial_{\tilde{x}}\tilde{Z})^2}$$

$$+\varepsilon^2\partial_{\tilde{x}}\tilde{Z}\left(C_{\text{lam}}\tilde{v}+UC_{\text{tur}}\left(|\tilde{u}|+\varepsilon|\tilde{v}|\right)\tilde{v}-\varepsilon U f_{\tilde{I}}\tilde{v}\right)\frac{\sqrt{1+\varepsilon^2(\partial_{\tilde{x}}\tilde{Z})^2}}{1-\varepsilon^2(\partial_{\tilde{x}}\tilde{Z})^2}.$$

Moving all terms of order ε and above to the right hand side and dividing by U, we get

$$\frac{\mu}{\rho_0 UL}\frac{\partial_{\tilde{z}}\tilde{u}}{\varepsilon}=-\frac{\varepsilon\mu}{\rho_0 UL}\left(\partial_{\tilde{x}}\tilde{v}+\frac{2\partial_{\tilde{x}}\tilde{Z}\left(\partial_{\tilde{z}}\tilde{v}-\partial_{\tilde{x}}\tilde{u}\right)}{1-\varepsilon^2(\partial_{\tilde{x}}\tilde{Z})^2}\right)$$

$$+\left(\frac{C_{\text{lam}}}{U}\tilde{u}+C_{\text{tur}}\left(|\tilde{u}|+\varepsilon|\tilde{v}|\right)\tilde{u}-\varepsilon f_{\tilde{I}}\tilde{u}\right)\frac{\sqrt{1+\varepsilon^2(\partial_{\tilde{x}}\tilde{Z})^2}}{1-\varepsilon^2(\partial_{\tilde{x}}\tilde{Z})^2}$$

$$+\varepsilon^2\partial_{\tilde{x}}\tilde{Z}\left(\frac{C_{\text{lam}}}{U}\tilde{v}+C_{\text{tur}}\left(|\tilde{u}|+\varepsilon|\tilde{v}|\right)\tilde{v}-\varepsilon f_{\tilde{I}}\tilde{v}\right)\frac{\sqrt{1+\varepsilon^2(\partial_{\tilde{x}}\tilde{Z})^2}}{1-\varepsilon^2(\partial_{\tilde{x}}\tilde{Z})^2}.$$

Recalling that $\text{Rey}=\rho_0 UL/\mu$, this becomes

$$\left[\frac{\partial_{\tilde{z}}\tilde{u}}{\varepsilon\text{Rey}}\right]_{\mathcal{B}}=\underbrace{-\frac{\varepsilon}{\text{Rey}}\left(\partial_{\tilde{x}}\tilde{v}+\frac{2\partial_{\tilde{x}}\tilde{Z}\left(\partial_{\tilde{z}}\tilde{v}-\partial_{\tilde{x}}\tilde{u}\right)}{1-\varepsilon^2(\partial_{\tilde{x}}\tilde{Z})^2}\right)}_{\phi_1(\tilde{\boldsymbol{u}})=\text{O}(\varepsilon/\text{Rey})}$$

$$+\left(\frac{C_{\text{lam}}}{U}\tilde{u}+C_{\text{tur}}\left(|\tilde{u}|+\varepsilon|\tilde{v}|\right)\tilde{u}-\varepsilon f_{\tilde{I}}\tilde{u}\right)\frac{\sqrt{1+\varepsilon^2(\partial_{\tilde{x}}\tilde{Z})^2}}{1-\varepsilon^2(\partial_{\tilde{x}}\tilde{Z})^2}$$

$$\underbrace{+\varepsilon^2\partial_{\tilde{x}}\tilde{Z}\left(\frac{C_{\text{lam}}}{U}\tilde{v}+C_{\text{tur}}\left(|\tilde{u}|+\varepsilon|\tilde{v}|\right)\tilde{v}-\varepsilon f_{\tilde{I}}\tilde{v}\right)\frac{\sqrt{1+\varepsilon^2(\partial_{\tilde{x}}\tilde{Z})^2}}{1-\varepsilon^2(\partial_{\tilde{x}}\tilde{Z})^2}}_{\phi_2(\tilde{\boldsymbol{u}})=\text{O}(\varepsilon^2)}.$$

Thus we have

$$\left[\frac{\partial_{\tilde{z}}\tilde{u}}{\varepsilon\text{Rey}}\right]_{\mathcal{B}}=\left(\frac{C_{\text{lam}}}{U}\tilde{u}+C_{\text{tur}}\left(|\tilde{u}|+\varepsilon|\tilde{v}|\right)\tilde{u}-\varepsilon f_{\tilde{I}}\tilde{u}\right)\frac{\sqrt{1+\varepsilon^2(\partial_{\tilde{x}}\tilde{Z})^2}}{1-\varepsilon^2(\partial_{\tilde{x}}\tilde{Z})^2}+\text{O}\left(\varepsilon/\text{Rey}\right)+\text{O}\left(\varepsilon^2\right).$$

Applying the non-dimensional friction factors

$$C_{\text{lam}}\mapsto\varepsilon UC_{\text{lam},\varepsilon}\quad\text{and}\quad C_{\text{tur}}\mapsto\varepsilon C_{\text{tur},\varepsilon}\tag{3.2.2.19}$$

we get

$$\left[\frac{\partial_{\tilde{z}}\tilde{u}}{\varepsilon\text{Rey}}\right]_{\mathcal{B}}=\varepsilon\left(C_{\text{lam},\varepsilon}\tilde{u}+C_{\text{tur},\varepsilon}\left(|\tilde{u}|+\varepsilon|\tilde{v}|\right)\tilde{u}-f_{\tilde{I}}\tilde{u}\right)\frac{\sqrt{1+\varepsilon^2(\partial_{\tilde{x}}\tilde{Z})^2}}{1-\varepsilon^2(\partial_{\tilde{x}}\tilde{Z})^2}+\text{O}\left(\varepsilon/\text{Rey}\right)+\text{O}\left(\varepsilon^2\right).$$

In evaluating the first term, we want to group together terms of $\mathrm{O}(\varepsilon)$, whilst those of higher order will be absorbed into the existing $\mathrm{O}(\varepsilon^2)$. The first component can be divided as

$$\underbrace{\varepsilon\left(C_{\mathrm{lam},\varepsilon}\tilde{u}+C_{\mathrm{tur},\varepsilon}|\tilde{u}|\tilde{u}-f_{\tilde{I}}\tilde{u}\right)}_{\mathrm{O}(\varepsilon)}+\underbrace{\varepsilon^2\left(C_{\mathrm{tur},\varepsilon}|\tilde{v}|\tilde{u}\right)}_{\mathrm{O}(\varepsilon^2)}. \tag{3.2.2.20}$$

For the second component, we simply note that it can be expanded as 1 + higher order terms; the higher order terms when multiplied with the first component will all be absorbed into $\mathrm{O}(\varepsilon^2)$, as will the $\varepsilon^2\left(C_{\mathrm{tur},\varepsilon}|\tilde{v}|\tilde{u}\right)$ term, leaving

$$\begin{aligned}\left[\frac{\partial_{\tilde{z}}\tilde{u}}{\varepsilon\mathrm{Rey}}\right]_{\mathcal{B}} &= \varepsilon\underbrace{\left(C_{\mathrm{lam},\varepsilon}\tilde{u}+C_{\mathrm{tur},\varepsilon}|\tilde{u}|\tilde{u}-f_{\tilde{I}}\tilde{u}\right)}_{=\left(k_0(\tilde{u})-f_{\tilde{I}}\right)\tilde{u}}+\mathrm{O}\left(\varepsilon/\mathrm{Rey}\right)+\mathrm{O}\left(\varepsilon^2\right)\\ &= \varepsilon\left(k_0(\tilde{u})-f_{\tilde{I}}\right)\tilde{u}+\mathrm{O}\left(\varepsilon^2\right)\end{aligned} \tag{3.2.2.21}$$

with *asymptotic friction laws*

$$\begin{aligned}k_0(\xi) &:= C_{\mathrm{lam},0}+C_{\mathrm{tur},0}|\xi| \text{ for } \xi\in\mathbb{R}\\ f_{\tilde{I}} &:= \alpha\ \min(0,\tilde{I}).\end{aligned} \tag{3.2.2.22}$$

For the permeable boundary condition (3.1.1.11), applying our dimensionless variables we get

$$\begin{aligned}\varepsilon U\tilde{v}-U\tilde{u}\cdot\varepsilon\partial_{\tilde{x}}\tilde{Z}+\varepsilon U\tilde{I}\sqrt{1+\varepsilon^2(\partial_{\tilde{x}}\tilde{Z})^2}=0\\ \tilde{v}-\tilde{u}\partial_{\tilde{x}}\tilde{Z}+\tilde{I}+\mathrm{O}\left(\varepsilon\right)=0.\end{aligned} \tag{3.2.2.23}$$

Free surface

For the boundary conditions on the free surface $\mathcal{F}$, applying our non-dimensionalisation approach to the kinematic boundary condition (3.1.2.4) we derive

$$\partial_{\tilde{t}}\tilde{H}+u\partial_{\tilde{x}}\tilde{H}-\tilde{v}=\tilde{R} \tag{3.2.2.24}$$

while we can non-dimensionalise (3.1.2.8) in the same manner as the Navier boundary condition (3.1.1.9) on the wet boundary $\mathcal{B}$, giving

$$\left[\frac{\partial_{\tilde{z}}\tilde{u}}{\varepsilon\mathrm{Rey}}\right]_{\mathcal{F}}=-\varepsilon f_{\tilde{R}}\tilde{u}+\mathrm{O}\left(\varepsilon^2\right) \tag{3.2.2.25}$$

with free surface asymptotic friction law

$$f_{\tilde{R}}=\alpha\tilde{R} \text{ for } \alpha\in\mathbb{R}. \tag{3.2.2.26}$$

3.2.3 First order approximation of the dimensionless Navier–Stokes

Before considering the first order approximation that will lead to the shallow water equations, we recall the system of equations and boundary conditions that we non-dimensionalised in the previous section:

Navier–Stokes

$$\begin{aligned} \operatorname{div}[\tilde{\boldsymbol{u}}] &= 0 \\ \frac{\partial \tilde{u}}{\partial \tilde{t}} + \frac{\partial\left(\tilde{u}^2\right)}{\partial \tilde{x}} + \frac{\partial(\tilde{u}\tilde{v})}{\partial \tilde{z}} + \frac{\partial \tilde{p}}{\partial \tilde{x}} &= \frac{\partial}{\partial \tilde{z}}\left[\frac{\mu_0}{\varepsilon}\frac{\partial \tilde{u}}{\partial \tilde{z}}\right] + \mathrm{O}(\varepsilon) \\ \frac{\partial \tilde{p}}{\partial \tilde{z}} &= -\frac{1}{\mathrm{Fro}^2} + \mathrm{O}(\varepsilon) \end{aligned} \tag{3.2.3.1}$$

Wet boundary $\mathcal{B}$

$$\begin{aligned} \left[\frac{\partial_{\tilde{z}}\tilde{u}}{\varepsilon \mathrm{Rey}}\right]_{\mathcal{B}} &= \varepsilon\left(k_0(\tilde{u}) - f_{\tilde{I}}\right)\tilde{u} + \mathrm{O}\left(\varepsilon^2\right) \\ \tilde{v} - \tilde{u}\partial_{\tilde{x}}\tilde{Z} + \tilde{I} &= \mathrm{O}(\varepsilon) \end{aligned} \tag{3.2.3.2}$$

Free surface $\mathcal{F}$

$$\begin{aligned} \left[\frac{\partial_{\tilde{z}}\tilde{u}}{\varepsilon \mathrm{Rey}}\right]_{\mathcal{F}} &= -\varepsilon f_{\tilde{R}}\tilde{u} + \mathrm{O}\left(\varepsilon^2\right) \\ \partial_{\tilde{t}}\tilde{H} + u\partial_{\tilde{x}}\tilde{H} - \tilde{v} &= \tilde{R} \end{aligned} \tag{3.2.3.3}$$

Dropping all terms of order ε and higher in equations (3.2.3.1), (3.2.3.2), and (3.2.3.3) (and dropping the $\tilde{\cdot}$ throughout for brevity), we deduce the following *hydrostatic approximation* of the dimensionless Navier–Stokes system:

$$\partial_x u_\varepsilon + \partial_z v_\varepsilon = 0 \tag{3.2.3.4}$$

$$\partial_t u_\varepsilon + \partial_x\left[u_\varepsilon^2\right] + \partial_z[u_\varepsilon v_\varepsilon] + \partial_x p_\varepsilon = \partial_z\left[\frac{\mu_0}{\varepsilon}\partial_z u_\varepsilon\right] \tag{3.2.3.5}$$

$$\partial_z p_\varepsilon = -\frac{1}{\mathrm{Fro}^2} \tag{3.2.3.6}$$

whilst the boundary conditions, as a result of the asymptotic setting $\mathrm{Rey}^{-1} = \varepsilon\mu_0$, simplify to

$$\left[\frac{\mu_0}{\varepsilon}\partial_z u_\varepsilon\right] = \left(k_0(u_\varepsilon) - k_I\right)u_\varepsilon \quad \text{and} \quad v_\varepsilon = u_\varepsilon\partial_x Z - I \text{ on } \mathcal{B}, \tag{3.2.3.7}$$

and

$$\left[\frac{\mu_0}{\varepsilon}\partial_z u_\varepsilon\right] = -k_R u_\varepsilon \quad \text{and} \quad \partial_t H + u_\varepsilon\partial_x H - v_\varepsilon = R \text{ on } \mathcal{F}. \tag{3.2.3.8}$$

Here, $(u_\varepsilon, v_\varepsilon, p_\varepsilon)$ represents the solution of the first-order dimensionless Navier-Stokes system.

Vertically integrating (3.2.3.6) over $[z, H(x,t)]$, we obtain the hydrostatic pressure

$$p_\varepsilon(x,t,H) - p_\varepsilon(x,t,z) = -\frac{1}{\mathrm{Fro}^2}(H - z). \tag{3.2.3.9}$$

We assume that the pressure exerted on the free surface $p_\varepsilon(x,t,H) = p_c$ for some constant $p_c \in \mathbb{R}$ (as we neglected all other meteorological phenomena), and thus the equation becomes

$$p_\varepsilon(x,t,z) = \frac{1}{\mathrm{Fro}^2}(H - z) + p_c \tag{3.2.3.10}$$

Identifying terms at order $1/\varepsilon$ in (3.2.3.5), (3.2.3.7), and (3.2.3.8), we can decompose the function u_ε as

$$u_\varepsilon(x,t,z) = u_0(x,t) + \mathrm{O}(\varepsilon) \tag{3.2.3.11}$$

for some function $u_0(x,t)$, as a consequence of

$$\partial_z[\mu_0\partial_z u_\varepsilon] = \mathrm{O}(\varepsilon)\,,\ [\mu_0\partial_z u_\varepsilon]_{\mathcal{B}} = \mathrm{O}(\varepsilon)\,,\ \text{and}\ [\mu_0\partial_z u_\varepsilon]_{\mathcal{F}} = \mathrm{O}(\varepsilon)\,. \tag{3.2.3.12}$$

Noting $\langle u_\varepsilon(x,t)\rangle$ as the mean speed of the fluid over the section $[Z(x), H(x,t)]$,

$$\langle u_\varepsilon(x,t)\rangle = \frac{1}{h(x,t)}\int_{Z(x)}^{H(x,t)} u_\varepsilon(t,x,z)dz, \tag{3.2.3.13}$$

one can use the following approximations at first order:

$$u_\varepsilon(x,t,z) = \langle u_\varepsilon(x,t)\rangle + \mathrm{O}(\varepsilon)\ \text{ and }\ \left\langle u_\varepsilon(x,t)^2\right\rangle = \langle u_\varepsilon(x,t)\rangle^2 + \mathrm{O}(\varepsilon)\,. \tag{3.2.3.14}$$

3.2.4 Shallow water system with recharge

To derive the conservation of mass equation, there are two points we must first recall; the first is the definition of the indicator function for the wet region, given by

$$\Phi(x,t,z) := \mathbb{I}[Z(x) \le z \le H(x,t)]\ \text{ for all } x,t,z \in \mathbb{R}. \tag{3.2.4.1}$$

The second is Leibniz's rule, which states that for a function $f(x,t)$,

$$\int_{a(t)}^{b(t)} \frac{\partial f}{\partial t}dx = \partial_t\left[\int_{a(t)}^{b(t)} f(x,t)dx\right] + f(a(t),t)\cdot\partial_t a - f(b(t),t)\cdot\partial_t b. \tag{3.2.4.2}$$

With these in place, we can integrate the indicator transport equation (3.1.0.10) for $z \in [Z(x), H(x,t)]$:

$$\int_{Z(x)}^{H(x,t)} \partial_t\Phi + \partial_x[\Phi u_\varepsilon] + \partial_z[\Phi v_\varepsilon]\,dz = 0. \tag{3.2.4.3}$$

Considering each integral individually, we have

$$\begin{aligned}\int_{Z(x)}^{H(x,t)} \partial_t\Phi dz &= \partial_t\int_{Z(x)}^{H(x,t)} \Phi dz + [\Phi]_{\mathcal{B}}\underbrace{\partial_t Z}_{=0} - [\Phi]_{\mathcal{F}}\,\partial_t H \\ &= \partial_t h - [\partial_t H]_{\mathcal{B}}\end{aligned} \tag{3.2.4.4}$$

$$\begin{aligned}\int_{Z(x)}^{H(x,t)} \partial_x[\Phi u_\varepsilon]\,dz &= \partial_x\int_{Z(x)}^{H(x,t)} \Phi u_\varepsilon dz + [\Phi u_\varepsilon]_{\mathcal{B}}\,\partial_x Z - [\Phi u_\varepsilon]_{\mathcal{F}}\,\partial_x H \\ &= \partial_x[hu_\varepsilon] + [u_\varepsilon\partial_x Z]_{\mathcal{B}} - [u_\varepsilon\partial_x H]_{\mathcal{F}}\end{aligned} \tag{3.2.4.5}$$

and

$$\int_{Z(x)}^{H(x,t)} \partial_z[\Phi v_\varepsilon]\,dz = [v_\varepsilon]_{\mathcal{F}} - [v_\varepsilon]_{\mathcal{B}} \tag{3.2.4.6}$$

Grouping these terms together, we get

$$\partial_t h + \partial_x q - [\partial_t H + u_\varepsilon\partial_x H - v_\varepsilon]_{\mathcal{B}} + [u_\varepsilon\partial_x Z - v_\varepsilon]_{\mathcal{F}} = 0 \tag{3.2.4.7}$$

where, in view of (3.2.3.14), the discharge q is defined as

$$q(x,t) := \langle u_\varepsilon(x,t)\rangle\, h(x,t). \tag{3.2.4.8}$$

From the penetration condition (3.2.3.7) and kinematic boundary condition (3.2.3.8), we deduce the conservation of mass equation

$$\partial_t h + \partial_x q = S \tag{3.2.4.9}$$

where the source term $S := R - I$ measures the gain or loss of water through the rainfall and infiltration rates, respectively.

Recalling the pressure equation (3.2.3.10) and making use of boundary conditions (3.2.3.7) and (3.2.3.8) once again, the left hand side of (3.2.3.5) can be integrated as follows:

$$\int_{Z(x)}^{H(x,t)} \text{LHS}\; dz = \int_{Z(x)}^{H(x,t)} \partial_t u_\varepsilon + \partial_x\left[u_\varepsilon^2\right] + \partial_z[u_\varepsilon v_\varepsilon] + \partial_x p\; dx. \tag{3.2.4.10}$$

As we did in deriving the conservation of mass equation, we will consider each integral in turn:

$$\begin{aligned}
\int_{Z(x)}^{H(x,t)} \partial_t u_\varepsilon\; dz &= \partial_t \int_{Z(x)}^{H(x,t)} u_\varepsilon dz + [u_\varepsilon]_{\mathcal{B}} \underbrace{\partial_t Z}_{=0} - [u_\varepsilon]_{\mathcal{F}}\, \partial_t H \\
&= \partial_t \left(u_\varepsilon \left[z\right]\Big|_{Z(x)}^{H(x,t)} \right) - [u_\varepsilon]_{\mathcal{F}}\, \partial_t H \\
&= \partial_t \Big(u_\varepsilon \underbrace{\Big[H(x,t) - Z(x)\Big]}_{=h(t,x)} \Big) - [u_\varepsilon]_{\mathcal{F}}\, \partial_t H \\
&= \partial_t q - [u_\varepsilon]_{\mathcal{F}}\, \partial_t H
\end{aligned} \tag{3.2.4.11}$$

$$\begin{aligned}
\int_{Z(x)}^{H(x,t)} \frac{\partial u_\varepsilon^2}{\partial t} dz &= \partial_x \int_{Z(x)}^{H(x,t)} u_\varepsilon^2 dz + \left[u_\varepsilon^2\right]_{\mathcal{B}} \partial_x Z - \left[u_\varepsilon^2\right]_{\mathcal{F}} \partial_x H \\
&= \partial_x \left(q^2/h\right) + \left[u_\varepsilon^2\right]_{\mathcal{B}} \partial_x Z - \left[u_\varepsilon^2\right]_{\mathcal{F}} \partial_x H
\end{aligned} \tag{3.2.4.12}$$

and

$$\int_{Z(x)}^{H(x,t)} \partial_z[u_\varepsilon v_\varepsilon]\; dz = [u_\varepsilon v_\varepsilon]_{\mathcal{F}} - [u_\varepsilon v_\varepsilon]_{\mathcal{B}} \tag{3.2.4.13}$$

For the last integral, we first recall the definition of the pressure (3.2.3.10):

$$p_\varepsilon(x,t,z) = \frac{1}{\text{Fro}^2}\,(H - z) + p_c. \tag{3.2.4.14}$$

The integral thus becomes:

$$\begin{aligned}
\int_{Z(x)}^{H(x,t)} \partial_x p_\varepsilon\; dz &= \partial_x \int_{Z(x)}^{H(x,t)} p_\varepsilon dz + [p_\varepsilon]_{\mathcal{B}}\, \partial_x Z - [p_\varepsilon]_{\mathcal{F}}\, \partial_x H \\
&= \partial_x \int_{Z(x)}^{H(x,t)} \left[\frac{1}{\text{Fro}^2}(H - z) + p_c\right] dz + \frac{h}{\text{Fro}^2}\partial_x Z + p_c \partial_x Z - p_c \partial_x H \\
&= \frac{1}{\text{Fro}^2}\partial_x \int_{Z(x)}^{H(x,t)} (H - z) dz + \frac{h}{\text{Fro}^2}\partial_x Z \\
&\quad + \underbrace{\partial_x \int_{Z(x)}^{H(x,t)} p_c dz + p_c \partial_x Z - p_c \partial_x H}_{=0}
\end{aligned}$$

which integrates to

$$\begin{aligned}\int_{Z(x)}^{H(x,t)} \partial_x p_\varepsilon \, dz &= \frac{1}{\mathrm{Fro}^2}\partial_x \left[H(x,t)z - \frac{z^2}{2}\right]\Big|_{Z(x)}^{H(x,t)} + \frac{h}{\mathrm{Fro}^2}\partial_x Z \\ &= \frac{1}{\mathrm{Fro}^2}\partial_x \left(H^2 - \frac{H^2}{2} - HZ + \frac{Z^2}{2}\right) + \frac{h}{\mathrm{Fro}^2}\partial_x Z \\ &= \frac{1}{\mathrm{Fro}^2}\partial_x \left(\frac{(H-Z)^2}{2}\right) + \frac{h}{\mathrm{Fro}^2}\partial_x Z \\ &= \partial_x \left(\frac{h^2}{2\mathrm{Fro}^2}\right) + \frac{h}{\mathrm{Fro}^2}\partial_x Z.\end{aligned} \tag{3.2.4.15}$$

Grouping terms together, we have

$$\begin{aligned}\int_{Z(x)}^{H(x,t)} \mathrm{LHS} \, dz &= \partial_t q + \partial_x \left[\frac{q^2}{h} + \frac{h^2}{2\mathrm{Fro}^2}\right] + \frac{h^2}{\mathrm{Fro}^2}\partial_x Z \\ &\quad - \left[\left(\partial_t H + u_\varepsilon \partial_x H - v_\varepsilon\right) u_\varepsilon\right]_{\mathcal{B}} + \left[\left(u_\varepsilon \partial_x Z - v_\varepsilon\right) u_\varepsilon\right]_{\mathcal{F}} \\ &= \partial_t q + \partial_x \left[\frac{q^2}{h} + \frac{h^2}{2\mathrm{Fro}^2}\right] + \frac{h^2}{\mathrm{Fro}^2}\partial_x Z \\ &\quad - \left[R u_\varepsilon\right]_{\mathcal{B}} + \left[I u_\varepsilon\right]_{\mathcal{F}} \\ &= \partial_t q + \partial_x \left[\frac{q^2}{h} + \frac{h^2}{2\mathrm{Fro}^2}\right] + \frac{h^2}{\mathrm{Fro}^2}\partial_x Z - S\frac{q}{h}\end{aligned} \tag{3.2.4.16}$$

where S is again defined as above. Integrating the right hand side of (3.2.3.5) using (3.2.3.7) and (3.2.3.8), we obtain

$$\begin{aligned}\int_{Z(x)}^{H(x,t)} \mathrm{RHS} \, dz &= \left[\frac{\mu_0}{\varepsilon}\partial_z u_\varepsilon\right]_{\mathcal{F}} - \left[\frac{\mu_0}{\varepsilon}\partial_z u_\varepsilon\right]_{\mathcal{B}} \\ &= -\left[k_R u_\varepsilon\right]_{\mathcal{F}} + \left[\left(k_0(u_\varepsilon) - k_I\right) u_\varepsilon\right]_{\mathcal{B}} \\ &= -\left(k_R - k_I + k_0\left(\frac{q}{h}\right)\right)\frac{q}{h}\end{aligned} \tag{3.2.4.17}$$

where the friction factors k_R, k_I, and k_0 are defined as in (3.2.2.26) and (3.2.2.22), respectively. Multiplying each side of (3.2.4.9), (3.2.4.16), and (3.2.4.17) by $\rho_0 U^2/D$, we derive the shallow water system with recharge:

$$\begin{aligned}\partial_t h + \partial_x q &= S \\ \partial_t q + \partial_x \left[\frac{q^2}{h} + \mathrm{g}\,\frac{h^2}{2}\right] &= -\,\mathrm{g}\,h\partial_x Z + S\frac{q}{h} - \left(k_R - k_I + k_0\left(\frac{q}{h}\right)\right)\frac{q}{h} \\ \text{where } q &= hu\,.\end{aligned} \tag{3.2.4.18}$$

3.3 Extended shallow water theorem

We will now consider several properties of the extended shallow water system, (3.2.4.18), and consider how these properties compare to the existing model. Most notably, we will see how the condition for the model to be well-posed differs depending upon the existence of the additional Sq/h term in the conservation of momentum equation.

3.3.1 Theorem (stability and entropy relation)

(a) *System* (3.2.4.18) *is strictly hyperbolic on the set* $\{h > 0\}$.

(b) *For smooth solution* (h, u)*, the mean velocity* $u = q/h$ *satisfies:*

$$\partial_t u + \partial_x \psi(x, h, u) = -\frac{(k_R - k_I + k_0(u))\, u}{h} \tag{3.3.1.1}$$

where $\psi(x, h, u) = \frac{u^2}{2} + \mathrm{g}\, h + \mathrm{g}\, Z$ *is the total head.*

(c) *For smooth solutions, the still water steady state reads*

$$u = S = 0 \text{ and } h + Z = h_0 \text{ for some constant } h_0 > 0. \tag{3.3.1.2}$$

(d) *System* (3.2.4.18) *admits a mathematical entropy*

$$E(h, u) = \frac{hu^2}{2} + \frac{\mathrm{g}\, h^2}{2} \tag{3.3.1.3}$$

which satisfies the reference-frame invariant entropy relation for smooth solutions

$$\begin{aligned} \partial_t E + \partial_x \left[\left(E + \frac{\mathrm{g}\, h^2}{2} \right) u \right] = S \left(\frac{u^2}{2} + \mathrm{g}\, h \right) - \mathrm{g}\, hu \partial_x Z \\ - (k_R - k_I + k_0(u))\, u^2. \end{aligned} \tag{3.3.1.4}$$

Proof. The proof of these assumptions follows after some manipulations of the two equations of system (3.2.4.18). We consider each statement in turn.

(a) The Jacobian of the flux function is given by

$$\boldsymbol{J}(h, q) := \begin{bmatrix} 0 & 1 \\ -q^2/h^2 + \mathrm{g}\, h & 2q/h \end{bmatrix}. \tag{3.3.1.5}$$

To calculate the eigenvalues of the Jacobian, we need to solve the quadratic equation

$$\begin{aligned} 0 = \det\left(\boldsymbol{J}(h, q) - \lambda \mathbb{I}_n\right) = \begin{vmatrix} 0 - \lambda & 1 \\ -q^2/h^2 + \mathrm{g}\, h & 2q/h - \lambda \end{vmatrix} \\ = \lambda^2 - 2q/h \lambda + \left(q^2/h^2 - \mathrm{g}\, h\right), \end{aligned} \tag{3.3.1.6}$$

whose solutions are given by

$$\lambda_{1,2} = \frac{\frac{2q}{h} \pm \sqrt{\frac{4q^2}{h^2} - \frac{4q^2}{h^2} + 4\,\mathrm{g}\, h}}{2} = \frac{q}{h} \pm \sqrt{\mathrm{g}\, h}. \tag{3.3.1.7}$$

Our eigenvalues are therefore

$$\lambda_1(h, q) = q/h + \sqrt{\mathrm{g}\, h} \text{ and } \lambda_2(h, q) \quad = q/h - \sqrt{\mathrm{g}\, h}. \tag{3.3.1.8}$$

For these eigenvalues to exist and be real, we require that $h > 0$; the diagonalizability of the Jacobian (3.3.1.5) follows from the eigenvalues being necessarily distinct for $h > 0$. We can conclude, therefore, that the extended shallow water system is hyperbolic on the set $\{h > 0\}$.

(b) We rewrite the conservation of momentum equation in terms of (h, u) rather than (h, q) to give

$$\partial_t[hu] + \partial_x\left[hu^2 + \frac{\mathrm{g}\,h^2}{2}\right] = -\,\mathrm{g}\,h\partial_x Z + Su - (k_R - k_I + k_0(u))\,u. \quad (3.3.1.9)$$

Applying the product rule to the first term of (3.3.1.9) and substituting in the conservation of mass equation, we get

$$\begin{aligned} h\partial_t u + u\,(S - \partial_x[hu]) + \partial_x\left[hu^2\right] + \partial_x\left[\frac{\mathrm{g}\,h^2}{2}\right] \\ = -\,\mathrm{g}\,h\partial_x Z + Su - (k_R - k_I + k_0(u))\,u, \end{aligned} \quad (3.3.1.10)$$

from which we can cancel Su on both sides. Using the product rule again, we have that

$$u\partial_x[hu] = \partial_x\left[hu^2\right] - hu\partial_x u, \quad (3.3.1.11)$$

which can be substituted into (3.3.1.10) to give

$$\begin{aligned} h\partial_t u - \partial_x\left[hu^2\right] + hu\partial_x u + \partial_x\left[hu^2\right] + \partial_x\left[\frac{\mathrm{g}\,h^2}{2}\right] \\ = -\,\mathrm{g}\,h\partial_x Z - (k_R - k_I + k_0(u))\,u, \end{aligned} \quad (3.3.1.12)$$

enabling us to now cancel $\partial_x[hu^2]$. Noting that

$$\partial_x\left[\frac{\mathrm{g}\,h^2}{2}\right] = h\partial_x[\mathrm{g}\,h]\,, \quad (3.3.1.13)$$

we can substitute this into (3.3.1.12) and divide by h throughout to get

$$\partial_t u + u\partial_x u + \partial_x[\mathrm{g}\,h] = -\,\mathrm{g}\,\partial_x Z - \frac{(k_R - k_I + k_0(u))\,u}{h}. \quad (3.3.1.14)$$

Making a final substitution of

$$u\partial_x u = \partial_x u^2/2 \quad (3.3.1.15)$$

and grouping derivatives of x, we have

$$\partial_t u + \partial_x \psi(x, h, u) = -\frac{(k_R - k_I + k_0(u))\,u}{h} \quad (3.3.1.16)$$

where $\psi(x, h, u) = \frac{u^2}{2} + \mathrm{g}\,h + \mathrm{g}\,Z$, as required.

(c) Setting $u = 0$ in equation (3.3.1.1), we have

$$\partial_x \psi = \partial_x[\mathrm{g}\,h + \mathrm{g}\,Z] = 0, \quad (3.3.1.17)$$

which is strictly constant, thereby yielding the lake-at-rest steady state.

(d) We begin by noting that

$$\left(E + \frac{\mathrm{g}\,h^2}{2}\right) u = (\psi - \mathrm{g}\,Z)\,hu \quad (3.3.1.18)$$

and hence

$$\begin{aligned}\partial_t E + \partial_x\left[\left(E + \frac{\mathrm{g}\,h^2}{2}\right)u\right] &= \partial_t E + \partial_x[\psi hu] - \partial_x[\mathrm{g}\,huZ] \\ &= \partial_t E + hu\partial_x\psi + \psi\partial_x[hu] - \partial_x[\mathrm{g}\,huZ]\,.\end{aligned} \tag{3.3.1.19}$$

Through a rearrangement of property (b), we have

$$hu\partial_x\psi = -(k_R - k_I + k_0\,(u))u^2 - hu\partial_t u, \tag{3.3.1.20}$$

and so equation (3.3.1.19) becomes

$$\partial_t E - (k_R - k_I + k_0(u))\,u^2 - (hu)\,\partial_t u + \psi\partial_x[hu] - \partial_x[\mathrm{g}\,huZ]\,. \tag{3.3.1.21}$$

Next we substitute

$$(hu)\,\partial_t u = u\partial_t[hu] - u^2\partial_t h\partial_x[\mathrm{g}\,huZ] = \mathrm{g}\,hu\partial_x Z + \mathrm{g}\,Z\partial_x[hu] \tag{3.3.1.22}$$

to give

$$\begin{aligned}\partial_t E - u\partial_t[hu] + u^2\partial_t h + \psi\partial_x[hu] - \mathrm{g}\,hu\partial_x Z \\ - \mathrm{g}\,Z\partial_x[hu] - (k_R - k_I + k_0(u))\,u^2.\end{aligned} \tag{3.3.1.23}$$

From the definition of E, (3.3.1.3), we note that $E = (\psi - {}^{gh}/_2 - \mathrm{g}\,Z)\,h$, and hence

$$\begin{aligned}\partial_t E &= \partial_t\left[\left(\psi - \frac{gh}{2}\right)h\right] - \partial_t[\mathrm{g}\,hZ] \\ &= h\partial_t\left[\psi - \frac{gh}{2}\right] + \left(\psi - \frac{gh}{2}\right)\partial_t h - \partial_t[\mathrm{g}\,hZ] \\ &= h\partial_t\left[\psi - \frac{gh}{2}\right] + \psi\partial_t h - \frac{gh}{2}\partial_t h - \partial_t[\mathrm{g}\,hZ]\,.\end{aligned} \tag{3.3.1.24}$$

Substituting (3.3.1.24) into (3.3.1.23), we have

$$\begin{aligned}&h\partial_t\left[\psi - \frac{gh}{2}\right] - \frac{gh}{2}\partial_t h - u\partial_t[hu] + u^2\partial_t h \\ &+ \underbrace{\psi\,(\partial_t h + \partial_x[hu]) - \mathrm{g}\,Z\,(\partial_t h + \partial_x[hu]) - \mathrm{g}\,hu\partial_x Z - (k_R - k_I + k_0(u))\,u^2}_{=S(u^2/2+\mathrm{g}\,h)-\mathrm{g}\,hu\partial_x Z-(k_R-k_I+k_0(u))u^2}\,.\end{aligned}$$

To conclude the proof we need to show that the terms in the first line all cancel. Expanding the first derivative, we have

$$\begin{aligned}h\partial_t\psi - h\partial_t\left[\frac{gh}{2}\right] - \frac{gh}{2}\partial_t h - u\partial_t[hu] + u^2\partial_t h \\ = h\partial_t\psi - h\partial_t[gh] - u\partial_t[hu] + u^2\partial_t h.\end{aligned} \tag{3.3.1.25}$$

The last two terms can be rewritten as

$$\begin{aligned}u^2\partial_t h &= \partial_t\left[hu^2\right] - h\partial_t\left[u^2\right] = \partial_t\left[hu^2\right] - 2(hu)\partial_t u \\ u\partial_t[hu] &= \partial_t\left[hu^2\right] - (hu)\partial_t u.\end{aligned} \tag{3.3.1.26}$$

Substituting and cancelling, (3.3.1.25) becomes

$$h\partial_t\psi - h\partial_t[gh] - (hu)\partial_t u. \tag{3.3.1.27}$$

Using the definition of ψ, we have

$$\begin{aligned} h\partial_t\left[u^2/2 + gh + gZ\right] - h\partial_t[gh] - (hu)\partial_t u \\ &= \underbrace{h\partial_t\left[u^2/2\right]}_{=(hu)\partial_t u} + h\partial_t[gh] + \underbrace{h\partial_t[gZ]}_{=0} - h\partial_t[gh] - (hu)\partial_t u \\ &= (hu)\partial_t u + h\partial_t[gh] - h\partial_t[gh] - (hu)\partial_t u \\ &= 0. \end{aligned}$$

Thus the result is proven.

□

3.3.2 Remark on discontinuous solutions

In theorem 3.3.1, we only made reference to smooth solutions (h, u) in defining the stability and entropy relations of our extended shallow water system (3.2.4.18). For discontinuous solutions, it is not in general the case that strong solutions will always exist, and hence we must instead rely upon having a weak solution to system. The requirements and conditions under which such weak solutions exist is the focus of current ongoing research.

3.3.3 Corollary (condition for energy growth or decay)

(a) *The extended shallow water system (3.2.4.18) with infiltration rate $I < 0$ (i.e. water is recharging from the ground into the system) has energy decay if*

$$\alpha S + k_0\left(q/h\right) \geq \frac{S\left(q^2/2h^2 + \mathrm{g}\, h\right) - \mathrm{g}\, q\partial_x Z}{q^2/h^2} \tag{3.3.3.1}$$

that is, if the reduction in energy of the system from the friction effects is enough to compensate for the increase in energy from the source terms and the increase or decrease in energy from the topography, and energy growth otherwise.

(b) *The extended shallow water system (3.2.4.18) with infiltration rate $I > 0$ (i.e. water is infiltrating from the system into the ground) has energy decay if*

$$\alpha R + k_0\left(q/h\right) \geq \frac{S\left(q^2/2h^2 + \mathrm{g}\, h\right) - \mathrm{g}\, q\partial_x Z}{q^2/h^2} \tag{3.3.3.2}$$

that is, if the reduction in energy of the system from the friction effects is enough to compensate for the increase in energy (when the rate of precipitation exceeds that of the infiltration and so $S > 0$) and the increase or decrease in energy from the topography, and energy growth otherwise.

3.3.4 Comparison to the existing model

The derived model differs from the usual shallow water system for overland flows, (2.1.0.1), in which Sq/h and the additional friction terms in the conservation of momentum are neglected. In particular properties (a) and (c) in theorem 3.3.1 (hyperbolicity of the system and existence of a steady state) still hold, but the entropy relation is altered and the energy-consistency of the system becomes conditional not on the assumed level of friction but on the water height.

Using the same notations for E and ψ, one can prove that model (2.1.0.1) instead satisfies the following properties:

(b) For smooth solution (h, u), the mean velocity $u = q/h$ satisfies:

$$\partial_t u + \partial_x \psi(x, h, u) = \frac{-Su - k_0(u)u}{h}\,. \tag{3.3.4.1}$$

(d) System (2.1.0.1) satisfies the following entropy relation for smooth solutions:

$$\partial_t E + \partial_x \left[\left(E + \frac{\mathrm{g}\, h^2}{2} \right) u \right] = -S \left(\frac{u^2}{2} - \mathrm{g}\, h \right) - \mathrm{g}\, hu\partial_x Z - k_0(u)u^2\,. \tag{3.3.4.2}$$

Due to the altered entropy relation, the energy-consistency of model (2.1.0.1) is conditional on the water height, which we will ultimately see does not depend on the sign of the source term S. To begin with, however, let there be a net gain of water into the system, $S > 0$. Our entropy relation this implies that

$$-S \left(\frac{u^2}{2} - \mathrm{g}\, h \right) - \mathrm{g}\, hu\partial_x Z - k_0(u)u^2 \geqslant 0. \tag{3.3.4.3}$$

Dividing through by $-S$ (which we note will be negative), we have

$$\left(\frac{u^2}{2} - \mathrm{g}\, h \right) + \frac{\mathrm{g}\, hu\partial_x Z}{S} + \frac{k_0(u)u^2}{S} \leqslant 0. \tag{3.3.4.4}$$

Rearranging to isolate the water height h, we have

$$h \left(\frac{\mathrm{g}\, u\partial_x Z}{S} - \mathrm{g} \right) \leqslant -\frac{u^2}{2} - \frac{k_0(u)u^2}{S} \tag{3.3.4.5}$$

which simplifies to

$$h \leqslant \frac{\frac{u^2}{2} + \frac{k_0(u)u^2}{S}}{\mathrm{g}\left(1 - \frac{u\partial_x Z}{S}\right)} = \frac{u^2\left(S + 2k_0(u)\right)}{2\,\mathrm{g}\left(S - u\partial_x Z\right)}. \tag{3.3.4.6}$$

For $S < 0$, our entropy relation becomes

$$-S \left(\frac{u^2}{2} - \mathrm{g}\, h \right) - \mathrm{g}\, hu\partial_x Z - k_0(u)u^2 \leqslant 0. \tag{3.3.4.7}$$

Dividing through by $-S$ (which this time will be positive), we have

$$\left(\frac{u^2}{2} - \mathrm{g}\, h \right) + \frac{\mathrm{g}\, hu\partial_x Z}{S} + \frac{k_0(u)u^2}{S} \leqslant 0, \tag{3.3.4.8}$$

and so we derive the same condition as above for $S > 0$. Therefore, we can conclude that the entropy inequality for the existing model is only satisfied on the set

$$\left\{ h \leqslant \frac{u^2 \left(S + 2k_0(u)\right)}{2\,\mathrm{g}\left(S - u\partial_x Z\right)} \right\} \tag{3.3.4.9}$$

and hence the model is only conditionally well-posed. Therefore, as demonstrated in the mathematical derivation, the term Sq/h cannot be omitted.

3.4 Conclusion

Our aim in this chapter was to derive a mathematically rigorous one-dimensional shallow water model, extended to include both precipitation and infiltration effects. We achieved this by going back to the original two-dimensional Navier-Stokes equations and adapting the boundary conditions appropriately to model these additional meteorological phenomena.

The new model (3.2.4.18) that we have derived includes additional momentum source and friction terms in comparison to earlier models, which become special cases of our extended system. The friction terms are obtained naturally from the derivation and their presence is essential in explaining how the velocity of the water-body interacts with the additional water coming from either precipitation or runoff.

We showed in Theorem 3.3.1 and Corollary 3.3.3 that the existence of these additional terms leads to a model whose energetic consistency depends solely on the level of assumed rain-induced friction, denoted by α, and whenever these terms are neglected the model is instead conditionally consistent with respect to the water height; for certain regimes, this model may yield non-physical solutions. The presence of the rain-induced friction terms is particularly important from a flood modelling perspective, as these additional terms will cause a greater accumulation of the flow and thus lead to longer lasting and more pronounced flooding.

As we noted in §2.1, the techniques and approach that we have used to adapt the one-dimensional shallow water model to include precipitation and infiltration effects can be readily extended to the two-dimensional system, starting from both the three-dimensional Navier-Stokes and three-dimensional Euler equations. The inclusion of the rain- and infiltration-induced friction terms in the two-dimensional system will require careful treatment, however, since there may be new issues that arise due to the additional dimension.

Chapter 4

Developing a well-balanced kinetic scheme

Now we have developed our extended shallow water system, the next step is to design a suitable numerical method. As we detailed in §2.3, our approach will be to consider a kinetic interpretation of our extended shallow water system from which we will derive a kinetic equation. This equation can then be used to derive a well-balanced numerical scheme akin to those detailed in §2.2.

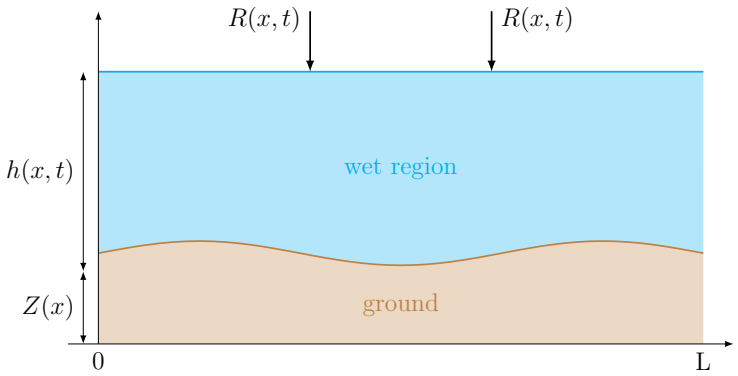

Figure 4.1: In considering a balance law system, we must adapt the *lake-at-rest* property used for conservation laws to account for the expected addition of water.

For our extended shallow water system, we do first have to make a small adjustment to the framework for our kinetic formulation. Since through the addition of the rainfall and infiltration effects our shallow water system is no longer a conservation law but rather a balance law, we have the possibility of water being added to or lost from the lake, and thus this particular equilibrium only holds in the case $S = 0$ (which is not very useful for the applications we want to consider). We must adapt this property, therefore, and instead desire that our system preserves the *filling the lake* state (see Figure 4.1), given by:

$$\partial_t h = R \text{ and } u = 0; \tag{4.0.0.1}$$

that is, the rate at which the height of water changes is equal to the rate at which water is added to the system through the rainfall term. Failing to preserve this

would mean a change in the mass of water greater or lower than the rate at which it is added, thus violating the balance of mass property of our system. As for the lake-at-rest, the *kinetic solvers* can be modified to preserve the filling-the-lake state, while at the same time maintaining their simplicity and stability properties.

In this chapter we demonstrate the construction of a new numerical method for modelling the shallow water system, extended to include rainfall and infiltration effects. In §4.1, we present an overview of the kinetic formulation that underpins our numerical method, which is then used to extend the standard kinetic equation to include the new terms in the momentum equation in §4.2. Finally, in §4.3, we present several numerical experiments to demonstrate the application of the model we have developed.

4.1 Kinetic formulation

To derive the kinetic equation for our extended shallow water system, we follow the kinetic formulation proposed by Audusse et al. [2000], Perthame and Simeoni [2001] and further developed by Bourdarias et al. [2014], Ersoy [2015]. We consider a *kinetic averaging weight function* $\chi : \mathbb{R} \to \mathbb{R}$ and a *kinetic density function* M satisfying

$$\chi(\omega) = \chi(-\omega) \geq 0, \quad \int_{\mathbb{R}} \chi(\omega) d\omega = 1, \quad \int_{\mathbb{R}} \omega^2 \chi(\omega) d\omega = \frac{\mathrm{g}}{2}, \tag{4.1.0.1}$$

$$M(x,t,\xi) := \sqrt{h(x,t)}\chi\left(\frac{\xi - u(x,t)}{\sqrt{h(x,t)}}\right). \tag{4.1.0.2}$$

These functions originate in the kinetic theory where $M(x,t,\xi)$ accounts for the density of particles with speed ξ at the space-time point (x,t).

The discretisation we will use in our numerical scheme will be based upon the specific weighting function

$$\chi(\omega) = \frac{1}{\pi\,\mathrm{g}}\left[2\,\mathrm{g} - \omega^2\right]_+^{1/2} \text{ for } \omega \in \mathbb{R}, \tag{4.1.0.3}$$

where $[X]_+$ stands for the positive part of X [Perthame and Simeoni, 2001, eq.(2.13)]. We show this function has the required properties we desire.

Proof. The non-negativity of $\chi(\omega)$ is directly implied by the definition, as we consider only the positive component the square root. We also note that, since $\omega^2 = (-\omega)^2$, it can easily be seen that $\chi(\omega) = \chi(-\omega)$.

For the first integral, the square root is non-negative for $\omega \in [-\sqrt{2\,\mathrm{g}}, \sqrt{2\,\mathrm{g}}]$ and so the integral can be simplified to

$$\frac{1}{\pi\,\mathrm{g}} \int_{-\sqrt{2\,\mathrm{g}}}^{\sqrt{2\,\mathrm{g}}} \left[2\,\mathrm{g} - \omega^2\right]^{1/2}. \tag{4.1.0.4}$$

To calculate this integral, we first make the substitution $\omega = \sqrt{2\,\mathrm{g}}\sin(x)$; this leads to

$$\begin{aligned} \omega &= \sqrt{2\,\mathrm{g}}, \quad x = \pi/2 \\ \omega &= -\sqrt{2\,\mathrm{g}}, \quad x = -\pi/2 \\ d\omega &= \sqrt{2\,\mathrm{g}}\cos(x)dx \end{aligned} \tag{4.1.0.5}$$

and thus

$$\begin{aligned} &\frac{1}{\pi\,\mathrm{g}}\int_{-\pi/2}^{\pi/2}\sqrt{2\,\mathrm{g}}\cos(x)\sqrt{2\,\mathrm{g}-2\,\mathrm{g}\sin^2(x)}dx \\ &= \frac{2}{\pi}\int_{-\pi/2}^{\pi/2}\cos(x)\sqrt{1-\sin^2(x)}dx. \end{aligned} \tag{4.1.0.6}$$

Using the identities $1-\sin^2(x) = \cos^2(x)$ and $\cos^2(x) = \frac{1+\cos(2x)}{2}$, we have

$$\begin{aligned} \frac{2}{\pi}\int_{-\pi/2}^{\pi/2}\cos(x)\sqrt{1-\sin^2(x)}dx &= \frac{2}{\pi}\int_{-\pi/2}^{\pi/2}\frac{1+\cos(2x)}{2}dx \\ &= \frac{1}{\pi}\left[x+\frac{\sin(2x)}{2}\right]_{-\pi/2}^{\pi/2} \\ &= \frac{1}{\pi}\left[\frac{\pi}{2}+0-\left(-\frac{\pi}{2}+0\right)\right] \\ &= 1. \end{aligned} \tag{4.1.0.7}$$

Similarly, for the second integral we have

$$\begin{aligned} &\frac{1}{\pi\,\mathrm{g}}\int_{-\pi/2}^{\pi/2}2\,\mathrm{g}\sin^2(x)\sqrt{2\,\mathrm{g}}\cos(x)\sqrt{2\,\mathrm{g}-2\,\mathrm{g}\sin^2(x)}dx \\ &= \frac{4\,\mathrm{g}}{\pi}\int_{-\pi/2}^{\pi/2}\sin^2(x)\cos(x)\sqrt{1-\sin^2(x)}dx \\ &= \frac{4\,\mathrm{g}}{\pi}\int_{-\pi/2}^{\pi/2}\sin^2(x)\cos^2(x)dx. \end{aligned} \tag{4.1.0.8}$$

Using this time the identity $\sin^2(x)\cos^2(x) = \frac{1-\cos(4x)}{8}$, we have

$$\begin{aligned} \frac{4\,\mathrm{g}}{\pi}\int_{-\pi/2}^{\pi/2}\frac{1-\cos(4x)}{8}dx &= \frac{\mathrm{g}}{2\pi}\left[x-\frac{\sin(4x)}{4}\right]_{-\pi/2}^{\pi/2} \\ &= \frac{\mathrm{g}}{2\pi}\left[\frac{\pi}{2}-0-\left(-\frac{\pi}{2}-0\right)\right] \\ &= \frac{\mathrm{g}}{2}. \end{aligned} \tag{4.1.0.9}$$

Thus the proof is concluded. □

In developing a numerical method, the goal is for the derivation of the finite-volume scheme fluxes to be based on M, through the following property which links the macroscopic variables with the microscopic ones.

4.1.1 Proposition (macroscopic-microscopic relations)

Let the functions h, u solve the shallow water system (3.2.4.18) and kinetic density M as in (4.1.0.2). If $h(x,t) > 0$ at (x,t) then the following macroscopic-microscopic relations *hold*

$$\int_{\mathbb{R}} \begin{bmatrix} 1 \\ \xi \\ \xi^2 \end{bmatrix} M(x,t,\xi)d\xi = \begin{bmatrix} h(x,t) \\ h(x,t)u(x,t) \\ h(x,t)u(x,t)^2 + \mathrm{g}\, h(x,t)^2/2 \end{bmatrix}. \tag{4.1.1.1}$$

Proof. We prove each of the three integrals in turn.

(1) From the definition of the kinetic density M, (4.1.0.2), the integral becomes

$$\int_{\mathbb{R}} M(x,t,\xi)d\xi = \sqrt{h(x,t)} \int_{\mathbb{R}} \chi\left(\frac{\xi - u(x,t)}{\sqrt{h(x,t)}}\right) d\xi. \tag{4.1.1.2}$$

Applying a change of variables $\eta := \frac{\xi - u}{\sqrt{h}}$, from which we have $d\xi = \sqrt{h}d\eta$, (4.1.1.2) becomes

$$\sqrt{h(x,t)} \int_{\mathbb{R}} \sqrt{h(x,t)}\chi(\eta)d\eta = h(x,t) \int_{\mathbb{R}} \chi(\eta)d\eta. \tag{4.1.1.3}$$

From (4.1.0.1), the integral

$$\int_{\mathbb{R}} \chi(\eta)d\eta = 1 \tag{4.1.1.4}$$

and thus we have

$$\int_{\mathbb{R}} M(x,t,\xi)d\xi = h(x,t) \tag{4.1.1.5}$$

as claimed.

(2) For the second integral, we apply the same change of variables, which yields

$$\begin{aligned} \int_{\mathbb{R}} \xi M(x,t,\xi)d\xi &= \sqrt{h(x,t)} \int_{\mathbb{R}} \xi\chi\left(\frac{\xi - u(x,t)}{\sqrt{h(x,t)}}\right) d\xi \\ &= \sqrt{h(x,t)} \int_{\mathbb{R}} \sqrt{h(x,t)} \cdot (\eta\sqrt{h} + u)\chi(\eta)d\eta \\ &= h(x,t) \int_{\mathbb{R}} (\eta\sqrt{h} + u)\chi(\eta)d\eta. \end{aligned} \tag{4.1.1.6}$$

Multiplying out the brackets within the integral, we get

$$\begin{aligned} &h(x,t)\sqrt{h(x,t)} \int_{\mathbb{R}} \eta\chi(\eta)d\eta + h(x,t)u(x,t) \underbrace{\int_{\mathbb{R}} \chi(\eta)d\eta}_{=1} \\ &= h(x,t)\sqrt{h(x,t)} \int_{\mathbb{R}} \eta\chi(\eta)d\eta + h(x,t)u(x,t). \end{aligned} \tag{4.1.1.7}$$

To prove the claim of the proposition, we need to show that the remaining term equals 0. From the properties (4.1.0.1), we note that χ is an even function (i.e. $\chi(\eta) = \chi(-\eta)$), and thus $\eta\chi(\eta)$ is an odd function. Since the integral of an odd function over $\mathbb{R}$ is by definition 0,

$$\int_{\mathbb{R}} \eta\chi(\eta)d\eta = 0 \tag{4.1.1.8}$$

and hence

$$\int_{\mathbb{R}} \xi M(x,t,\xi)d\xi = h(x,t)u(x,t) \tag{4.1.1.9}$$

as claimed.

(3) For the third and final integral, we proceed in a similar manner as above:

$$\begin{aligned}
\int_{\mathbb{R}} \xi^2 M(x,t,\xi)d\xi &= \sqrt{h(x,t)} \int_{\mathbb{R}} \xi^2 \chi\left(\frac{\xi - u(x,t)}{\sqrt{h(x,t)}}\right) d\xi \\
&= \sqrt{h(x,t)} \int_{\mathbb{R}} \sqrt{h(x,t)} \cdot (\eta\sqrt{h} + u)^2 \chi(\eta)d\eta \\
&= h(x,t) \int_{\mathbb{R}} (u^2 + 2\eta\sqrt{h}u + \eta^2 h)\chi(\eta)d\eta \\
&= hu^2 \underbrace{\int_{\mathbb{R}} \chi(\eta)d\eta}_{=1} + 2h\sqrt{h}u \underbrace{\int_{\mathbb{R}} \eta\chi(\eta)d\eta}_{=0} + h^2 \underbrace{\int_{\mathbb{R}} \xi^2\chi(\eta)d\eta}_{=\frac{\mathrm{g}}{2}} \\
&= hu^2 + \frac{\mathrm{g}\, h^2}{2}
\end{aligned}$$

making use of (4.1.0.1) and (4.1.1.8) in the last simplification.

Thus the proof of proposition 4.1.1 is complete. □

4.2 Kinetic equation

Recall the extended shallow water model (3.2.4.18) that we developed in Chapter 3 to incorporate precipitation and infiltration phenomena:

$$\begin{aligned}
\partial_t h + \partial_x q &= S \\
\partial_t q + \partial_x \left[\frac{q^2}{h} + \mathrm{g}\,\frac{h^2}{2}\right] &= -\,\mathrm{g}\, h\partial_x Z + S\frac{q}{h} - \left(k_R - k_I + k_0\left(\frac{q}{h}\right)\right)\frac{q}{h} \\
&\text{where } q = hu\,.
\end{aligned} \tag{4.2.0.1}$$

We will demonstrate in this section how we can solve this equation (that is, find (h,u) for a given topography, source term, and friction coefficients) using a kinetic approach.

For the topography and friction terms in the conservation of momentum equation, substituting for $u = q/h$, we note that these terms can be rewritten as

$$-\,\mathrm{g}\, h\partial_x Z - (k_R - k_I + k_0(u))\, u = -\,\mathrm{g}\, h\left(\partial_x Z + \frac{(k_R - k_I + k_0(u))\, u}{\mathrm{g}\, h}\right) \tag{4.2.0.2}$$

following the approach considered in [Bourdarias et al., 2011], for example, adapted to account for our additional friction terms. The reason for rewriting these terms in this manner is so we can pack them into a single term; that is, we define

$$W(x,t) := Z(x) + \int_0^x \left[\frac{(k_R - k_I + k_0(u))\,u}{\mathrm{g}\,h}\right](s,t)ds \text{ for } 0 < x < L, \tag{4.2.0.3}$$

and thus the system becomes

$$\begin{aligned} \partial_t h + \partial_x[hu] &= S\ , \\ \partial_t[hu] + \partial_x\left[hu^2 + \frac{\mathrm{g}\,h^2}{2}\right] &= -\,\mathrm{g}\,h\partial_x W + Su\ . \end{aligned} \tag{4.2.0.4}$$

The kinetic approach allows us to simplify this system into a single equation; more specifically, we set M as the solution of the following *kinetic equation*

$$\begin{aligned} &\partial_t M(x,t,\xi) + \xi\partial_x M(x,t,\xi) \\ &\qquad - \mathrm{g}\,\partial_x\hat{W}\partial_\xi M(x,t,\xi) + \frac{S(x,t)M(x,t,\xi)}{\langle M\rangle_1} = Q(x,t,\xi) \end{aligned} \tag{4.2.0.5}$$

where

$$\hat{W}(x,t) := Z(x) + \int_0^x \left[\frac{(k_R - k_I + k_0(\langle M\rangle_2))\,\langle M\rangle_2}{\mathrm{g}\,\langle M\rangle_1}\right](s,t)ds \tag{4.2.0.6}$$

using the notation

$$\langle M\rangle_1 = \int_{\mathbb{R}} M d\xi, \quad \langle M\rangle_2 = \frac{1}{\langle M\rangle_1}\int_{\mathbb{R}} \xi M d\xi. \tag{4.2.0.7}$$

The term $Q(x,t,\xi)$ plays the mathematical role of a *collision term*, similar, for instance, to the ones encountered in Boltzmann's equation, and must satisfy

$$\int_{\mathbb{R}} \begin{bmatrix}1\\ \xi\end{bmatrix} Q(x,t,\xi)d\xi = \begin{bmatrix}0\\0\end{bmatrix}. \tag{4.2.0.8}$$

We take a second here to note why the additional notation for $\langle M\rangle_1$ and $\langle M\rangle_2$ is required. In defining $\hat{W}(x,t)$, the kinetic form of $W(x,t)$, we assume that (h,u) are unknown and to be found, and thus we cannot use them within the definition. We are required, therefore, to instead define $\hat{W}$ in terms of $\langle M\rangle_1$ and $\langle M\rangle_2$, which are themselves defined in terms of the density function M, the solution to the kinetic equation, and which by virtue of proposition 4.1.1 will ultimately give us h and u.

4.2.1 Observations

Before continuing with the derivation of our kinetic scheme, we make two interesting observations on what we have developed thus far:

(1) In contrast to previous work, e.g. Perthame and Simeoni [2001], the kinetic equation (4.2.0.5) contains an extra term accounting for precipitation and infiltration effects, and this departure is crucial for the derivation of the fluxes that lead to a well-balanced scheme in the presence of such terms. We also note that, even though the Maxwellian function M is constructed for still water steady states, where $S(x,t) = 0$, we can still use it here to ensure a well-balanced scheme.

(2) In general, it is easier to find a numerical scheme to solve equation (4.2.0.5) for M that has the properties we desire than to solve the full shallow water system for h and u. However, in finding M, we can calculate h and hu by virtue of the macro-microscopic relations (proposition 4.1.1). In fact, M is never calculated explicitly, rather the function

$$\hat{M}(h,\eta) := \sqrt{h}\chi\left(\frac{\eta}{\sqrt{h}}\right) \text{ with } M(x,t,\xi) = \hat{M}(h(x,t),\xi - u(x,t)), \quad (4.2.1.1)$$

is used to build the fluxes appearing in a finite volume method.

4.2.2 Discretisation and kinetic fluxes

To go from the kinetic equation (4.2.0.5) to a numerical method, we follow the approach of Perthame and Simeoni [2001], in which they developed a kinetic scheme for the standard shallow water system, i.e. equation (4.2.0.5) with $S = 0$. Their approach was based on the general method for developing a finite volume scheme, integrating the kinetic equation over the domain of interest, with the vector of unknowns defined as

$$U_i^n = \int_{\mathbb{R}} \begin{bmatrix} 1 \\ \xi \end{bmatrix} M_i^n(\xi) d\xi = \begin{bmatrix} h_i^n \\ h_i^n u_i^n \end{bmatrix} \quad (4.2.2.1)$$

where the final equality can be seen from the macroscopic-microscopic relations (4.1.1.1) and in view of the second observation above. We follow the same process for our shallow water system, giving us the numerical scheme

$$U_i^{n+1} = U_i^n - \frac{\Delta t}{\Delta x}\left(F_{i+1/2}^n - F_{i-1/2}^n\right) + \Delta t \begin{bmatrix} S_i^n \\ S_i^n u_i^n \end{bmatrix} \quad (4.2.2.2)$$

where S_i^n is a discretisation of the combined rain and infiltration terms (and which we will explore in more detail in the next chapter). For the time-step, Δt, we use the following condition:

$$\Delta t = \text{CFL} \cdot \frac{\Delta x}{\max\left(|u_i^n| + \sqrt{2\,\mathrm{g}\,h_i^n}\right)} \quad (4.2.2.3)$$

where $\text{CFL} \in (0,1]$ [Perthame and Simeoni, 2001, e.g.].

The construction of the numerical fluxes $F_{i\pm1/2}^n$ in (4.2.2.2) is based on the Nemitskii-type operator associated with $\hat{M}$ given in (4.2.1.1). We give here a brief overview of how the successive numerical flux terms are developed; the interested reader is directed to Perthame and Simeoni [2001] and Bourdarias et al. [2014] for more details.

We define the numerical flux (which has two components representing the conservation of mass and momentum equations), as the integral

$$F^n_{i\pm\frac{1}{2}} := \int_{\mathbb{R}} \xi \begin{bmatrix} 1 \\ \xi \end{bmatrix} M^{\mp}_{i\pm1/2}(\xi) d\xi. \tag{4.2.2.4}$$

The intermediate quantities $M^{\mp}_{i\pm1/2}(\xi)$, which measure the flux at the upper and lower boundaries of the cell $c_i = [x_{i-1/2}, x_{i+1/2}]$, respectively, are realised as upwinded fluxes:

$$\begin{aligned} M^{-}_{i+1/2} &:= M^n_i(\xi)\mathbb{I}[\xi > 0] + M^n_{i+1/2}(\xi)\mathbb{I}[\xi < 0]\,, \\ M^{+}_{i-1/2} &:= M^n_i(\xi)\mathbb{I}[\xi < 0] + M^n_{i-1/2}(\xi)\mathbb{I}[\xi > 0]\,, \end{aligned} \tag{4.2.2.5}$$

with

$$\begin{aligned} M^n_{i\pm1/2} := M^n_i(-\xi)\mathbb{I}\left[|\xi|^2 \le 2\,\mathrm{g}\,\Delta W^n_{i\pm1/2}\right] \\ + M^n_{i\pm1}\left(\mp\sqrt{|\xi|^2 - 2\,\mathrm{g}\,\Delta W^n_{i\pm1/2}}\right)\mathbb{I}\left[|\xi|^2 \ge 2\,\mathrm{g}\,\Delta W^n_{i\pm1/2}\right] \end{aligned} \tag{4.2.2.6}$$

where we use the notation

$$\mathbb{I}[P] := \begin{cases} 1 & \text{if P is true,} \\ 0 & \text{if P is false.} \end{cases} \tag{4.2.2.7}$$

To understand how these fluxes are defined, consider the flux over the upper bound $M^{-}_{i+1/2}$. From (4.2.2.5), we can see that it is comprised of two terms:

(1) $M^n_i(\xi)\mathbb{I}[\xi > 0]$: movement of water with positive velocity ($\xi > 0$) from within cell c_i to cell c_{i+1}

(2) $M^n_{i+1/2}(\xi)\mathbb{I}[\xi < 0]$: movement of water with negative velocity ($\xi < 0$) from within cell c_{i+1} to cell c_i. This term is decomposed a second time into components reflecting whether the water has enough energy to overcome the topography and friction to enter or leave the cell.

The term $\Delta W^n_{i\pm1/2}$ is the upwinded source term and provides the jump condition necessary for a particle in one cell to overcome the friction and topography to move to an adjacent cell. Consistent with previous definitions, we calculate this term numerically as:

$$\Delta W^n_{i+1/2} = W_{i+1}(t_n) - W_i(t_n), \quad \Delta W^n_{i-1/2} = W_{i-1}(t_n) - W_i(t_n) \tag{4.2.2.8}$$

where

$$W_i(t) = \mathbb{I}[c_i]\,(x)\frac{1}{\Delta x}\int_{c_i} W(x,t)dx \tag{4.2.2.9}$$

for a given cell c_i. The semi-discretised kinetic density, M^n_i, is defined as

$$M^n_i(\xi) := \sqrt{h^n_i}\,\chi\left(\frac{\xi - u^n_i}{\sqrt{h^n_i}}\right). \tag{4.2.2.10}$$

We provide details of each step in deriving our kinetic scheme in Algorithm 4.1.

Algorithm 4.1 Kinetic scheme algorithm

procedure KINETICSCHEME
    consider the extended shallow water system (4.2.0.1)
    pack the topography and friction into a single term W given by (4.2.0.3)
    write the new shallow water system (4.2.0.4) in terms of (h, u, S, W)

    simplify (4.2.0.4) into a single kinetic equation (4.2.0.5) in terms of M
    define U_i^n as the vector of unknowns given by (4.2.2.1)
    integrate (4.2.0.5) to derive the numerical scheme (4.2.2.2)

    define the fluxes in the numerical scheme as the integral (4.2.2.4)
    quantities $M^{\mp}_{i\pm1/2}$ are defined in (4.2.2.5) and (4.2.2.6) in terms of ξ and ΔW
    the upwinded source term ΔW is given by the difference (4.2.2.8)
end procedure

4.3 Numerical tests

The kinetic scheme we use for our numerical method was implemented by extending the code of Besson and Lakkis [2013] to account for the additional source term in (4.2.2.2), and we present here several simple numerical tests to demonstrate the validity and application of our shallow water system and the associated numerical method. Since the infiltration and precipitation term have almost the same mathematical and numerical difficulties, we will consider only the rain term and thus take $I \equiv 0$. Numerical tests with a realistic infiltration term will be considered in future work.

In §4.3.1, we begin by examining the influence of the friction effect α on the solution in an idealised scenario where an exact solution can be calculated, with a focus on determining in what regimes of α the solution is physically realistic. In §4.3.2, we compare our numerical model to a flume experiment, considering how our results compare to both the physical data collected from this experiment and also previous numerical simulations of this experiment using other methods. Finally, in §4.3.3, we simulate multiple rainfall processes of increasing duration on a slope with both a constant and decreasing gradient, and again measure how the value of α impacts the solution.

4.3.1 Influence of the friction effect α in an idealised scenario

We start by studying the influence of the rain-induced friction effect $k_R = \alpha R$, which is included in Equations (3.2.4.18) and omitted in Equations (2.1.0.1). As we saw in Corollary 3.3.3, for $S > 0$ (i.e. a net gain of water into the system), the energy growth/decay of the system depends upon the value of α as follows (substituting

$q = hu$ into our condition):

$$\partial_t E + \partial_x \left[\left(E + \frac{\mathrm{g}\, h^2}{2} \right) u \right] \begin{cases} \leqslant 0 & \text{if } \alpha \geqslant \frac{R\left(\frac{u^2}{2} + \mathrm{g}\, h\right) - \mathrm{g}\, huZ - k_0(u)u^2}{Ru^2} \\ \\ \geqslant 0 & \text{if } \alpha \leqslant \frac{R\left(\frac{u^2}{2} + \mathrm{g}\, h\right) - \mathrm{g}\, huZ - k_0(u)u^2}{Ru^2} \end{cases} \tag{4.3.1.1}$$

i.e. we see energy decay if the friction effect from α and k_0 is large enough to balance the source and topography terms, and energy growth otherwise. Similarly, the presence of the term k_R in the conservation of momentum equation indicates a dependence on α for the change in momentum and velocity. From a flood modelling perspective, the momentum and energy of a flood will be directly related to the amount of damage it could potentially cause; our aim, therefore, is to consider exactly how these variables behave over time as we change the value of α.

To do this, we will simplify the conditions for our test to a hypothetical, idealised scenario that will enable us to calculate an *exact solution* for our extended shallow water system that we can compare our simulation with. We consider a constant rainfall process on a river spanning spatial domain $x \in [0, 10]$ and time domain $t \in [0, 1]$, with topography $Z(x) = 0.1$, $N = 100$ meshpoints, and a CFL number of 0.95. We prescribe periodic boundary conditions and assume a constant initial height and discharge of

$$h(x, 0) = q(x, 0) = 1.0 \quad \forall x \in [0, 10]. \tag{4.3.1.2}$$

The rainfall intensity is applied uniformly on the river as a function of time up the final time $T = 1$:

$$R(t) = 1.0 \quad \forall t \in [0, 1]. \tag{4.3.1.3}$$

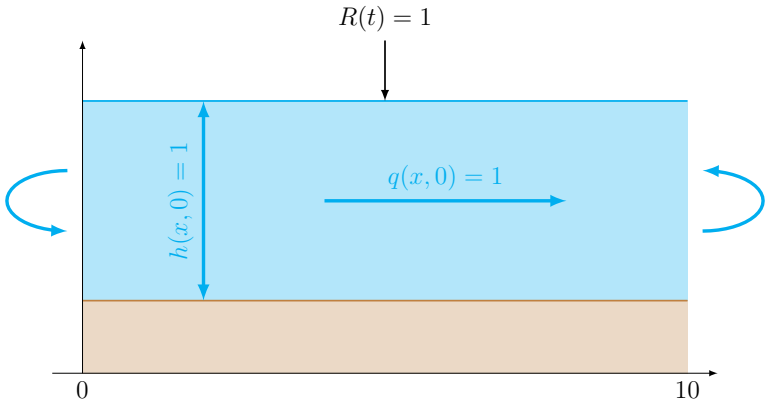

Figure 4.2: Diagram of the idealised scenario we are considering for our first numerical test.

Using these parameter values and assuming that the spatial derivative in both the mass and momentum equation can be neglected, our extended shallow water system simplifies to:

$$\begin{aligned} \partial_t h &= 1 \\ \partial_t q &= (1 - \alpha)\, \frac{q}{h} \quad \text{where } q = hu. \end{aligned} \tag{4.3.1.4}$$

We can solve explicitly for h, q, and u (which we note now only depend on t) as follows:

$$\begin{aligned} h(t) &= t+1 \\ q(t) &= (t+1)^{1-\alpha} \\ u(t) &= \frac{q(t)}{h(t)} = \frac{(t+1)^{1-\alpha}}{t+1} = (t+1)^{-\alpha}. \end{aligned} \tag{4.3.1.5}$$

For the entropy relation (3.3.1.4), which simplifies under these conditions to

$$\partial_t E = \left(\frac{1}{2} - \alpha\right) u^2 + \mathrm{g}\, h \quad \text{where } E = \frac{hu^2}{2} + \frac{\mathrm{g}\, h^2}{2}, \tag{4.3.1.6}$$

we note that the energy is comprised of both the kinetic energy, $K_E = {}^{hu^2}/_2$, and the potential energy, $P_E = {}^{\mathrm{g}\,h^2}/_2$. In our case, we are only interested in the change in kinetic energy, and thus our entropy relation becomes

$$\partial_t K_E = \left(\frac{1}{2} - \alpha\right)(t+1)^{-2\alpha} \begin{cases} \geqslant 0 & \text{if } \alpha \leqslant \frac{1}{2} \\ < 0 & \text{if } \alpha > \frac{1}{2} \end{cases}. \tag{4.3.1.7}$$

Using these equations, we can plot how the momentum, velocity, and change in kinetic energy fluctuate over time depending on the friction level α, giving us a total of seven separate regimes. We also measure these values in our simulations at the midpoint of the domain ($x = 5$) to enable us to compare the accuracy of our numerical scheme (in an admittedly idealised scenario) to the exact solution.

(i) $\boldsymbol{\alpha < 0}$: the friction effect from the rain hitting the river acts with the flow, resulting in an increase in momentum, velocity, and change in kinetic energy. Such a regime is unrealistic, as additional momentum is being created even though the rain is assumed to fall with zero momentum.

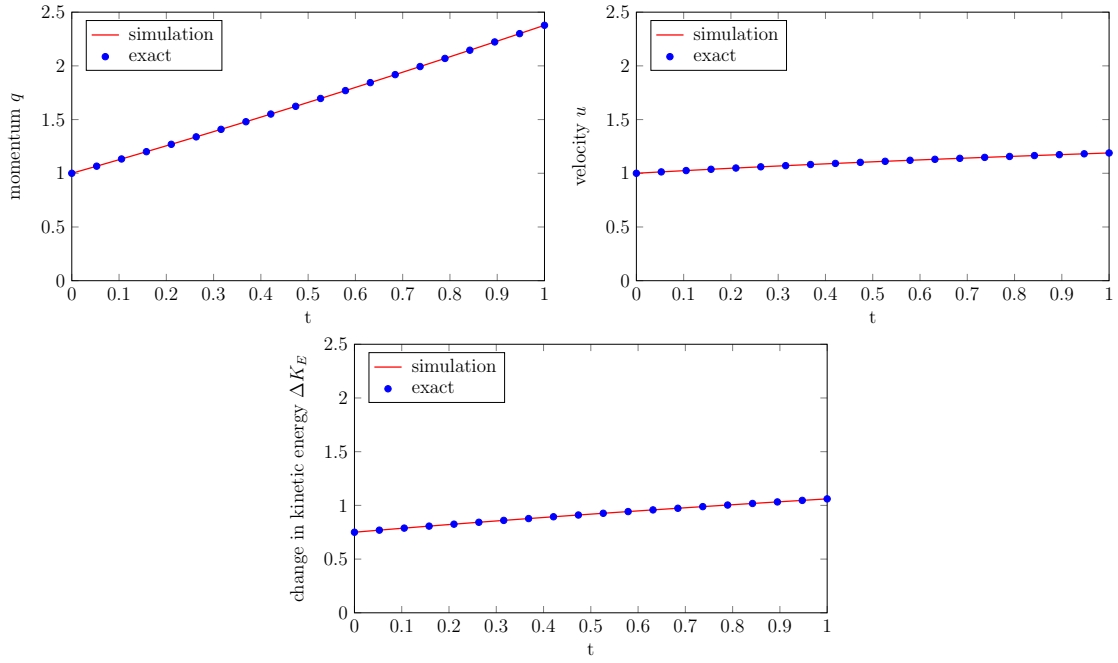

(ii) $\alpha = 0$: rain falling on the river does not produce any friction to slow the flow down, and thus the velocity remains the same while the momentum increases at the rate of the increase in water height. The change in kinetic energy is positive but remains steady. Since momentum is still being produced, this regime is also unrealistic.

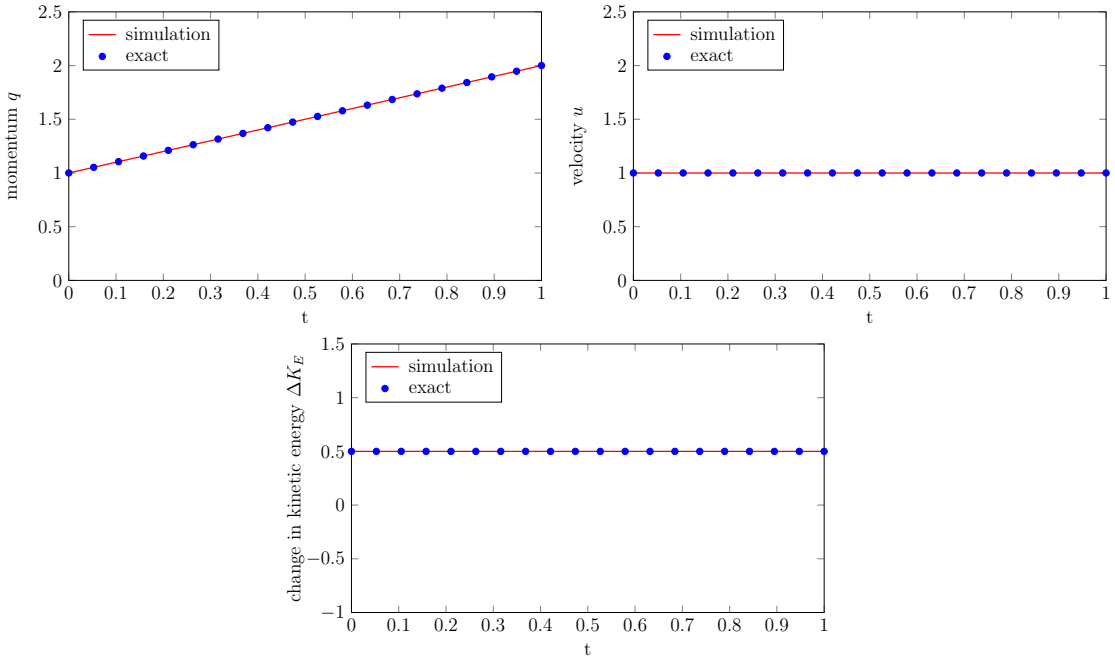

(iii) $0 < \alpha < \frac{1}{2}$: friction is produced when the rain hits the river flow, but not enough is produced to counter the increase in momentum. Both the velocity and change in kinetic energy decrease over time, though the energy change still remains positive. Though the velocity is decreasing, the rate is not enough to reduce the momentum, and so the regime is also unrealistic.

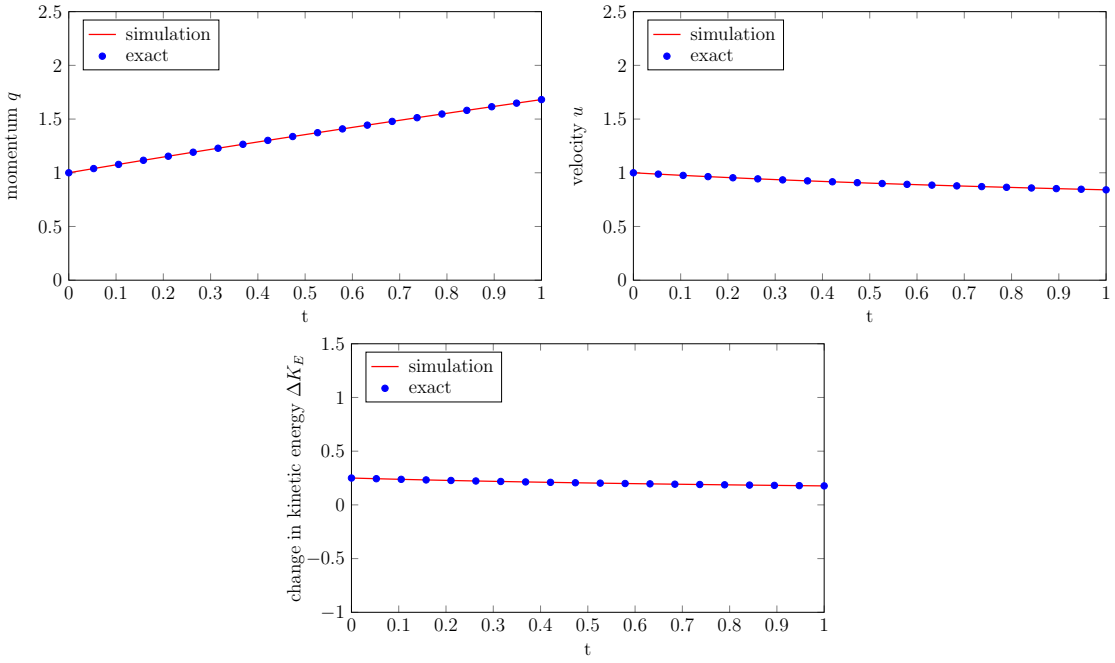

(iv) $\alpha = \frac{1}{2}$: similar to the previous case, the momentum increases and the velocity decrease over time, though the rate at which this occurs is reduced for the momentum and increased for the velocity. Unlike previous cases, however, the change in kinetic energy is zero, which remains steady over time. This regime is, like the previous cases, unrealistic from a physical perspective.

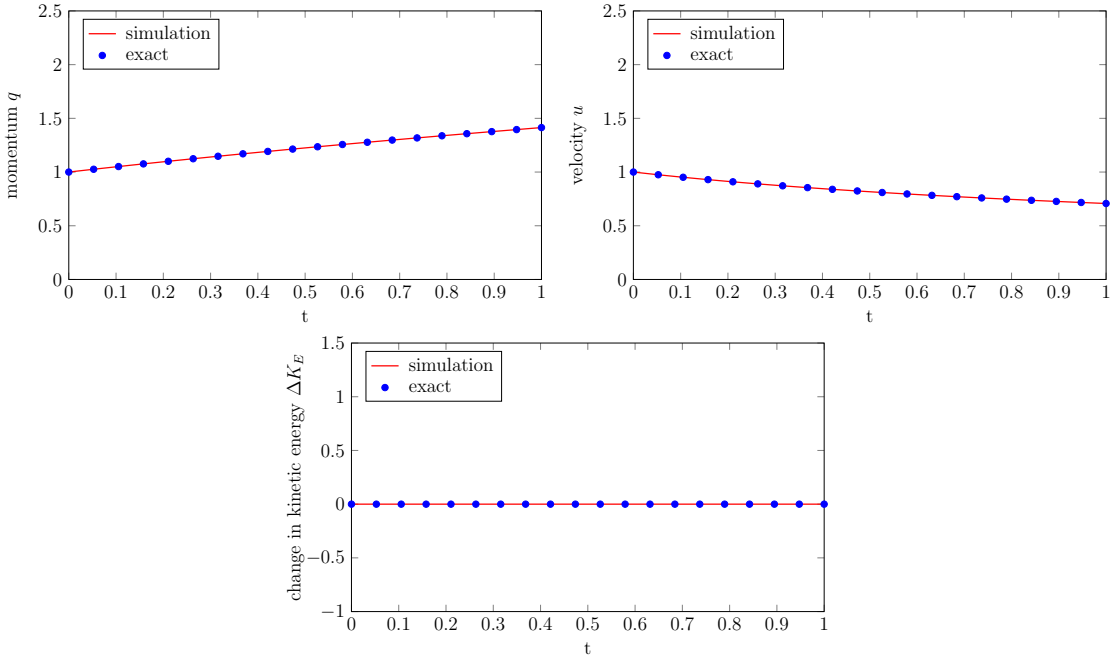

(v) $\frac{1}{2} < \alpha < 1$: once again, the momentum increases and the velocity decreases, but the increase in friction causes the rate at which this occurs to reduce and increase, respectively. The change in kinetic energy is now negative, but tends to zero over time. This regime is again unrealistic.

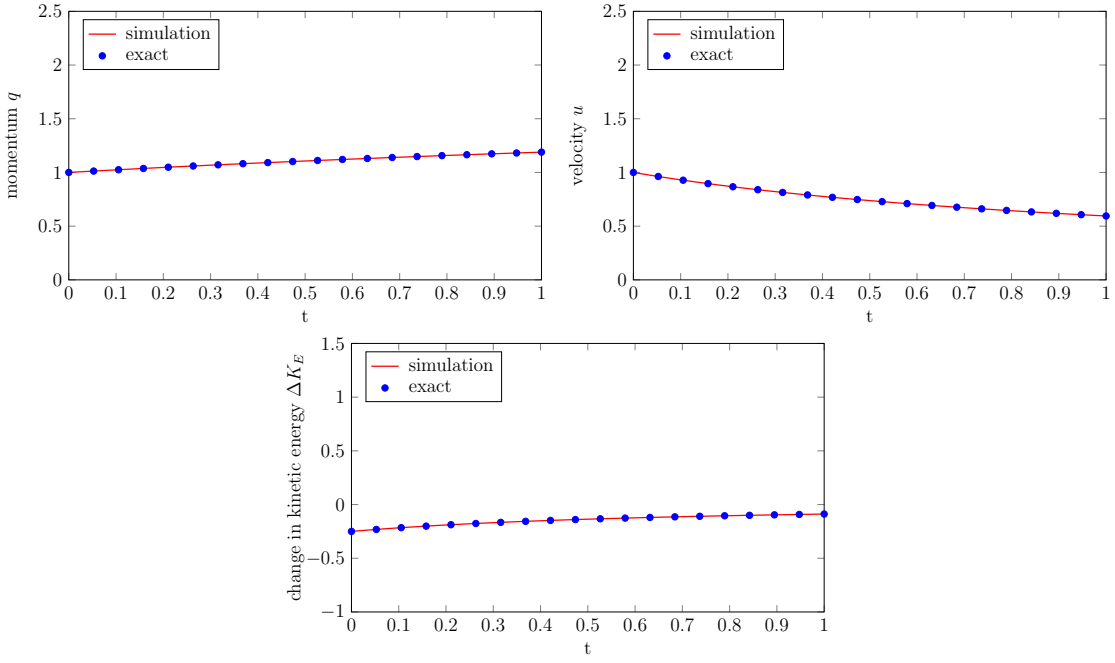

(vi) $\alpha = 1$: the friction generated by the rain causes a large enough reduction in velocity to balance the increase in height, and so momentum is conserved. The change in kinetic energy is again negative and tends to zero. Since momentum is conserved, this regime is realistic from a physical perspective.

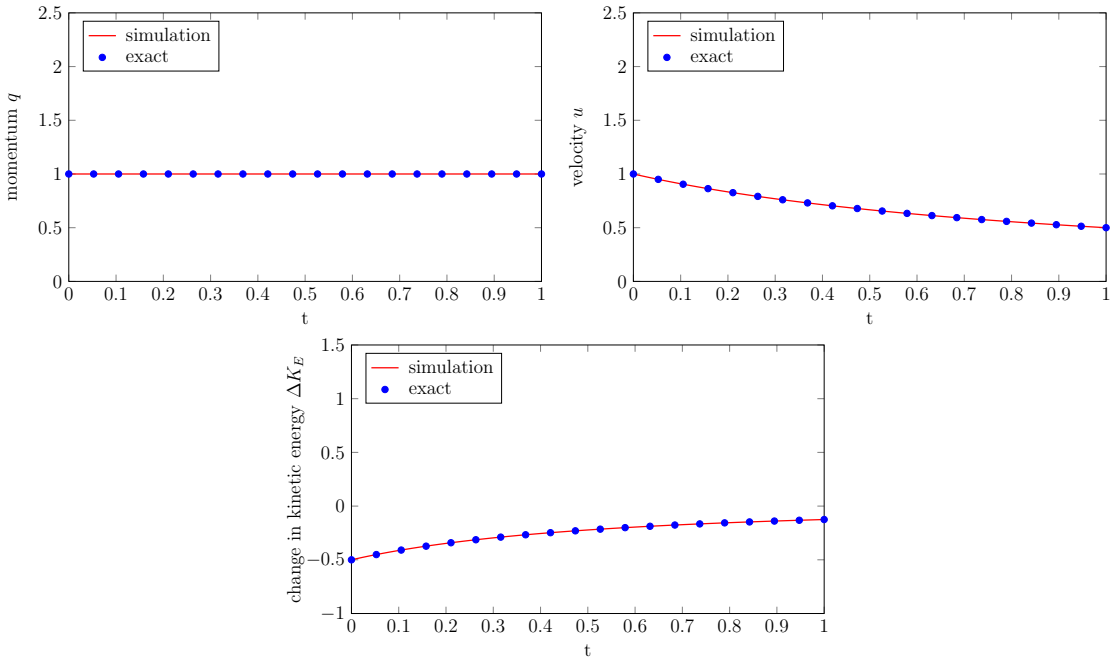

(vii) $\alpha > 1$: the friction generated by the rain slows the flow at faster rate than the increase in water height; momentum and velocity both decrease over time, and the change in kinetic energy is again negative and tending to zero. The reduction in momentum due to the higher friction effect is physically realistic, though whether taking $\alpha > 1$ is physically relevant remains an open question.

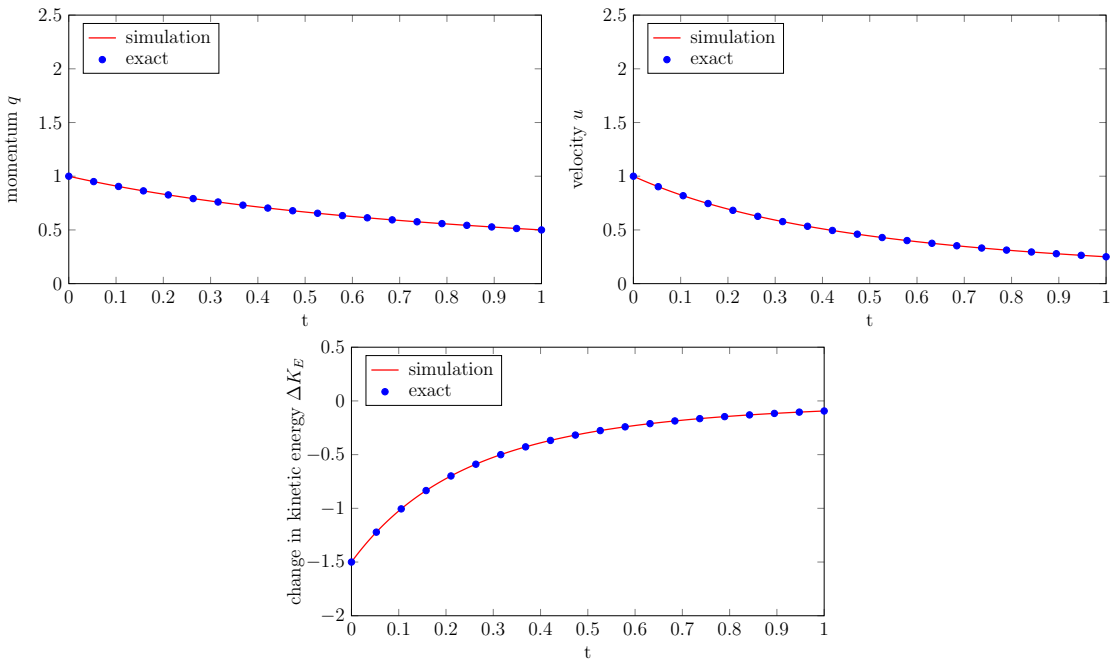

Overall, our conclusion from this numerical test focusing on an idealised scenario is that we have physically realistic solutions when the friction affect $\alpha \geq 1$, as it is within this regime that the momentum is either conserved of decreasing. As is clear from both the equations and the simulations, this occurs when the reduction in velocity is large enough to compensate for or balance the increase in water height.

The value of α also has a significant impact on the change in kinetic energy, with the rate being positive for $\alpha < 1/2$ and negative for $\alpha > 1/2$. It is also interesting to note that for $\alpha > 1/2$, over time the rate of change tends to zero due to the reduction in the velocity of the water, even though the momentum may still be increasing.

4.3.2 Comparison with experimental data

For our second test, we explore the accuracy of our numerical scheme by comparing with data taken from the flume experiment run as part of the ANR project METHODE at INRA-Orléans; we also compare our results to those obtained by Delestre and James [2008], who considered only an addition to the conservation of mass equation.

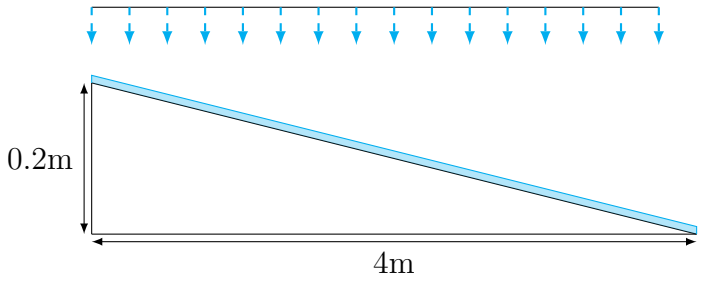

Figure 4.3: Visualisation of the flume experiment.

The experiment in question concerns a slope with a 5% gradient, an initial height $h_0 = 0$, and initial discharge $q_0 = 0$. The topography for the slope is given by $Z(x) = (4 - x)0.05$, we consider $N = 1000$ meshpoints, and we assume a CFL condition of 0.95. Rain falls onto the slope uniformly at a constant rate within a given time interval,

$$R(x,t) = \begin{cases} 50 \text{ mm/hr} & \text{if } (x,t) \in [0, 3.95] \times [5, 125] \\ 0 & \text{otherwise} \end{cases} \tag{4.3.2.1}$$

and we measure the discharge at the downstream edge of the slope up to time $T = 250$s. For our simulation, we assume the rain-induced friction level $\alpha = 1$. The hydrograph for the experiment is provided below in Figure 4.4.

The results from the simulation compare well with with the experimental data, particularly in the third and final phase when no rain is falling and the discharge is decreasing gradually over time. For the initial phase, where the discharge is increasing, the simulation matches well to begin with (up to around 25s) but subsequently appears to increase at a slower rate than in the experiment; at $t = 35$s, for example, the experiment shows a discharge level of 5.7 g/s, compared to the simulation which is at 3.59 g/s. For the secondary phase, where the discharge has stabilised, while the

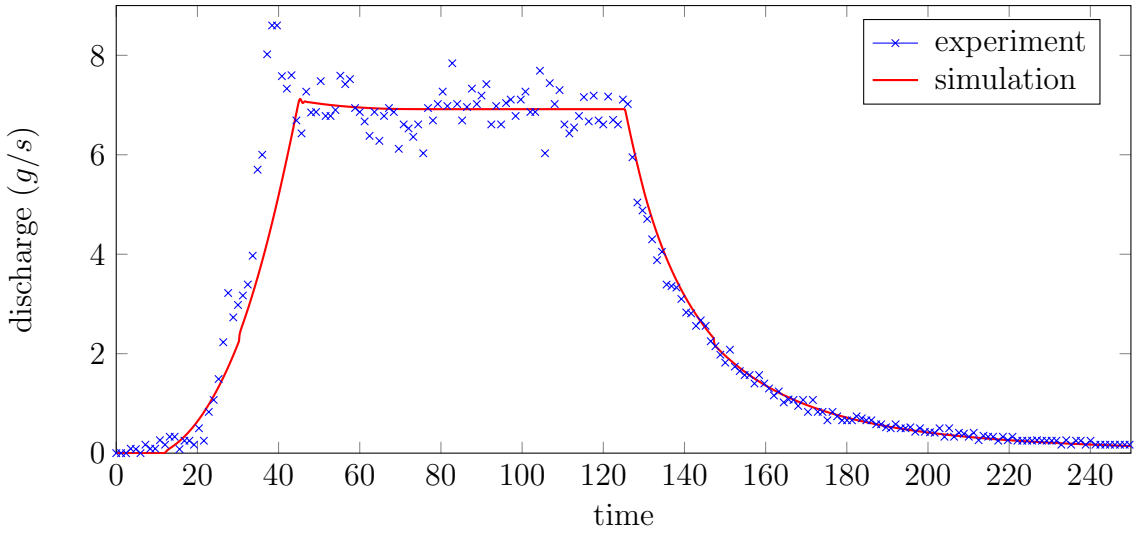

Figure 4.4: Hydrograph for the uniform slope test with both the experimental data and the simulated solution.

simulation does not capture the fluctuations that were present in the experiment, it does maintain a smooth transition through the centre of the data, and begins to decrease at the same point as the experiment.

Comparing the results of our simulation to those of Delestre and James [2008], we see that our simulation matches much better in both the initial and final phases; in the initial phase, their simulation increases a lot sooner than in the experiment, and though it begins to decrease at the correct time, it also underestimates the total discharge level in the final phase. For the secondary phase, their results are slightly lower than ours but still consistent with the experimental data.

We would also like to consider the sensitivity of our numerical model to the number of meshpoints N. To achieve this, we rerun this simulation for additional meshpoints $N = [10, 50, 100, 500]$ and compare the discharge value at the point $(x, t) = (12, 125)$. The convergence of the discharge value is shown below in Figure 4.5.

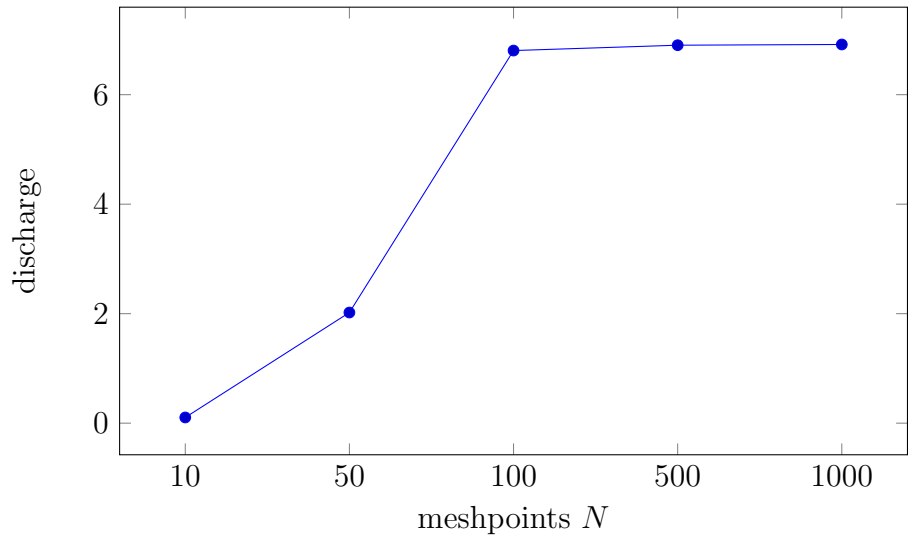

Figure 4.5: Convergence of the discharge value for increasing meshpoints N.

The results demonstrate good convergence of the discharge value as the number of meshpoints increases, with minimal difference in the outputs between $N = 100$ and $N = 1000$. Where we see significant difference is for lower meshpoint sizes; for $N = 10$ our simulation gives a poor estimation of the discharge and this continues (though to a lesser degree) for $N = 50$. This is most likely an artefact of the CFL condition we use to calculate the time-step Δt for each iteration; at these lower meshpoint values, the time-step generated is too large to accurately capture the motion of the flow, resulting in a poor solution. For the higher meshpoint values where the solution is much more accurate, we may still see discrepancies in the solution due to the CFL dependancy, but the rate of convergence lends some evidence to suggest that these differences will be minimal.

4.3.3 Single-level and three-level cascade

For our final test, we consider a similar scenario to §4.3.2 but with a higher intensity rainfall process on a slope with a much shallower gradient. We also compare how the water flows when the gradient of the slope is constant across the full domain, and how it flows when the gradient decreases periodically from the upstream to downstream end. For our simulations, we consider a spatial domain $x \in [0, 12]$, a final time $t = 40$s, a rainfall intensity $R_0 = 0.001$ which falls across the entire domain, $N = 1000$ meshpoints, and a CFL number of 0.95. Within this test, the parameters that we want to change and measure the effect of are the following:

(1) the total length of the rainfall process $T_R = 10$, 20, and 30 seconds

(2) the topography of the slope onto which the rain falls, for which we consider a constant slope (the single cascade) with $Z_1(x) = (12 - x)0.005$, and a decreasing slope (the three-level cascade, see Figure 4.6) with

$$Z_2(x) = \begin{cases} (12 - x)0.006 - 0.012 & \text{if } x \in [0, 4] \\ (12 - x)0.005 - 0.004 & \text{if } x \in [4, 8] \\ (12 - x)0.004 & \text{if } x \in [8, 12] \end{cases} \tag{4.3.3.1}$$

(3) the rain-induced friction level α, for which we take $\alpha = 0, 1$, and 5 for the single cascade and $\alpha = 0$ and 1 for the three-level cascade

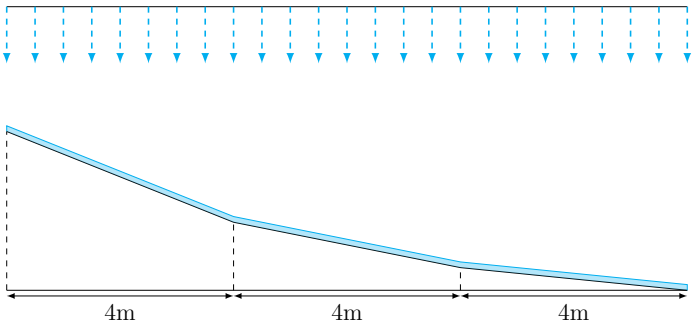

Figure 4.6: Topography for the three-level cascade, showing the decrease in gradient as we move from the upstream to the downstream end.

For our outputs, we measure the height of the flow across the entire domain at the point the rainfall stops, and we also measure the height and discharge at the downstream end (i.e. $x = 12$) up to the final time.

Starting with the height profile at $t = T_R$, we see in Figure 4.7 that for the single-level cascade, increasing the value of α causes more water to accumulate at the upstream end, as expected since the momentum of the water will decrease the higher we take α. It is interesting to note also that for $T_R = 10$, the water still accumulates to the same maximum amount irrespective of the value of α, though at different points in the domain; for longer rainfall times, this accumulation can still occur, but potentially beyond the end of the domain if the water has enough momentum.

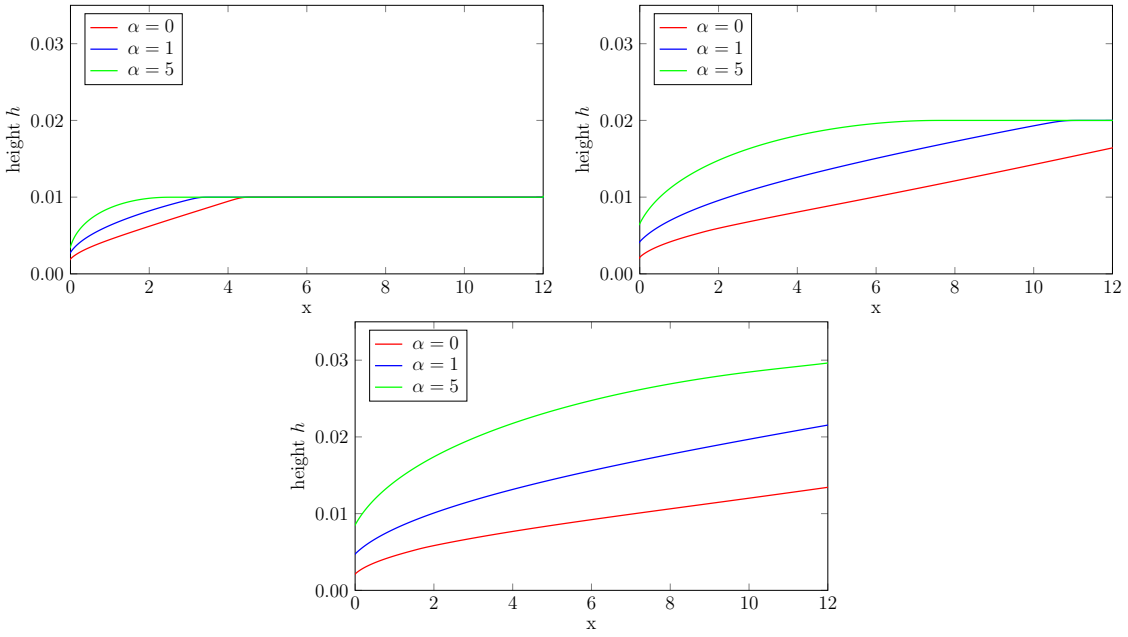

Figure 4.7: Height profiles for the single-level cascade for varying values of rain-induced friction α at the rainfall end time $T_R = 10$, 20, and 30.

For the three-level cascade shown in Figure 4.8, the reduction in gradient induces multiple waves to be formed, though these waves become more smoothed out as the rainfall time increases. This effect is reduced as α is increased, which is consistent with our expectation since the water flow will be more slowed down. Unlike the single-level cascade, the flows do not accumulate to the same amount, though this may be due to the length of the domain.

For the second part of our numerical test, we consider the height and momentum profiles over time at the end of the domain ($x = 12$). For the single-level cascade (see Figure 4.9), we see that increasing the friction level α extends the height profile of the flow, causing it to decrease at a later time. This occurs for all lengths of rainfall T_R, though notably we see that as T_R increases the length of time for which the flow plateaus is decreased.

For the momentum, the change in friction and length of rainfall has a much more pronounced effect. For $T_R = 10$, the three friction levels result in much the same profile though slightly shifted as the level increases. For $T_R = 20$ and 30, however, the profiles are more varied, with the momentum tending to change rather linearly

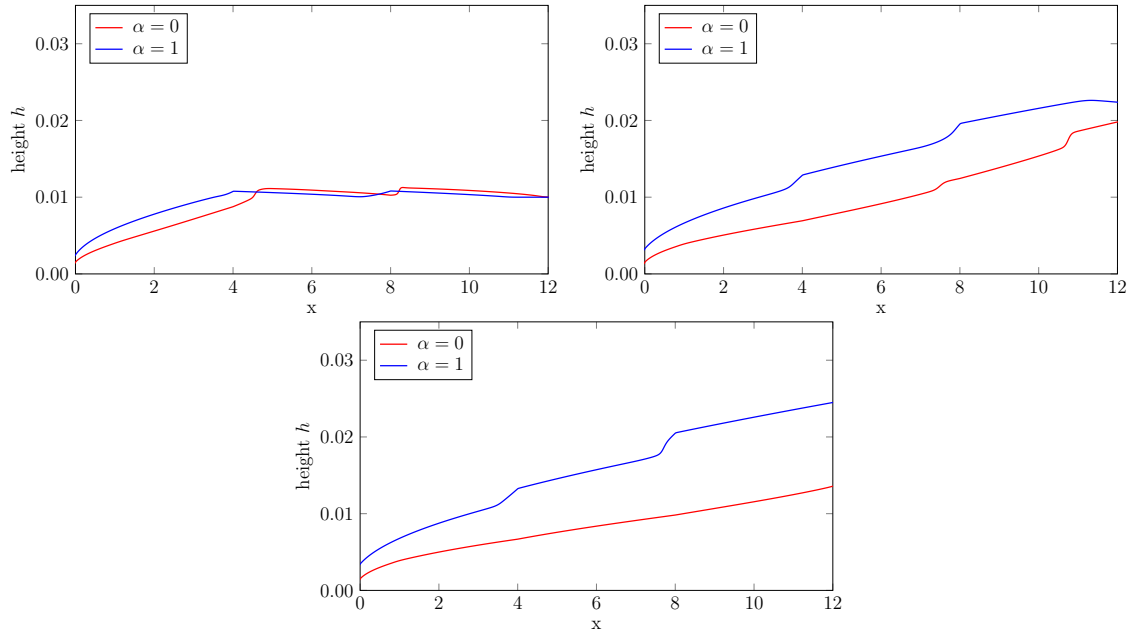

Figure 4.8: Height profiles for the three-level cascade for varying values of rain-induced friction α at the rainfall end time $T_R = 10$, 20, and 30.

for $\alpha = 0$ but showing a much more curved profile for $\alpha = 5$. We can also see that for $T_R = 30$, the momentum is decreasing when the rainfall stops for $\alpha = 0$ and 1, but continues to rise and at an increased rate for $\alpha = 5$.

The three-level cascade shown in Figure 4.10 exhibits much the same behaviour as the single-level cascade, with perhaps the most notable changes being in the height profile; for the single-level cascade the height profile for $\alpha = 0$ remains consistently below that for $\alpha = 1$, but for the three-level cascade this does not hold true between, approximately, $t = 10$ and $t = 20$. The momentum profile for the three-level cascade is very similar in behaviour to the single-level.

4.4 Conclusion

Since the envisioned application of our extended shallow water model was to real-world problems of flood inundation, it is vital that we have an accurate numerical method to simulate our extended shallow water system. Existing approaches such as finite difference or finite volume can be used, but they fail to ensure certain properties that we would like our method to have. The alternative approach we took was to instead use a kinetic formulation, rewriting our shallow water system as a single kinetic equation (which is easier to solve and guarantees the properties we want) which can then be solved using a finite volume method to find the original variables (h, q).

To demonstrate the applicability and viability of the shallow water system and associated kinetic scheme, we ran a number of numerical simulations of our model. Our focus was on demonstrating the effect the rain-induced friction level, α, has on the height and momentum profiles of the flow. In §4.3.1, we showed that increases

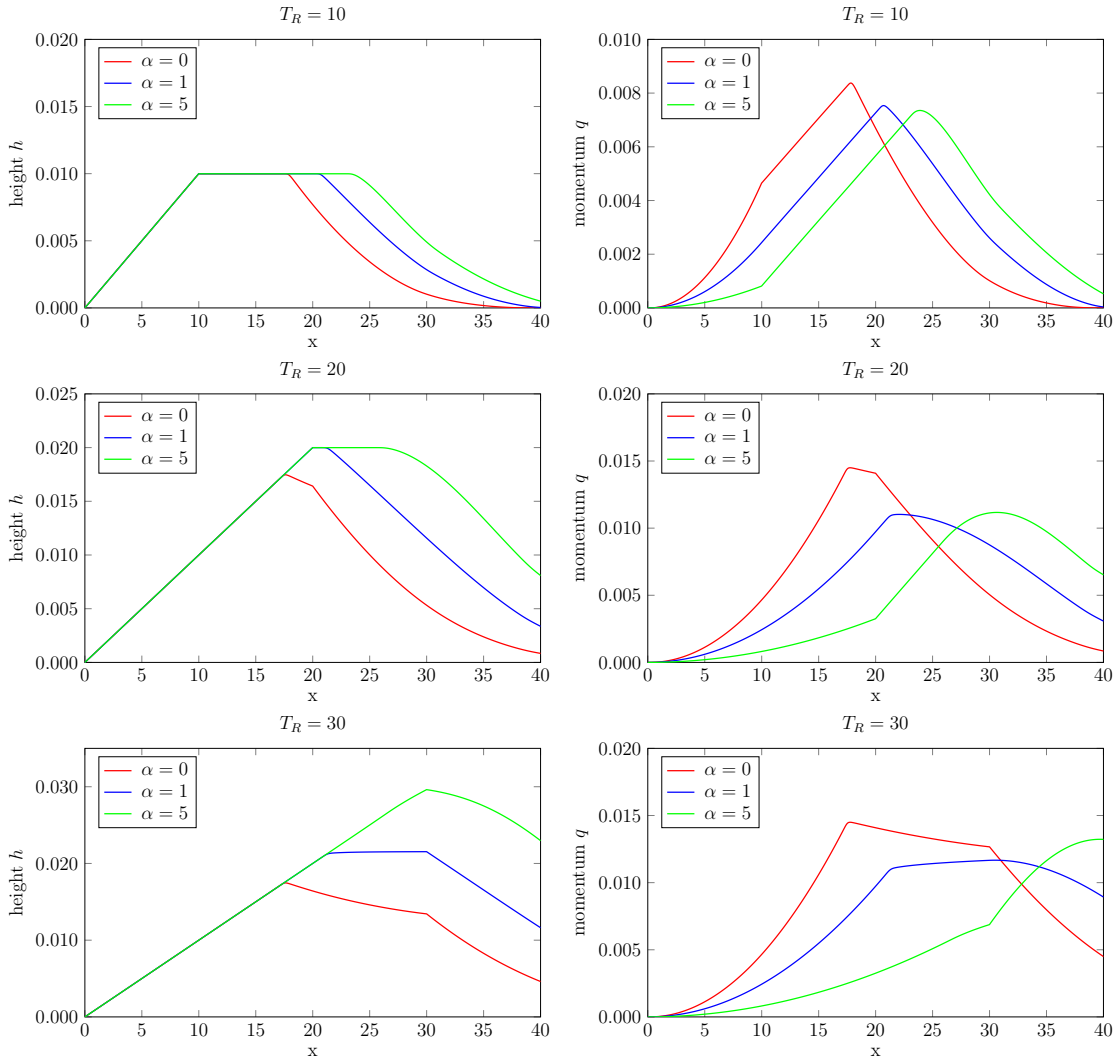

Figure 4.9: Height and momentum profiles over time for the single-level cascade for varying values of rain-induced friction α at the domain end $x = 12$.

or decreases in the momentum, velocity, and energy could be directly linked to particular regions of α, while in §4.3.3 we saw that increasing the value of α slows down the propagation of the flow (as one would expect). This is particularly important in modelling flood inundation and being able to predict the position of the leading edge of the flood event, thus justifying why it is necessary that these terms be included in the model.

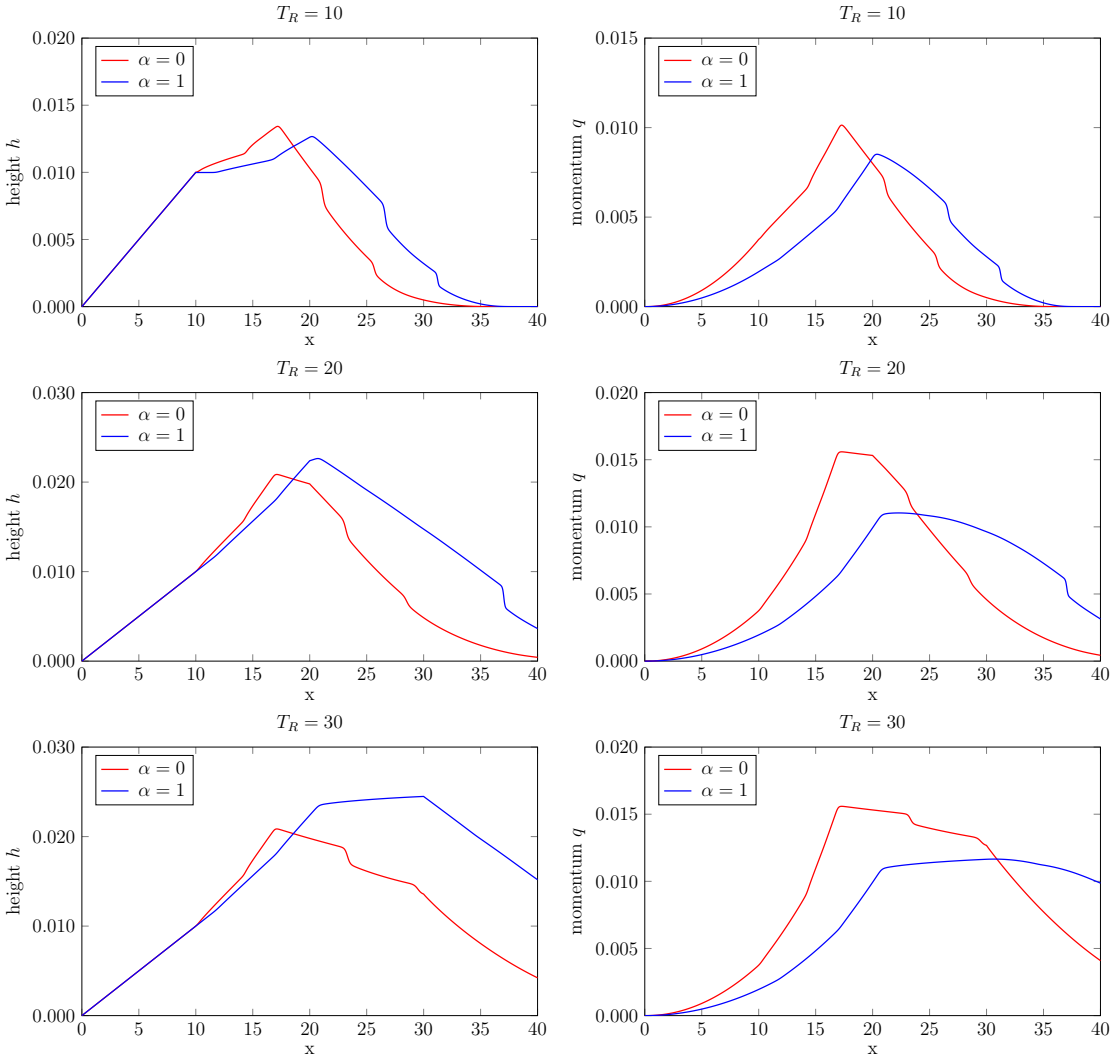

Figure 4.10: Height and momentum profiles over time for the three-level cascade for varying values of rain-induced friction α at the domain end $x = 12$.

Chapter 5

A stochastic approach to modelling rainfall

Thus far, we have shown how we can incorporate the meteorological phenomena that lead to flood inundation in our shallow water model in a mathematically rigorous manner (specifically, through adapting the boundary conditions in the Navier-Stokes equations) and developed a robust kinetic scheme that we can use to model the overall system numerically. We have not, however, addressed the question of how to actually model the precipitation and infiltration effects themselves; in our derivation of the shallow water system from Navier-Stokes in §3.1 and §3.2, we included the precipitation and infiltration effects as inflow and outflow boundary conditions without specifying their exact form, and in all of the numerical tests we ran in §4.3 the rainfall rate was assumed to be a given function of space and time.

Within this chapter we will take a step back and consider the modelling of the precipitation as a stochastic differential equation. In §5.1 we will give a brief discussion of the background and general usage of stochastic processes to modelling physical phenomena, and note some of the drawbacks of such an approach. In §5.2, we will present a number of approaches of increasing complexity for our stochastic equation for modelling the rainfall term; we will then combine the most realistic approach with a novel technique for incorporating observation data in §5.2.2 to give a new approach to predicting precipitation rates, reflecting both observed values and stochastic effects. Finally, we will present some techniques used to model such equations numerically in §5.3 and §5.4, in particular demonstrating how the improved Multilevel Monte Carlo method introduced in Giles [2006] can be applied to our extended shallow water system, and present some numerical simulations to demonstrate the validity of our approach in §5.4.3.

5.1 An introduction to stochastic processes

Before considering the representation of the precipitation, we will give a basic introduction to stochastic processes and stochastic differential equations, and present some background to their application to modelling physical phenomena. Much of this initial background comes from Kloeden and Platen [1999] and Lord et al. [2014].

5.1.1 Motivation

We begin by considering a very simple question: *why do we care about stochastic modelling?*

The simple answer is that stochastic modelling better reflects reality than deterministic (i.e. non-stochastic) modelling approaches. When applying mathematical techniques and methods to real world situations, the analysis will typically involve representing the problem as a system of ordinary or partial differential equations (referred to as ODEs and PDEs, respectively) and there are a number of methods for solving such equations.

Around the end of the 19th Century, the prevailing mathematical theory was that if all initial data for a problem could be collected, it was possible to predict the future (i.e. the solution to the problem) with absolute certainty. Albert Einstein, continuing work which had previously been developed by botanist Robert Brown, showed this belief to be false [Einstein, 1905]. The example used was the motion of a particle of dust in a volume of water (as depicted in Figure 5.1); the motion of the particle will be affected by its interactions with the water molecules, which are too complex to be described deterministically and thus require a stochastic interpretation.

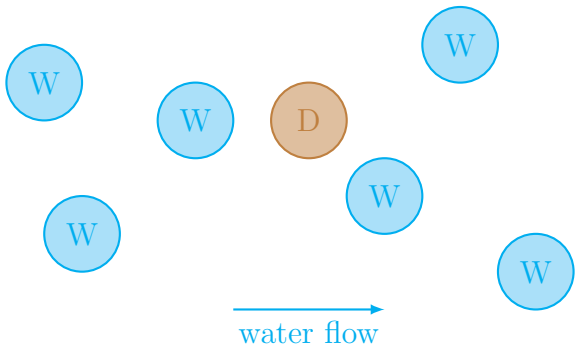

Figure 5.1: As the dust particle flows in the water, its motion will be affected by its interactions with the water molecules.

We could use ODEs or PDEs to give a good *representation* of the motion of the particle (and indeed, the stochastic equations we use will build upon an ODE or PDE framework), but they cannot describe the random interactions that occur, and so will fall short of giving an accurate enough solution.

We deal with this limitation through the use of stochastic differential equations (SDEs), whereby one or more of the terms in the equation is a stochastic process which models the random interactions that occur in the system, and thus the solution to the equation itself depends on a stochastic variable ω in addition to the space-time variables (x, t). The example above of the stochastic motion of a dust particle in water is often referred to as Brownian motion, in reference to Robert Brown's work on the problem.

The use of SDEs is not restricted to merely physical phenomena as already discussed; they are also used in modelling stock prices [Black and Scholes, 1973, Merton, 1973]

and population dynamics [Kloeden and Platen, 1999]. In each case, there is some degree of randomness that we wish to accurately model which cannot be achieved using an ODE; for example, in a stochastic population model

$$dX_t = aX_t\left(1 - \frac{X_t}{K}\right)dt + \sigma X_t\left(1 - \frac{X_t}{K}\right)dW_t \tag{5.1.1.1}$$

the inclusion of the stochastic term (multiplied by intensity σ) can vastly change the rate at which the population reaches carrying capacity (K) or possibly extinction.

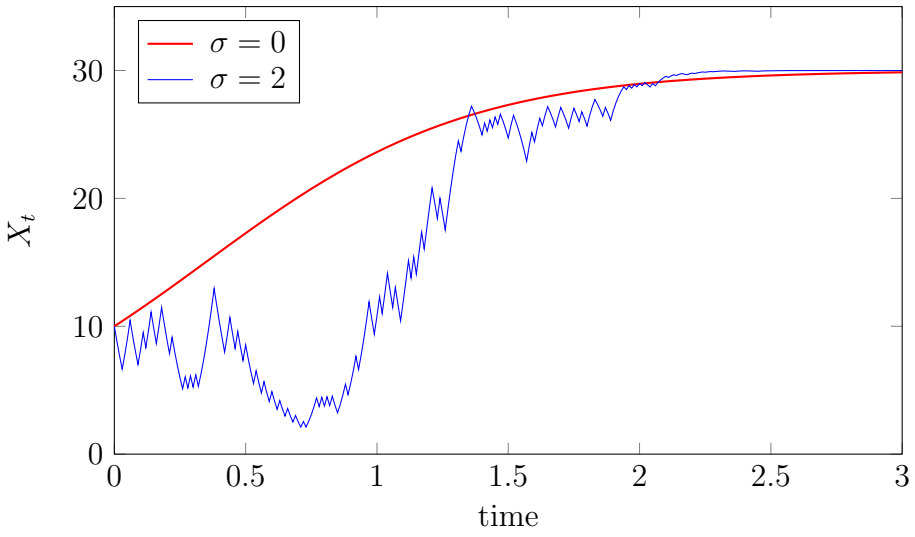

Figure 5.2: Comparison of deterministic (–) and stochastic (–) model of population growth with $X_0 = 10$, standard growth rate $a = 2$, and carrying capacity $K = 30$.

5.1.2 Wiener process

The Wiener process forms an important part of the development of stochastic differential equations, and is key in the development of more complicated stochastic processes. Due to its importance, we will explore its use in more detail, enabling us to create a foundation for developing these techniques in established probabilistic methods.

Background

We introduced the idea of stochastic modelling by considering a single particle of dust in a volume of water, which will move in an erratic and irregular fashion due to its interactions with the water particles. However, if we were to instead consider a cloud of dust particles suspended in water (see Figure 5.3), the cloud will spread throughout the volume of water due to diffusion over time and the concentration of dust at a given spatial position will change in a smooth manner. We can hence model the motion of the cloud mathematically using an ordinary or partial differential equation. This therefore gives us a rather interesting phenomenon; the erratic motion of the individual particles gives rise to a smooth motion of the mass of particles when considered as a whole.

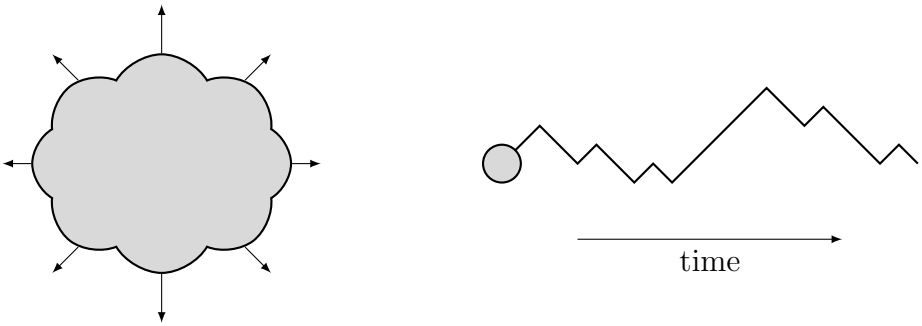

Figure 5.3: The smooth motion of the dust cloud as a whole is contrasted by the erratic motion of a single particle.

The Wiener process, named after American mathematician Norbert Wiener, was designed as a way to model the motion of these individual particles, and paths of the process exhibit similar behaviour to the erratic motion of real dust particles. The Wiener process is widely used in mathematical models involving noisy systems; one of the main reasons for such widespread use is that, in real world examples, if the noise comes from a number of independent random changes, then by the Central Limit Theorem it is predicted that the net result will be normally distributed, a trait shared by increments of the Wiener process.

Definition

We define a standard Wiener process, given by $W = \{W(t), t \geq 0\}$, to be a continuous Gaussian process with independent increments such that $W(0) = 0$, $\mathbb{E}(W(t)) = 0$, and

$$\text{Var}(W(t) - W(s)) = t - s \tag{5.1.2.1}$$

for all $0 \leq s \leq t$. From (5.1.2.1) we can determine that $W(t) - W(s)$ is $\mathcal{N}(0; t - s)$ Gaussian distributed for $0 \leq s \leq t$ and

$$\text{Var}(W(t)) = t. \tag{5.1.2.2}$$

The variance of the Wiener process will therefore grow unbounded over time, whereas the mean will always remain as zero. This means that, as time increases, the values attained by the sample path of such a process will become larger, in both a positive and negative sense to achieve a continued mean of zero.

Approximating a Wiener process

Since our intention overall is to use numerical methods to simulate the evolution of a stochastic differential equation, we will require some method for approximating a standard Wiener process; we can do this using a scaled random walk. Without loss of generality, suppose our process is over the interval $[0, T]$; we split this interval into N equal subintervals

$$0 = t_0 < t_1 < \cdots < t_k < \cdots < t_N = T \tag{5.1.2.3}$$

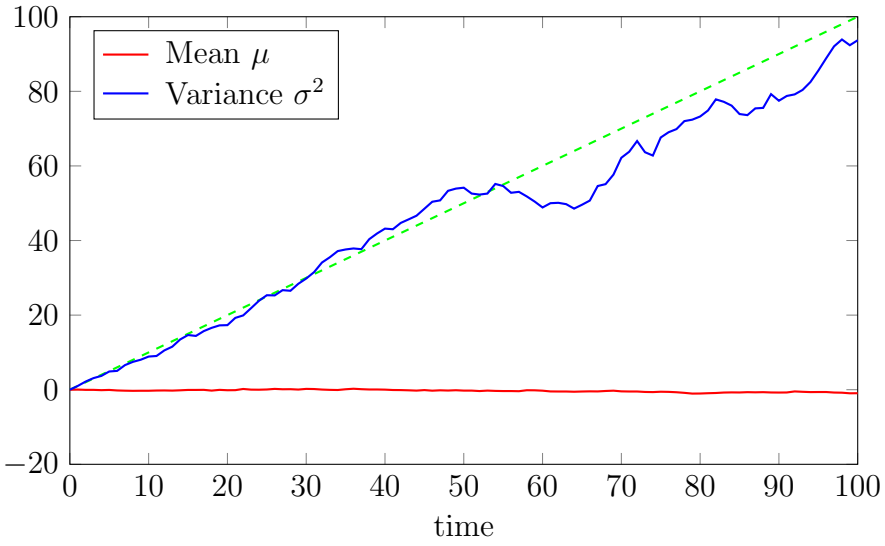

Figure 5.4: Mean and variance for 100 sample paths of $W(t)$; as expected, the variance evolves as approximately t whilst the mean remains close to zero.

where the length of each subinterval is given by $\Delta t = T/N$. From this, we can construct a simple stepwise random walk, which we denote by $Y_N(t)$, by taking steps of length $\pm\sqrt{\Delta t}$, each equally probable, at the end of each subinterval. We therefore define

$$\begin{cases} Y_N(t_0) & = 0 \\ Y_N(t_k) & = (X_1 + X_2 + \cdots + X_k)\sqrt{\Delta t} \quad \forall j = [1:N] \end{cases} \tag{5.1.2.4}$$

where the value of X_j is either ± 1, with equal probability. We can then define $Y_N(t)$ through a linear interpolation of the values (5.1.2.4), giving

$$Y_N(t) = Y_N(t_k) + \frac{t - t_k}{t_{k+1} - t_k}\left(Y_N(t_{k+1}) - Y_N(t_k)\right) \tag{5.1.2.5}$$

for $t_k < t < t_{k+1}$ and $k = [0:N]$, with initial condition $S_N(0) = 0$. In practice, we would use a (pseudo-)random number generator to generate values for X_k which we can then use to calculate (5.1.2.4) and hence (5.1.2.5).

5.1.3 Stochastic differential equations

We will now present the concept of a stochastic process and a stochastic differential equation, which ultimately we will use to model the precipitation phenomena.

Stochastic integral

We can write the general form of an ordinary differential equation (ODE) as the following system of equations:

$$\begin{cases} \dfrac{dx(t)}{dt} = a(x(t), t) \\ x(t_0) = x_0 \end{cases} \tag{5.1.3.1}$$

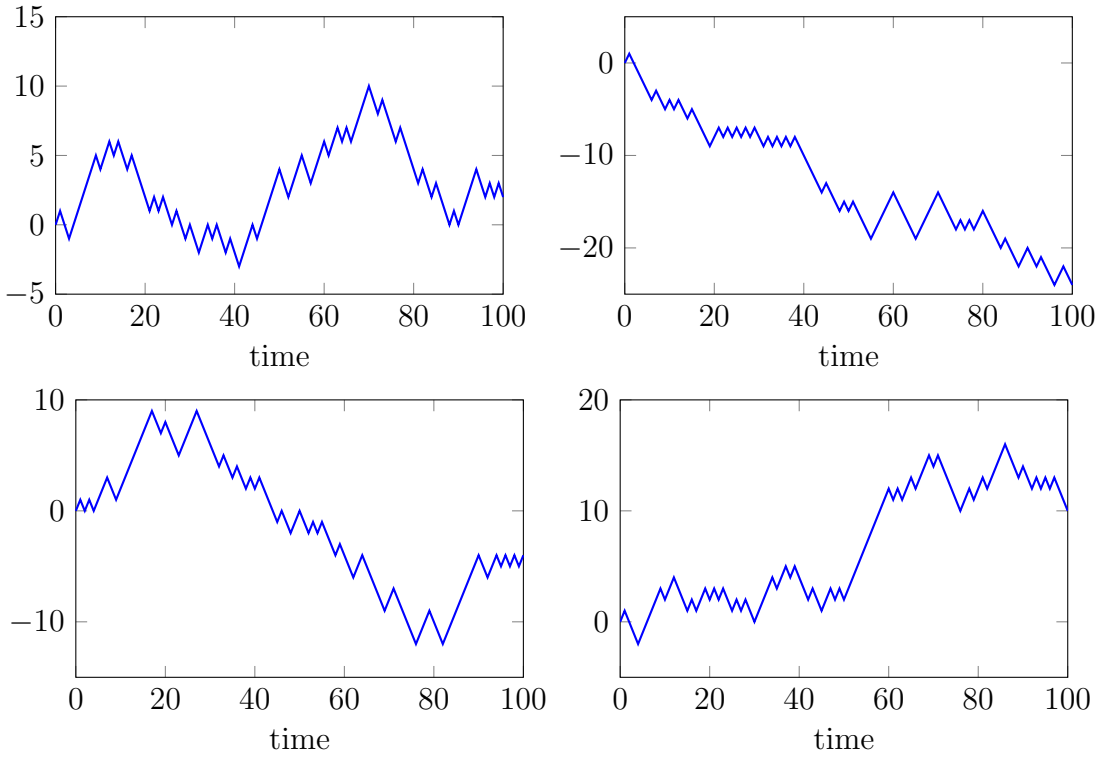

Figure 5.5: Four sample paths of the Wiener process.

for a given function $\{a(\cdot, t) : t \in \mathbb{T}\}$ and time interval $\mathbb{T}$. Through a simple rearrangement, we can rewrite (5.1.3.1) in the form

$$dx(t) = a(x, t)dt \tag{5.1.3.2}$$

and thus as the integral equation

$$x(t) = x_0 + \int_{t_0}^{t} a(x(s), s)ds. \tag{5.1.3.3}$$

The uniqueness and existence of a solution $x(t) = x(t, x_0, t_0)$ can be ensured under certain regularity assumptions on the function $a(x, t)$, such as Lipschitz continuity.

We can think of a stochastic differential equation (SDE) as an ODE with additional "randomness". We note, however, that the inclusion of random effects in an ODE does not necessarily lead to a stochastic equation, and thus we need to be clear on exactly what sort of equation we are defining. Consider the first possibility of an ODE with random coefficients, a random initial value, or that is being forced by a stochastic process; for example

$$\begin{cases} \dfrac{dx(t)}{dt} = a(\omega)x(t) + b(t, \omega) \\ x(0) = x_0(\omega) \end{cases} \tag{5.1.3.4}$$

where the forcing term b is continuous for each ω. This is known as a *random differential equation*, and is solved for each sample path as an ODE:

$$x(t, \omega) = e^{a(\omega)t} \left(x_0(\omega) + \int_0^t e^{-a(\omega)s} b(s, \omega)ds \right). \tag{5.1.3.5}$$

The second possibility, and the one that we will be using, is when the forcing term is a stochastic process; the dynamics of this formulation can be written symbolically as

$$dX_t = a(X_t, t)dt + b(X_t, t)\xi_t dt \tag{5.1.3.6}$$

where X_t is a stochastic process; that is, a sequence of random variables on a common probability space (Ω, A, P) which describes the evolution of a probabilistic system over time. If the process is defined at discrete instants of time then we call this a discrete stochastic process; similarly, a continuous stochastic process is defined for all time instants, in either a bounded interval $[0, T]$ or an unbounded interval $[0, \infty)$.

In this formulation, the function $a(X_t, t)$ represents the deterministic drift term (comparable to the term $a(x, t)$ given in (5.1.3.2)), which is perturbed by a diffusion term $b(X_t, t)\xi_t$. The ξ_t are standard Gaussian random variables for each t whilst $b(X_t, t)$ represents the intensity of the randomness; the diffusion term is typically referred to as Gaussian white noise.

In much the same way that we rearranged our ordinary differential equation into an integral equation, we can do the same for (5.1.3.6); for each sample path ω, we interpret the differential equation as

$$X_t(\omega) = X_{t_0}(\omega) + \int_{t_0}^{t} a\left(X_s(\omega), s\right) ds + \int_{t_0}^{t} b\left(X_s(\omega), s\right) \xi_s(\omega) ds. \tag{5.1.3.7}$$

For the Gaussian random variables ξ_t, we note that if we set $a = 0$ and $b = 1$ in (5.1.3.6), we have

$$dX_t = \xi_t dt \quad \Rightarrow \quad \frac{dX_t}{dt} = \xi_t. \tag{5.1.3.8}$$

Since ξ_t should be the derivative of pure Brownian motion, we can equate it to the derivative of a Wiener process W_t, and hence our integral equation (5.1.3.7) becomes

$$X_t(\omega) = X_{t_0}(\omega) + \int_{t_0}^{t} a\left(X_s(\omega), s\right) ds + \int_{t_0}^{t} b\left(X_s(\omega), s\right) dW_s(\omega). \tag{5.1.3.9}$$

From a first look, we seem to be in a good position to continue; however, this formulation presents something of a problem. A significant property of the Wiener process is that it is non-differentiable, and so the Gaussian random variable ξ_t does not exist as a conventional function. We can conclude, therefore, that the second integral in (5.1.3.9) does not exist as an ordinary integral.

We fix this problem through the use of the Itô integral. Rather than defining the integral using standard calculus, we define it as the limit of a sequence of random variables over some partition of the interval $[t_0, T]$, which in the limit will tend to zero. This approach is possible if the integrand of this second integral in (5.1.3.9) is what is known as a non-anticipating or adapted process.

Definition. *A function $G(t)$ is called a* nonanticipating *or* adapted function of t *if for all s and t such that $t < s$, $G(t)$ is statistically independent of $G(s) - G(t)$.*

This definition effectively states that the value of the function $G(t)$ should only depend on information up to time t, and thus independent of how the Wiener process behaves in the future. This consideration is motivated not only by its requirement in deriving the Itô integral, but also because the idea occurs in nature, where the unknown future cannot affect the present.

5.2 Stochastic precipitation

With the framework for our stochastic modelling approach built, we now consider how we can apply these ideas to model the precipitation process as a stochastic differential equation. We recall the extended shallow water system that we developed in Chapter 3:

$$\begin{aligned} \partial_t h + \partial_x q &= S \\ \partial_t q + \partial_x \left[\frac{q^2}{h} + \mathrm{g}\,\frac{h^2}{2} \right] &= -\,\mathrm{g}\,h\partial_x Z + S\frac{q}{h} - \left(k_R - k_I + k_0\left(\frac{q}{h}\right)\right)\frac{q}{h}. \end{aligned} \tag{5.2.0.1}$$

As our desire is to consider modelling of the precipitation term only, we will simplify this equation by assuming that infiltration is zero and thus take $S = R$.

In §5.2.1 and §5.2.2 we will consider increasingly more complex stochastic representations of the rainfall, before considering the issue of numerical approximation and Monte Carlo simulation in §5.2.3 and §5.3. Finally, in §5.4, we will consider improvements upon the standard Monte Carlo approach, giving a basic introduction to Quasi Monte Carlo simulation and exploring in more detail Multilevel Monte Carlo and its application to flood and precipitation modelling.

5.2.1 Simple stochastic rainfall

We begin by considering the most simple stochastic representation of the precipitation term: that the source term S is modelled as pure white noise in space and time. We define the rainfall intensity $S_{i,j}$ in a given cell $c_i = [x_{i-1/2}, x_{i+1/2}]$ over time interval $[t_j, t_{j+1}]$ through the integral equation

$$S_{i,j} = \int_{x_{i-1/2}}^{x_{i+1/2}} \int_{t_j}^{t_{j+1}} (\partial_{xt} w)\, dtdx \tag{5.2.1.1}$$

where $w(x,t)$ represents a white noise process. The assumption that the rainfall is pure white noise implies that the intensity at this cell should be independent of the intensity at any other spatial-temporal cell; that is

$$S_{i,j} \text{ is independent of } S_{k,l} \iff i \neq k \text{ or } j \neq l. \tag{5.2.1.2}$$

We model the rain intensity (5.2.1.1) by sampling from a Normal distribution, such that $S_{i,j} \in \mathcal{N}(0, \Delta x \Delta t_{j+1})$, where Δx is the grid cell size (taken as constant across the spatial domain) and Δt_{j+1} the time step across interval $[t_j, t_{j+1}]$, with $\Delta t_{j+1} = t_{j+1} - t_j$. To generate samples from this distribution we use the *Box-Muller transform* [Box and Muller, 1958] as follows:

(1) We generate two independent random variables U_1 and U_2 from a uniform distribution in the interval $[0, 1]$

(2) We define

$$\begin{aligned} X &= \sqrt{-2\ln(U_1)}\cos(2\pi U_2) \in \mathcal{N}(0,1) \\ Y &= \sqrt{\Delta x \Delta t_{j+1}} X; \end{aligned} \tag{5.2.1.3}$$

then $Y \in \mathcal{N}(0, \Delta x \Delta t_{j+1})$ as required. The Box-Muller transform is chosen to generate the normally distributed values due to the simplicity of its implementation and integration into our existing shallow water code; other methods (such as the *Ziggurat algorithm* or the *Marsaglia polar method*) can also be used.

Applying this method in a simple example over the space-time interval $[0, 3] \times [0, 2]$ with $\Delta x = 0.1$ and $\Delta t_{j+1} = \Delta t = 0.1$, we get the following heatmap plot for the rainfall intensity:

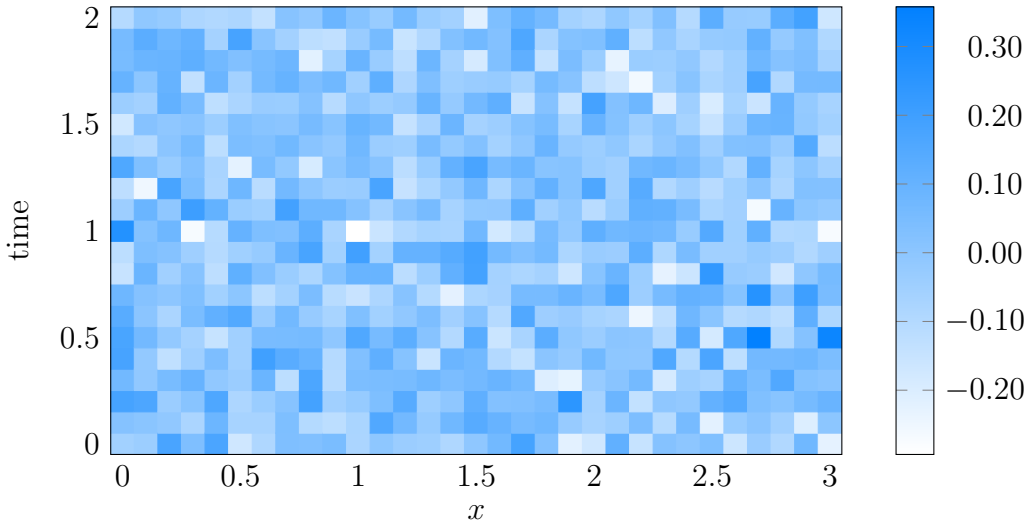

Figure 5.6: Heatmap plot of the stochastic rain function, showing the intensity of the rainfall over spatial-temporal domain $[0, 3] \times [0, 2]$.

The heatmap Figure 5.6 highlights a problem with using pure white noise as our stochastic representation of the rainfall: while the intensity of the rainfall may follow a random process, to be realistic there should be some degree of correlation in both space and time. Since the assumption of the rainfall as pure white noise implies that each spatial-temporal cell is uncorrelated, we will need to go beyond this if we want to determine a stochastic representation for the precipitation that has some degree of realistic correlation. To achieve this, we impose the following conditions on our stochastic representation:

- the closer two cells are (spatially and temporally), the more likely their intensities are to be correlated
- two cells that are next to one another can be uncorrelated, but this should have a low probability of occurring

These two points infer that sudden jumps in the rainfall intensity can occur, but they shouldn't occur too often.

Going back to our stochastic differential equation formulation, an obvious first approach would be to model the stochastic precipitation as a simple Wiener process, i.e.

$$dS(x, t) = b(x, t)dW_t. \tag{5.2.1.4}$$

We present in Figure 5.7 the output from modelling this formulation on the domain

$(x,t) \in [0,4] \times [0,2]$ for a single sample path ω with two intensity functions:

$$b(x,t) = 1 \quad \text{and} \quad b(x,t) = \frac{(x-2)^2}{4} \tag{5.2.1.5}$$

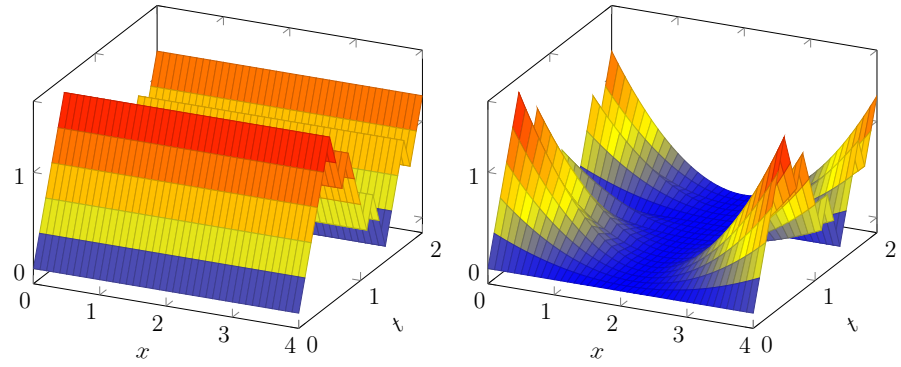

Figure 5.7: Representation of the precipitation, $S(x,t)$, as a Wiener process with both a constant and spatially-variant intensity function $b(x,t)$.

The formulation (5.2.1.4) will ensure a reasonable correlation in time and thus go some way to achieving our first condition, but the lack of spatial variability (aside from the diffusion function) presents something of an issue and makes it difficult to achieve the second condition. To address this, we consider the way in which precipitation is produced. In general, rainfall does not occur as a single event but as a collection of storms, each with their own start time, duration, and location. This suggests, therefore, that rather than considering our rainfall as a single stochastic process, we should instead consider it as a summation of stochastic events.

In light of this, we adopt for our stochastic representation a *weather generator* approach (see §2.4 and the references contained therein for an overview of the relevant literature). We assume that our precipitation is represented by a collection of storm cells which exist in the full spatial-temporal domain Ω. We model the storm variables as stochastic processes:

- storm arrival $T_s = \text{Pois}(\beta)$
- storm duration $T_d = \text{Exp}(\nu)$
- storm location $T_l = \text{Unif}(\cdot)$ on the spatial domain

The parameters β and ν are assumed to be given, and will in general be based on real-world measurements; for example, we can use previous storm occurrences to estimate the expected duration of a single storm, which will then determine the value ν. Each individual storm cell will occupy a subset of the domain Ω, which we denote by Ω_j for $j = [1:J]$, incorporating these three variables. We present in Algorithm 5.1 a simplified algorithm of the weather generator approach.

We can then model the intensity of each individual storm as a separate Wiener process, with the overall precipitation function given by the combined equation

$$dS(x,t) = \sum_{j=1}^{J} \mathbb{I}_{\Omega_j} \left(b(x,t) dW_t^{(j)} \right). \tag{5.2.1.6}$$

Algorithm 5.1 Weather generator algorithm

procedure WEATHERGENERATOR
    specify final time T
    initialise total storm time $T_{\max} = 0$
    counter for the storm cell number $j = 0$

    while $T_{max} < T$ **do**
        $j = j + 1$ % iterate storm count
        $T_s(j) = \text{Pois}(\beta)$ % sample time to next storm
        $T_{\max} = T_{\max} + T_s(j)$ % track cumulative storm time

        $T_d(j) = \text{Exp}(\nu)$ % sample duration of next storm
        $T_l(j) = \text{Unif}(\cdot)$ % sample location of next storm
    end while
end procedure

This formulation ensures that the closer two cells are the more likely they are to be correlated, and also allows for jumps in the intensity that do not occur too regularly.

To demonstrate this approach, we provide in Table 5.1 and Figures 5.8 and 5.9 an example of 3 generated storms with respective storm arrival, duration, and location values; combining these storms will then give us our overall precipitation function.

Table 5.1: Generated values for the 3 storms and associated domain Ω_j.

Storm no. j	$T_s(j)$	$T_{\max}$	$T_d(j)$	$T_l(j)$	Ω_j
1	0.3	0.3	1.2	3.6	$[3.5, 3.7] \times [0.3, 1.5]$
2	0.7	1.0	0.8	0.8	$[0.7, 0.9] \times [1.0, 1.8]$
3	0.2	1.2	0.4	1.2	$[1.1, 1.3] \times [1.2, 1.6]$

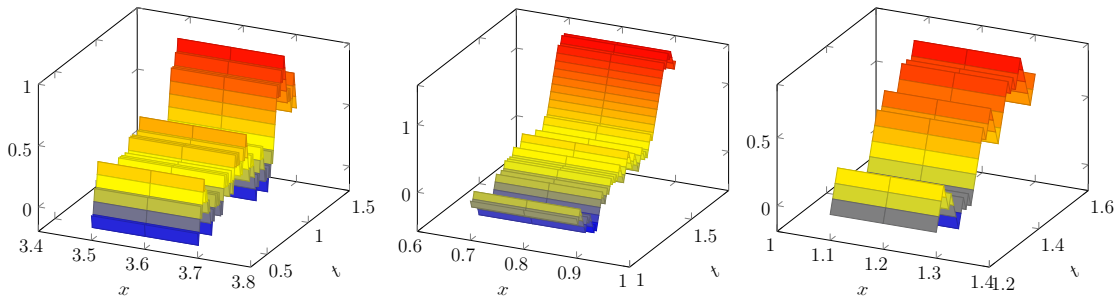

Figure 5.8: Surface plots for each of the 3 storm cells generated.

We note that we have assumed a given intensity function $b(x, t)$ which is identical for all generated storms. Our weather generator algorithm detailed above could, however, be extended to allow for different "variations" of storms which each have different parameter rates. This work is left for future research.

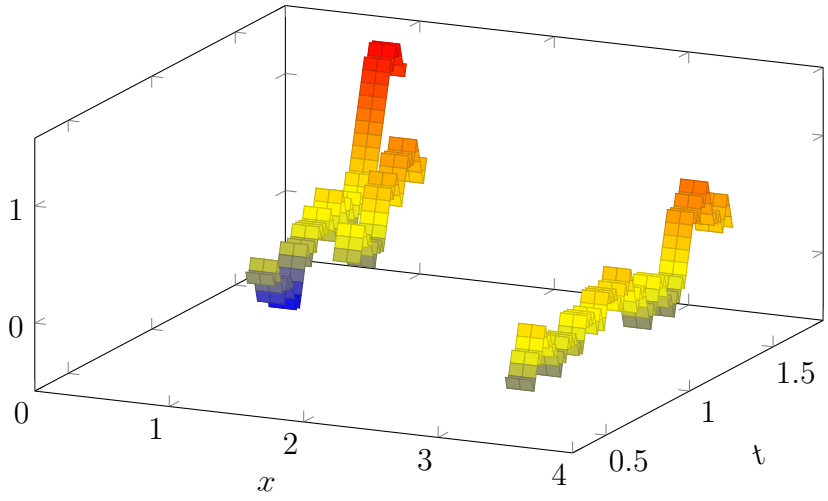

Figure 5.9: Surface plot for the full precipitation.

5.2.2 Rainfall observation data

The approaches we have detailed thus far to modelling the precipitation stochastically have focused on the diffusion term, which we have represented as a stochastic process (in particular, pure white noise ω and a Wiener process W). In this section, we would like to explore the deterministic drift term and an approach that should ensure the precipitation term reflects reality.

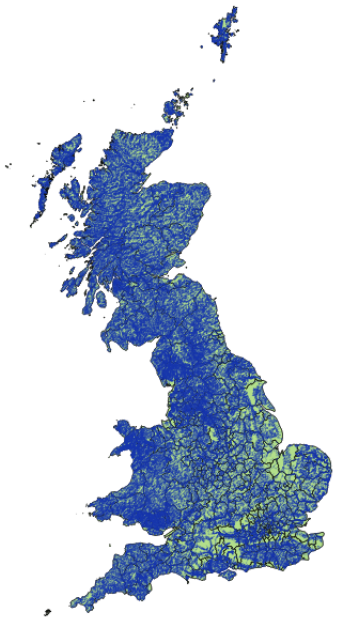

Figure 5.10: River network in the United Kingdom. Contains OS data © Crown copyright and database right (2017)

Within industrial applications the basis for any prediction of future rainfall rates is the use of observation data sourced from rain gauges, which record the daily precipitation rate at a given location. In the United Kingdom, there is an extensive network of rain gauges which are administered by the Met Office and monitored daily. There is also an archive of historical data for these gauges, with the data for

some gauges going back over 100 years [Met Office, 2017]; the length of these records provides greater assurance on the accuracy of any predictions of future rates.

Our intention is to incorporate observation data from one or more rain gauges into our stochastic precipitation equation. This can be achieved by adding a drift term, which we will denote very generally by $a(\cdot)$, to our stochastic equation to give

$$dS(x,t) = \sum_{j=1}^{J} \mathbb{I}_{\Omega_j} \left(a(\cdot)dt + b(x,t)dW_t^{(j)} \right) \tag{5.2.2.1}$$

through which we hope to capture any underlying patterns in the rainfall at the location. The question thus becomes exactly how to define this function based on the observation data we have available.

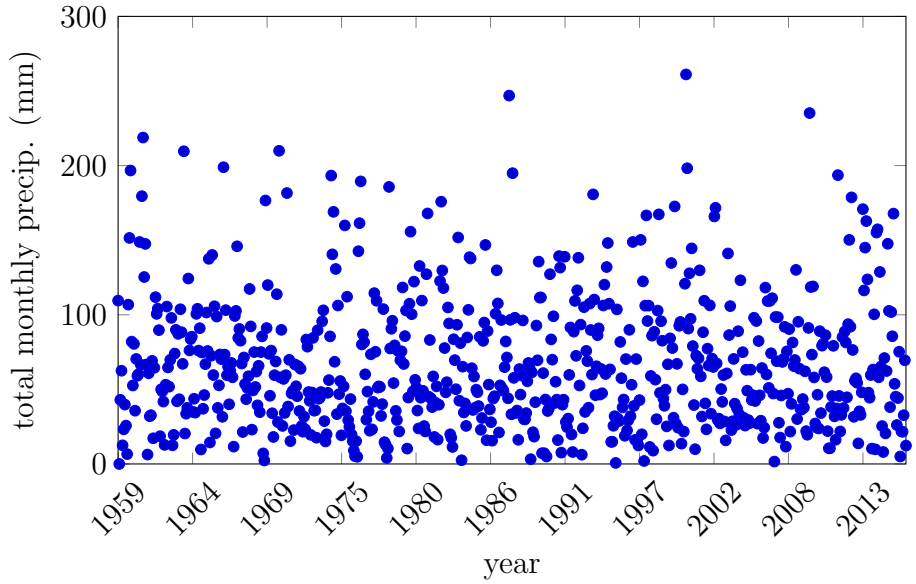

Figure 5.11: Total monthly precipitation for an example rain gauge.

In Figure 5.11 we present the data from the Eastbourne weather station, which has around 60 years of records (a reasonably long length of record). However, we can notice very quickly that it will be problematic to use this data set in its entirety, as the data is too sporadic for any meaningful conclusions or approximations to be made. We therefore aggregate the data as follows:

(1) Organise the data from the rain gauge with the total monthly precipitation for each year in columns

(2) For each month, calculate the average monthly precipitation (for months where data is missing, we exclude this from our averaging)

(3) Divide the average by the number of days in each month to determine a total daily precipitation rate

We provide in Table 5.2 a cross-section of this aggregation applied to the data from the Eastbourne weather station, together with the resulting rainfall intensity plot in Figure 5.12.

Table 5.2: Aggregation of the rain gauge data from the example Eastbourne weather station.

Month	**Days**	**1959**	**1960**	$\cdots$	**2016**	**Average**	**Daily precip.**
Jan	31	109.5	82	$\cdots$	167.8	83.7	2.70
Feb	29	0	52.6	$\cdots$	53.7	54.3	1.87
$\vdots$	$\vdots$			$\vdots$			
Dec	31	196.7	125.3	$\cdots$	12.3	91.5	2.95

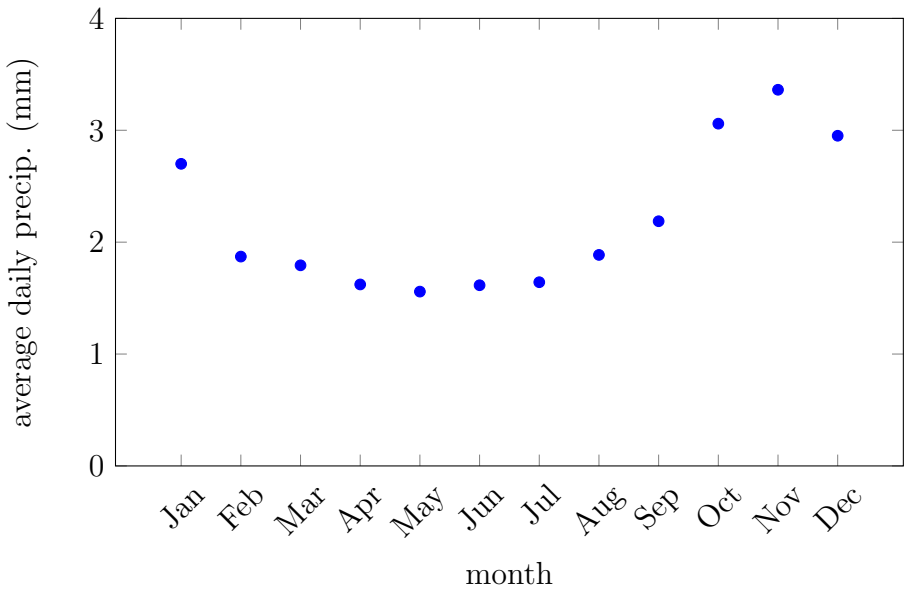

Figure 5.12: Average total daily precipitation for the rain gauge.

Looking at the aggregated data, we can see a clear seasonality in the precipitation rate that we would like to capture, suggesting that some form of sinusoidal line would fit the data best. To achieve this, we introduce a new time variable s measured in days, and define January 1st as $s = 1$, January 2nd as $s = 2$, and so on, up to $s = 366$ for December 31st. We also assume that the average daily precipitation rates are assigned to the first day in each month. Our approximation to the data is then given by

$$a(s) = \left(\frac{r_{\max} - r_{\min}}{2}\right) \cos\left(\frac{2\pi\,(s - s_{\max})}{366}\right) + \left(\frac{r_{\max} + r_{\min}}{2}\right). \qquad (5.2.2.2)$$

The choice of a cosine curve is to ensure we capture the seasonality of the data, and we multiply by $2\pi/366$ to ensure we fit our curve to the full year of data. We subtract $s_{\max}$, the day on which the maximum daily precipitation $r_{\max}$ occurs, to ensure our approximation captures the maximum precipitation rate and the time at which this occurs, since from a flood modelling perspective the maximum amount of rain we can expect to see is going to have the greatest impact. The final adjustments, multiplying by half the range and adding the average, ensure we get the correct vertical fit for our cosine curve to the data.

Applying this to our gauge from above, we get the plot shown in Figure 5.13.

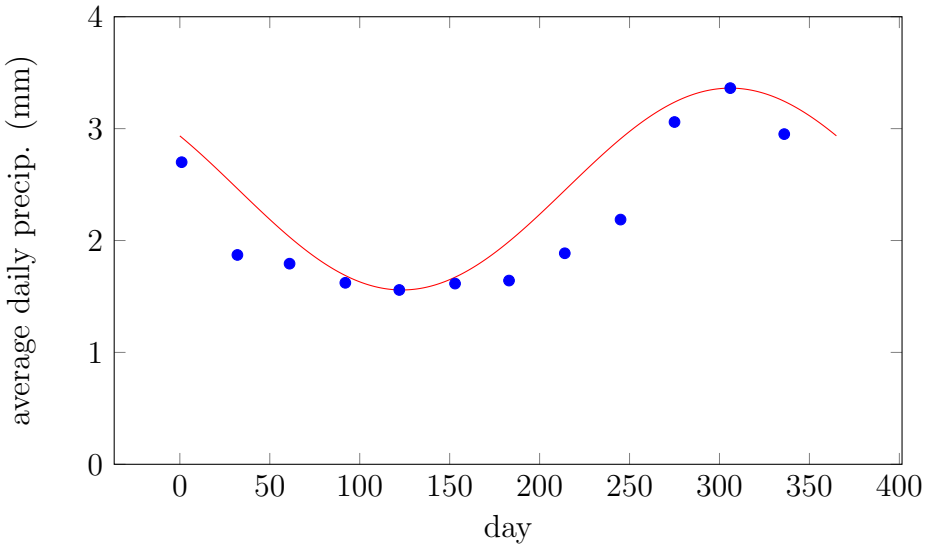

Figure 5.13: Fit of the approximation $a(s)$ to the exact data.

We can see that the fit to the data is reasonably good, though we do overestimate the precipitation in the second half of the year. Applying this approach to data from two other rain gauges, we again get a good approximation of the daily precipitation rate.

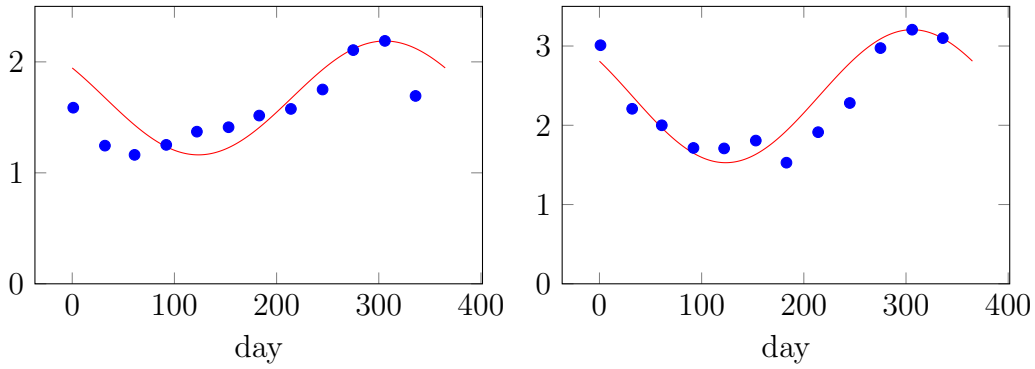

Figure 5.14: Approximation for two other rain gauges.

Bringing the various components together, our stochastic precipitation equation is given by

$$dS(x,t,s) = \sum_{j=1}^{J} \mathbb{I}_{\Omega_j} \left(a(s)dt + b(x,t)dW_t^{(j)} \right)$$

$$a(s) = \frac{1}{\lambda}\left[\left(\frac{r_{\max} - r_{\min}}{2} \right) \cos\left(\frac{2\pi\,(s - s_{\max})}{366} \right) + \left(\frac{r_{\max} + r_{\min}}{2} \right) \right]$$

with dual time scales: $t \in [0, T]$ for the underlying unit of time and $s \in [1 : 366]$ in days.

Before we continue, we take a second to explain each term in this formulation, how it contributes to approximating the rate of precipitation, and how each term will be estimated. The formulation states that the precipitation is formed as the summation of J storm cells, with the spatial-temporal domain Ω_j for each cell generated as a combination of stochastic processes. The intensity for each cell is given by a stochastic equation, with a drift term $a(s)$ derived from observation data and a diffusion term given by a Wiener process. This drift term follows a sinusoidal formulation fitted to observation data to capture the seasonality of the rainfall and, due to the differing time scales, is scaled by a variable λ which will depend on the units used for the time t (for example, if t is in days then $\lambda = 1$; if t is in hours, then $\lambda = 24$).

5.2.3 Numerical approximation

The standard approach to approximating a stochastic differential equation follows much the same framework as that for ordinary differential equations; the main difference, as one would expect, is the treatment and approximation of the Wiener process. We also note that the solution to the SDE will have an additional dependence on the sample path ω, and thus each time we run our numerical simulation we will have a different solution. This issue will be addressed in greater detail in §5.3.

Before considering the numerical approximation of our full stochastic precipitation term $S(x,t,s)$, we will first consider a simplified version for a single storm cell

$$dS(x,t,s) = a(s)dt + b(x,t)dW_t \tag{5.2.3.1}$$

with initial condition $S(\cdot,0,s) = S_0(\cdot,s)$. We partition the time domain $[0,T]$ into a sequence of discretisation points

$$0 = \tau_0 < \tau_1 < \cdots < \tau_M = T \tag{5.2.3.2}$$

where $\tau_m = \tau_{m-1} + \Delta\tau_m$ for $m = 1,\ldots,M$, and using the Euler-Maruyama method, integrate (5.2.3.1) over the time interval $[\tau_m, \tau_{m+1}]$ to get

$$\begin{aligned} \int_{\tau_m}^{\tau_{m+1}} dS(x,t,s) &= \int_{\tau_m}^{\tau_{m+1}} a(s)dt + \int_{\tau_m}^{\tau_{m+1}} b(x,t)dW_t \\ S(x,\tau_{m+1},s) - S(x,\tau_m,s) &= a(s)\left(\tau_{m+1} - \tau_m\right) + \int_{\tau_m}^{\tau_{m+1}} b(X_t,t)dW_t. \end{aligned} \tag{5.2.3.3}$$

We approximate the stochastic process $S(x,\tau_m,s)$ by $Y_m(x,s)$ and the integral as

$$\int_{\tau_m}^{\tau_{m+1}} b(x,t)dW_t \approx b(x,\tau_m)(W_{\tau_{m+1}} - W_{\tau_m}) \tag{5.2.3.4}$$

giving us, for $m = [0 : M-1]$,

$$\begin{cases} Y_{m+1}(x,s) = Y_m(x,s) + a(s)\Delta\tau_{m+1} + b(x,\tau_m)\Delta W_{m+1} \\ \quad Y_0(x,s) = S_0(x,s). \end{cases} \tag{5.2.3.5}$$

where, for simplicity, we define the Wiener process term as

$$W_{\tau_{m+1}} - W_{\tau_m} = \Delta W_{m+1} \in \mathcal{N}(0, \Delta t_{m+1}), \tag{5.2.3.6}$$

which we can approximate using the method we detailed in §5.1.2. Extending this definition to include all storm cells generated, our numerical approximation for $m = [0 : M-1]$ is given by:

$$\begin{cases} Y_{m+1}(x,s) = Y_m(x,s) + \sum_{j=1}^{J} \mathbb{I}_{\Omega_j} \left(a(s)\Delta\tau_{m+1} + b(x,\tau_m)\Delta W_{m+1}^{(j)} \right) \\ \quad Y_0(x,s) = S_0(x,s). \end{cases} \tag{5.2.3.7}$$

5.3 Monte Carlo methods

We demonstrated in §5.2.3 how our stochastic precipitation term could be approximated numerically. For each storm cell we generate a new sample path ω which is used to determine the intensity of the precipitation for that particular cell, and each time we run our shallow water simulation, we will get a new sequence $\{\Omega_j, \omega_j\}_{j=1}^{J}$ which will give a unique precipitation S as the source term. We need to determine, therefore, how we can make sense of the outputs from these simulations. The Monte Carlo method is one such possible approach.

To explain the typical procedure for a Monte Carlo simulation (and to motivate the approach we will use for our shallow water system), we will consider a very simple example of using the Monte Carlo method to approximate the integral of the equation $y = (2x-1)^2$ on the domain $[0,1]$, as shown in Figure 5.16. We proceed as follows:

(1) define our domain of consideration, $(x,y) \in [0,1]^2$

(2) model the system as one or more distributions, in this case a uniform distribution $U([0,1]^2)$

(3) randomly generate N points (inputs) over the domain following the distribution

(4) perform a deterministic computation on the inputs; for this we count the number of points, N_p, below the line $y = (2x-1)^2$

(5) calculate the quantity of interest; the integral of our equation over the domain $x \in [0,1]$ is approximated by the ratio of points below the line to the total number of points (N_p/N)

As we generate a greater number of inputs N, our calculated integral will become closer to the true solution (in this case, $1/3$).

Applying the Monte Carlo method to our shallow water system with stochastic precipitation, our approach is as follows:

(1) define our space-time domain of consideration, $(x,t) \in [0,L] \times [0,T]$

(2) model the system as one or more distributions; in this case, we model the stochastic component of our precipitation as a Wiener process on space-time domain $\{\Omega_j\} \times [0,T]$

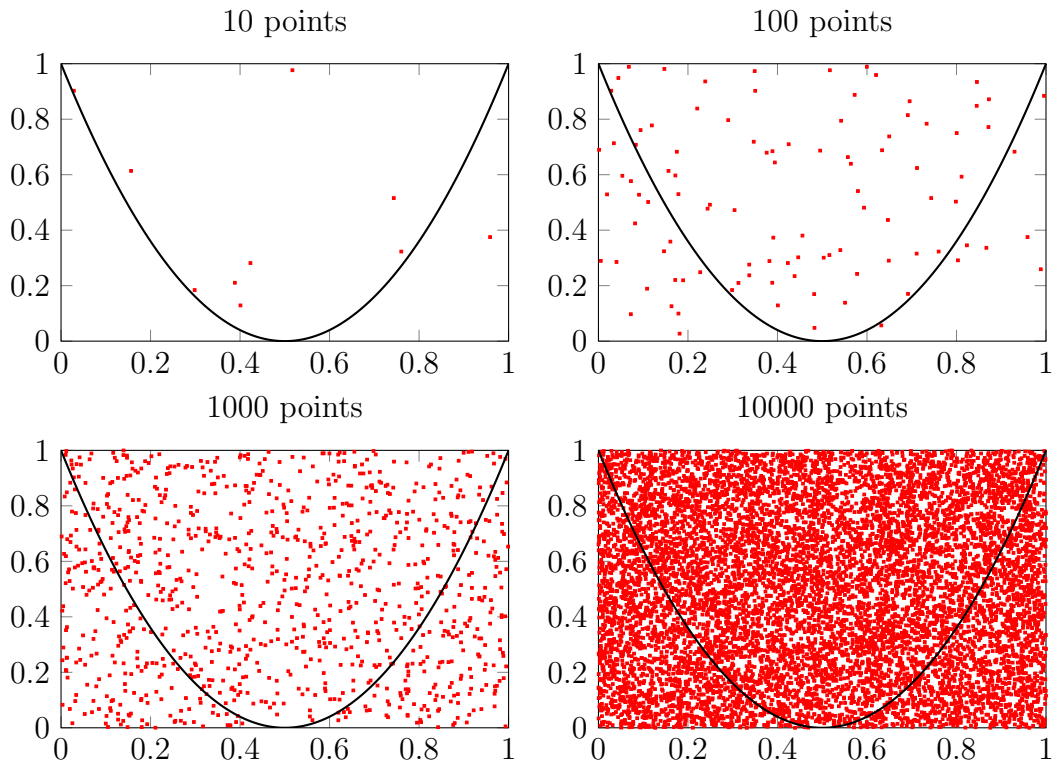

Figure 5.15: Monte Carlo simulation to determine the integral of the function $y = (2x-1)^2$ over the domain $[0,1]^2$.

Table 5.3: Calculating our Monte Carlo approximation and associated error.

Points N	**Count** N_p	**Calculated integral**	**Relative error**
10	1	0.1	70%
100	28	0.28	16%
1000	347	0.347	4.1%
10000	3313	0.3313	0.61%

(3) randomly generate sample paths ω_j over the domain for each storm cell generated

(4) perform a deterministic computation on the inputs; that is, run our shallow water model with inputs ω_j

(5) calculate the quantity of interest; *specified below*

The first four steps are relatively simple to define; the question is how to determine the quantity of interest we want to measure. For each simulation we run, the outputs from our shallow water system will be the height and momentum at each spatial and temporal grid point.

In modelling flood inundation, our interest is in understanding the water height and the probability that it will exceed a given value. Considering the expected maximum water height $\mathbb{E}[h_{\max}]$ at just the final time T may mean we miss events that occur prior to that, so the approach we take instead is to calculate for simulation k the

maximum water height achieved at any point in space and time:

$$M_k = \max_{i,n} \; h(x_i, t_n) \tag{5.3.0.1}$$

Calculating this for each of our N simulations, we can then define our shallow water Monte Carlo estimator as

$$\mathbb{E}[h_{\max}] \approx \mu_{\text{SW-MC}} = \frac{1}{N} \sum_{k=1}^{N} M_k \tag{5.3.0.2}$$

The final step in the process we outlined above thus becomes

(5) calculate the quantity of interest, the average maximum water height over time:

$$\mu_{\text{SW-MC}} = \frac{1}{N} \sum_{k=1}^{N} M_k. \tag{5.3.0.3}$$

A problem with the estimator (5.3.0.2), however, is that for a very large domain what occurs in one part of the domain (a very high water height, for example) may not be reflected in another part of the domain (where there might be almost no change in the water height). This will be particularly true if we consider more complex topographies, since this will often have a large influence on the level of water height produced. Another approach, therefore, is to consider the maximum at each grid-point instead:

$$M_k(x_i) = \max_{n} \; h(x_i, t_n) \tag{5.3.0.4}$$

and hence calculate our estimator as

$$\mu_{\text{SW-MC}}(x_i) = \frac{1}{N} \sum_{k=1}^{N} M_k(x_i) \tag{5.3.0.5}$$

We note also that, instead of considering just the average, we could also calculate from these values a probability distribution of the chance that any given water height will be exceeded.

5.4 Quasi and Multilevel Monte Carlo

A major problem with the standard Monte Carlo method is the computational cost required to achieve an accurate solution. To achieve $\mathrm{O}(\varepsilon)$ accuracy, we require the number of samples of the discretisation $N = \mathrm{O}(\varepsilon^{-2})$ and the time step $\Delta t = \mathrm{O}(\varepsilon)$; thus the computational cost can be calculated as

$$\text{cost} = \frac{MT}{\Delta t} = \frac{\mathrm{O}(\varepsilon^{-2})}{\mathrm{O}(\varepsilon)} = \mathrm{O}\left(\varepsilon^{-3}\right) \tag{5.4.0.1}$$

where $MT/\Delta t$ is the total number of steps we have to compute. In practice, this means that if we wanted to achieve a 10x increase in accuracy, the computational cost will increase by 1000. It is desirable, therefore, to look at ways in which this cost can be reduced, and there are two main methods for consideration:

- Quasi Monte Carlo
- Multilevel Monte Carlo

Our primary focus will be on Multilevel Monte Carlo, but we will give a brief overview of Quasi Monte Carlo as well for completeness.

5.4.1 Quasi Monte Carlo

When we considered the application of the standard Monte Carlo to the simple example of finding

$$\int_0^1 (2x-1)^2 dx \tag{5.4.1.1}$$

we generated N random points uniformly over the domain $[0,1]^2$, and approximated the integral as the ratio of points below the line $y = (2x-1)^2$ to the total number of points. The positioning of these points in the domain is uniform but ultimately random, and if we look at the plots in Figure 5.16 we can see that there are regions where the density of points is higher than in others.

The Quasi Monte Carlo (QMC) approach [Niederreiter, 1992] is to change the way in which the random numbers used to cover the domain are generated. The sequence of random numbers is chosen in such a way that the number of points in the sequence that fall in an arbitrary subdomain $\mathcal{D}$ is close to proportional to the measure of $\mathcal{D}$ (i.e. if $\mathcal{D}$ is a quarter of the total domain, then the number of points falling in $\mathcal{D}$ should be close to a quarter). The measure of equidistribution of points in a domain is known as the *discrepancy*, and thus the sequence of random numbers for Quasi Monte Carlo should have low-discrepancy. The rate of convergence for Quasi Monte Carlo is increased to $\mathrm{O}(N^{-1})$ from $\mathrm{O}(N^{-0.5})$ and hence we have a lower computational cost.

For our specification application of Monte Carlo to stochastic precipitation, the randomly generated inputs are the sample paths ω_j that we use to approximate the Wiener processes; thus the analogy with the standard Quasi Monte Carlo approach is that the sequence of samples paths ω_j should have low-discrepancy (in some manner). One possible approach to ensure this is to use a *constrained random walk*, fixing the value of the sample path at the start and end times:

$$\begin{cases} \omega_j(0) = 0 \\ \omega_j(T) = x_j \end{cases} \tag{5.4.1.2}$$

where the sequence of points $\{x_j\}$ is distributed in such a way as to have low-discrepancy. This constraint can be achieved by introducing a bias on the direction of the random walk, which is recalculated after each step to ensure that the sample path will always converge on the desired end value [Lawless, 2013].

5.4.2 Multilevel Monte Carlo

We have seen how the standard Monte Carlo method can be extended to Quasi Monte Carlo by exploiting the choice and sequencing of the random inputs to the

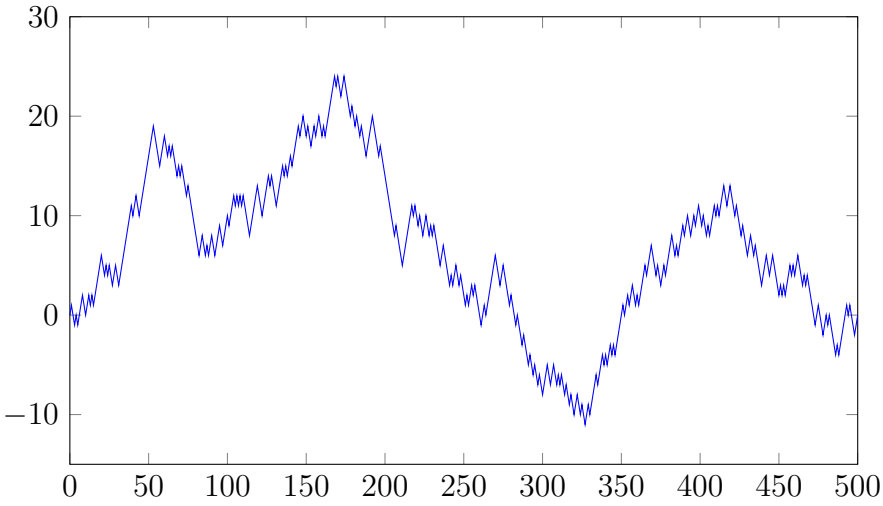

Figure 5.16: Example of a constrained random walk with $w(T) = 0$; by using such sample paths as our Wiener process, we can enforce that our inputs have low discrepancy.

method. Our interest, however, is in another extension of the standard method known as Multilevel Monte Carlo (MLMC), which instead exploits our ability to run simulations at different grid levels [Giles, 2006, 2015].

The reason for our choice of MLMC over QMC is that, in coupling our shallow water system with a weather generator, for each simulation we may compute only a small number of random paths and thus there is minimal speed up to be gained by choosing our sequence of paths to have low-discrepancy. If we instead consider the sequence of paths over all simulations, we see that the computational speed up will be dependent upon how many sample paths we generate in total; if this number is very small, the reduction in computational cost will be limited. For example, if we are modelling a system with a low storm generation rate, we may not see enough reduction in the computational cost from using the Quasi Monte Carlo method to balance the increase in cost from the additional computations needed to generate our low-discrepancy sequence.

General stochastic problem

We begin by considering the general problem of approximating numerically the process

$$\{X(t) : t \in [0, T]\} \tag{5.4.2.1}$$

which is modelled as a stochastic equation

$$dX(t) = a(X(t), t)dt + b(X(t), t)dW_t. \tag{5.4.2.2}$$

For a given sample path ω, the solution at time T is given by $X(T, \omega)$, which we can approximate numerically using the Euler-Maruyama method as

$$Y_M \approx X(T, \omega), \tag{5.4.2.3}$$

where the time points $t_m = m\Delta t$ are assumed to be equidistant with $\Delta t = {}^{T}/_{M}$. We generate N independent samples Y_M^i for $i = 1, \ldots, N$, and approximate the expectation $\mathbb{E}[X(T)]$ by the Monte Carlo estimator

$$\mu_{\text{MC}} = \frac{1}{N} \sum_{i=1}^{N} Y_M^i \tag{5.4.2.4}$$

which has computational cost $\mathrm{O}\left(\varepsilon^{-3}\right)$.

For the rest of this chapter, we will make a slight adjustment to the notation and denote the time step as

$$\Delta t_l = TK^{-l} \tag{5.4.2.5}$$

for mesh-refinement parameter $K \in \{2, 3, \ldots\}$; for ease, we will typically take $K = 2$. The variable l will be referred to as the grid level the simulation is being run at, with corresponding time step Δt_l; as we increase the grid level, the time-step will decrease.

To motivate the Multilevel Monte Carlo method, consider the following two situations:

(1) sampling our equation on a fine grid (i.e. large l)

(2) sampling on a coarse grid (i.e. small l)

For the samples on the fine grid, given that each sample is reasonably accurate but quite expensive to run, it makes sense to run only a small number of samples at this level. On the other hand, since the samples on the coarse grid are more inaccurate, it makes sense to run a larger number of samples at this level, which we can get away since they are cheap computationally.

The multilevel approach is to determine the number of simulations to run on a succession of levels (up to a final level L) in such a way that when we combine all our sample runs in a single estimator, we maintain the same desired accuracy but achieve a lower computational cost. We consider a hierarchy of grid levels $l = 0, \ldots, L$ with time step Δt_l and define our numerical approximation to $X(T)$ on level l as P_l. We can then approximate the expectation on the finest grid level L by the telescoping sum

$$\mathbb{E}[P_L] = \mathbb{E}[P_0] + \sum_{l=1}^{L} \mathbb{E}[P_l - P_{l-1}]. \tag{5.4.2.6}$$

Here, we define the expectation on the finest level L as the expectation on the coarsest level $l = 0$ plus a sum of corrections, which are each the difference between two approximations to $X(T)$: one with time step Δt_l (the fine step) and the other with Δt_{l-1} (the coarse step). Each component in (5.4.2.6) is estimated separately:

$$\begin{aligned} \mathbb{E}[P_0] \approx \mu_0 &= \frac{1}{N_0} \sum_{i=1}^{N_0} P_0^i \quad \text{using } N_0 \text{ samples of } P_0 \\ \mathbb{E}[P_l - P_{l-1}] \approx \mu_l &= \frac{1}{N_l} \sum_{i=1}^{N_l} \left(P_l^i - P_{l-1}^i\right) \quad \text{for } l = 1, \ldots, L \end{aligned} \tag{5.4.2.7}$$

To ensure that $\left(P_l^i - P_{l-1}^i\right)$ is reasonably small, we compute these increments using the same Brownian sample path ω_i. Incorporating this point into our notation, our approximation of $\mathbb{E}[X(T)]$ is given by the *multilevel* estimator

$$\mu_{\text{MLMC}} = \sum_{l=0}^{L} \mu_l = \frac{1}{N_0} \sum_{i=1}^{N_0} P_0^0(\omega_i) + \sum_{l=1}^{L} \left[\frac{1}{N_l} \sum_{i=1}^{N_l} \left(P_l^l(\omega_i) - P_{l-1}^l(\omega_i) \right) \right] \tag{5.4.2.8}$$

where the superscript indicates that the sample path ω_i is generated at that level; for $P_{l-1}^l(\omega_i)$, the sample path ω_i will therefore need to be extrapolated to grid level $l-1$. We note that μ_{MLMC} is more efficient than the standard estimator μ_{MC}.

We approximate the error between the expectation of the true solution and our multilevel estimator by

$$\mathbb{E}[X(T)] - \mu_{\text{MLMC}} = \underbrace{\left(\mathbb{E}[X(T)] - \mathbb{E}[P_L]\right)}_{\text{weak discretisation error}} + \underbrace{\left(\mathbb{E}[P_L] - \mu_{\text{MLMC}}\right)}_{\text{MLMC error}}. \tag{5.4.2.9}$$

The error in estimating $\mathbb{E}[P_l - P_{l-1}]$ by μ_l will be proportional to the standard deviation of $(P_l - P_{l-1})$, and since the numerical approximation P_l converges to $X(T)$, the standard deviation of $(P_l - P_{l-1})$ decreases as the grid level l increases (and the time step Δt_l decreases). Thus, fewer samples N_l are needed to compute the estimator μ_l for increasing grid level.

To ensure that $\Delta t_L = {}^{T}/_{K^{-L}} \leq {}^{\varepsilon}/_{2}$ and achieve a weak discretisation error of $\mathrm{O}(\varepsilon)$, we set

$$L = \left\lceil \frac{\log({}^{2T}/_{\varepsilon})}{\log(K)} \right\rceil. \tag{5.4.2.10}$$

The MLMC error is guaranteed to be $\mathrm{O}(\varepsilon)$ by virtue of the following three lemmas [Lord et al., 2014].

Lemma. *For a general stochastic differential equation*

$$dX(t) = a(X(t), t)dt + b(X(t), t)dW_t \quad \textit{for } t \in [0, T] \tag{5.4.2.11}$$

let the drift and diffusion functions $a(X(t), t)$ and $b(X(t), t)$, respectively, be Lipschitz continuous with linear growth, twice continuously differentiable, and have uniformly bounded second derivatives. Consider the multilevel estimator, (5.4.2.8), of $\mathbb{E}[X(T)]$; if the number of samples

$$\begin{aligned} N_0 &= \left\lceil \varepsilon^{-2} \right\rceil \\ N_l &= \left\lceil \varepsilon^{-2} L \Delta t_l \right\rceil \textit{ for } l = 1, \ldots, L \end{aligned} \tag{5.4.2.12}$$

then $\mathrm{Var}(\mu_{\text{MLMC}}) = \mathrm{O}(\varepsilon^2)$.

Lemma. *If $N_0 = \lceil \varepsilon^{-2} \rceil$, $N_l = \lceil \varepsilon^{-2} L \Delta t_l \rceil$ for $l = 1, \ldots, L$ with L defined as in (5.4.2.10), then the computational cost of finding the multilevel estimator is*

$$\mathrm{cost}(\mu_{\text{MLMC}}) = \mathrm{O}\left(\varepsilon^{-2} |\log \varepsilon|^2\right). \tag{5.4.2.13}$$

Lemma. *For a fixed computational cost C, $\exists K_C > 0$ such that $\mathrm{Var}(\mu_{\text{MLMC}})$ is minimised by taking*

$$\begin{aligned} N_0 &= \left\lceil K_C \sqrt{V_0 \Delta t_0} \right\rceil \\ N_l &= \left\lceil K_C \sqrt{\frac{V_l \Delta t_l}{1 + K^{-1}}} \right\rceil \end{aligned} \tag{5.4.2.14}$$

where

$$V_l = \begin{cases} \mathrm{Var}(P_0) & \text{if } l = 0 \\ \mathrm{Var}(P_l - P_{l-1}) & \text{if } l = 1, \ldots, L \end{cases}. \tag{5.4.2.15}$$

To achieve $\mathrm{Var}(\mu_{\mathrm{MLMC}}) = \varepsilon^2/2$, *we set*

$$K_C = 2\varepsilon^{-2} \left(\sqrt{V_0 \Delta t_0^{-1}} + \sum_{l=1}^{L} \sqrt{V_l \Delta t_l^{-1} \left(1 + K^{-1}\right)} \right). \tag{5.4.2.16}$$

We provide a simplified version of the multilevel approach in Algorithm 5.2. For testing the convergence of our method, we assume our method has converged if the error is less than

$$\frac{\varepsilon \left(2^{\gamma} - 1\right)}{\sqrt{2}} \tag{5.4.2.17}$$

where γ is the rate of convergence of the error (i.e. $\mathbb{E}[P_l - P_{l-1}] \propto 2^{-\gamma l}$), which in general we will have to estimate. However, rather than considering just the error for the finest level L, we consider the maximum error over the previous three levels:

$$\max \left\{ \left| \mathbb{E}[P_{L-2} - P_{L-3}] \right|, \left| \mathbb{E}[P_{L-1} - P_{L-2}] \right|, \left| \mathbb{E}[P_L - P_{L-1}] \right| \right\}. \tag{5.4.2.18}$$

This choice of convergence criteria ensures that we continue our simulations until we see true convergence of the method rather than just at a single level. If no such convergence is achieved, then we iterate the maximum level L and repeat; since the error we are testing for will decrease as the level l increases, we expect to see an improvement in our convergence each time we iterate.

Shallow water system with stochastic precipitation

We saw above how the Multilevel Monte Carlo method can be used to estimate more efficiently the expectation of the value of a given stochastic process X at final time T. We would like to consider now how this method can be applied to our specific problem: modelling the shallow water system with stochastic precipitation.

We determined in §5.3 that for our shallow-water/precipitation system, the appropriate quantity of interest to consider was the average maximum water height, $h_{\max}$, and we defined our shallow water Monte Carlo estimator as

$$\mathbb{E}[h_{\max}] \approx \mu_{\text{SW-MC}} = \frac{1}{N} \sum_{k=1}^{N} M_k. \tag{5.4.2.19}$$

A significant departure from the general stochastic approach we outlined above is that the time-step for our shallow water system is determined through the CFL condition

$$\Delta t = \mathrm{CFL} \cdot \frac{\Delta x}{\max\left(|u| + \sqrt{2\,\mathrm{g}\,h}\right)}, \quad \mathrm{CFL} \in (0, 1] \tag{5.4.2.20}$$

with given grid size Δx. Since this condition is included to ensure stability of the shallow water model, it is preferable that it be maintained; the adjustment we

Algorithm 5.2 Multilevel Monte Carlo algorithm

```
function MLMC
    L = 2
    K = 2

    while no convergence do          % continue until convergence
        initial = 100                % consider initial 100 samples

        for j = 1 : initial do
            calculate samples on coarsest level
        end for

        for l = 1 : L do
            for j = 1 : initial do
                calculate samples on remaining levels
                calculate difference estimator P_l − P_{l−1}
            end for
        end for
        calculate mean and variance for each level l

        for l = 0 : L do
            calculate optimal number of samples N(l)
        end for

        for j = 1 : N(0) − initial do
            calculate extra samples on coarsest level
        end for

        for l = 1 : L do
            for j = 1 : N(l) − initial do
                calculate extra samples on remaining levels
                calculate difference estimator P_l − P_{l−1}
            end for
        end for
        update mean and variance on each level l with the new samples

        if convergence has been achieved then
            end while loop
        else
            iterate L and repeat
        end if
    end while

    for l = 1 : L + 1 do
        sum together estimators
    end for
    return final estimator

end function
```

make, therefore, is to instead consider our hierarchy of grids on the spatial domain $x \in [0, D]$, and thus define the grid size on each level $l = 0, \ldots, L$ as

$$\Delta x_l = DK^{-l} \quad \text{for some } K \in \{2, 3, \ldots\}. \tag{5.4.2.21}$$

As before, we define our quantity of interest

$$M_k = \max_{i,n} h(x_i, t_n) \tag{5.4.2.22}$$

on level l with grid size Δx_l by P_l^k. For the general problem, we used the fact that the expectation on the finest level could be approximated as

$$\mathbb{E}[P_L] = \mathbb{E}[P_0] + \sum_{l=1}^{L} \mathbb{E}[P_l - P_{l-1}]. \tag{5.4.2.23}$$

i.e., the expectation on the coarsest level plus a sum of corrections, the difference between an approximation with time-step Δt_l and an approximation with Δt_{l-1}. We use a similar approach here, defining the estimators as

$$\begin{aligned} \mu_0 &= \frac{1}{N_0} \sum_{k=1}^{N_0} P_0^k \quad \text{using } N_0 \text{ samples of } P_0 \\ \mu_l &= \frac{1}{N_l} \sum_{k=1}^{N_l} \left(P_l^k - P_{l-1}^k\right) \quad \text{for } l = 1, \ldots, L \end{aligned} \tag{5.4.2.24}$$

As before, we ensure that $\left(P_l^k - P_{l-1}^k\right)$ is reasonably small by using the same sequence of storm cells and sample paths $\{\Omega, \omega\}$ to determine our stochastic precipitation; in practice, this works as follows:

(1) generate storm cells Ω_j on the finer grid level l

(2) for each storm cell, generate a sample path ω_j on grid level l

(3) calculate the precipitation term S which acts as the source term in the shallow water equations

(4) run the shallow water simulation and calculate P_l

(5) extrapolate Ω_j and ω_j to the coarser level $l - 1$

(6) calculate the precipitation S on the coarser level, use this as the input for the shallow water system, and calculate P_{l-1}

Our shallow water multilevel estimator is thus given by

$$\mu_{\text{SW-MLMC}} = \frac{1}{N_0} \sum_{k=1}^{N_0} P_0^0\{\Omega, \omega\}_k + \sum_{l=1}^{L} \left[\frac{1}{N_l} \sum_{k=1}^{N_l} \left(P_l^l\{\Omega, \omega\}_k - P_{l-1}^l\{\Omega, \omega\}_k\right) \right],$$

where the superscript indicates that the sequence of storm cells and sample paths $\{\Omega, \omega\}_k$ is generated at that level. The error between the expectation of the "true" solution and our multilevel estimator will be

$$\mathbb{E}[h_{\max}] - \mu_{\text{SW-MLMC}} = \underbrace{\left(\mathbb{E}[h_{\max}] - \mathbb{E}[P_L]\right)}_{\text{weak discretisation error}} + \underbrace{\left(\mathbb{E}[P_L] - \mu_{\text{SW-MLMC}}\right)}_{\text{MLMC error}}. \tag{5.4.2.25}$$

We can ensure a weak discretisation error of $\mathrm{O}(\varepsilon)$ by adapting definition (5.4.2.10) as

$$L = \left\lceil \frac{\log(^{2D}/_{\varepsilon})}{\log(K)} \right\rceil. \tag{5.4.2.26}$$

To achieve an MLMC error of $\mathrm{O}(\varepsilon)$, we need to show that our stochastic precipitation equation

$$dS(x,t,s) = \sum_{j=1}^{J} \mathbb{I}_{\Omega_j} \left(a(s)dt + b(x,t)dW_t^{(j)} \right) \tag{5.4.2.27}$$

satisfies the requirements of the first lemma, specifically that the drift and diffusion functions are:

- Lipschitz continuous with linear growth,
- twice continuously differentiable,
- have uniformly bounded second derivatives.

Since we did not specify a particular form for the diffusion intensity $b(x,t)$, we can assume that this function is chosen in such a way that the requirements of the lemma. For the drift function

$$a(s) = \frac{1}{\lambda}\left[\left(\frac{r_{\max} - r_{\min}}{2} \right) \cos\left(\frac{2\pi\,(s - s_{\max})}{366} \right) + \left(\frac{r_{\max} + r_{\min}}{2} \right) \right] \tag{5.4.2.28}$$

we note that the second derivative of the function $f(s) = \cos(s)$ is $f''(s) = -\cos(s)$ which is bounded from above and below by 1 and -1, respectively, and thus $a(s)$ will also have bounded second derivatives; all we have left to show, therefore, is that $a(s)$ is Lipschitz continuous with linear growth, which we will achieve by again considering the function $\cos(s)$.

A function $f(x)$ is Lipschitz continuous if there exists a constant $K > 0$ such that

$$|f(x_1) - f(x_2)| \leq K|x_1 - x_2|, \quad \forall\ x_1, x_2 \tag{5.4.2.29}$$

From the Mean Value Theorem, if a function $f(x)$ is continuous on the interval $[a,b]$ and differentiable on (a,b), then there exists $c \in (a,b)$ such that

$$f(b) - f(a) = f'(c)(b-a) \tag{5.4.2.30}$$

Taking $f(x) = \cos(x)$, we have that

$$|\cos(x_1) - \cos(x_2)| = \underbrace{|-\sin(c)|}_{\leq 1} |x_1 - x_2| \leq |x_1 - x_2| \tag{5.4.2.31}$$

and hence we have Lipschitz continuity. For linear growth, we want to show that the values of the function are bounded as

$$|f(x)| \leq c_1 + c_2|x| \tag{5.4.2.32}$$

for positive constants c_1 and c_2. Taking $x_2 = 0$ in (5.4.2.31) and adding 1 to both sides, we get

$$|\cos(x_1) - 1| + 1 \leq 1 + |x_1|; \tag{5.4.2.33}$$

From the triangle inequality, we note that

$$|\cos(x_1)| \leq |\cos(x_1) - 1| + 1, \tag{5.4.2.34}$$

and hence we can derive the following bound on our function

$$|\cos(x_1)| \leq 1 + |x_1|, \tag{5.4.2.35}$$

and thus we also have the required linear growth. Since the requirements of the lemma are satisfied, we can conclude that by picking the number of samples on each level as

$$\begin{aligned} N_0 &= \lceil \varepsilon^{-2} \rceil \\ N_l &= \lceil \varepsilon^{-2} D \Delta x_l \rceil \text{ for } l = 1, \ldots, L \end{aligned} \tag{5.4.2.36}$$

then the variance and cost of the shallow water multilevel are given by, respectively,

$$\begin{aligned} \text{Var}(\mu_{\text{SW-MLMC}}) &= \text{O}\left(\varepsilon^2\right) \\ \text{cost}(\mu_{\text{SW-MLMC}}) &= \text{O}\left(\varepsilon^{-2} |\log \varepsilon|^2\right). \end{aligned} \tag{5.4.2.37}$$

5.4.3 Numerical tests

Thus far, we have demonstrated in Chapter 3 how we can include precipitation and infiltration effects in our shallow water system and shown in Chapter 4 that this system can be modelled numerically with a kinetic scheme. In this chapter, we have demonstrated that the precipitation can be modelled as a stochastic equation which accounts for observation data, and also considered how the Multilevel Monte Carlo method can be applied to our coupled shallow water/precipitation system. We present in Figure 5.17 a flowchart detailing how these processes interact with one another.

Our aim now is to run several numerical simulations of the coupled system, showing in particular that we can get good convergence of the maximum water height from our multilevel code and the desired reduction in the number of samples to be ran at each level. We also run a standard Monte Carlo method for an increasing number of samples, and compare the computation time against our multilevel method.

We consider a river spanning spatial domain $x \in [0, 1]$ and time domain $t \in [0, 8]$, with topography $Z(x) = 0.1$ and CFL number 0.95. We assume periodic boundary conditions and assume a constant initial height and discharge of

$$h(x, 0) = 1.0, \quad q(x, 0) = 0.0 \qquad \forall x \in [0, 1] \tag{5.4.3.1}$$

We present a diagram of these conditions in Figure 5.18.

For the rainfall, we use a weather generator with the following parameters:

- storms arrive at rate $\beta = 0.25$, i.e. a storm arrives on average every 4s
- the duration of each storm is exponential with rate $\nu = 0.5$, i.e. each storm lasts 2s on average

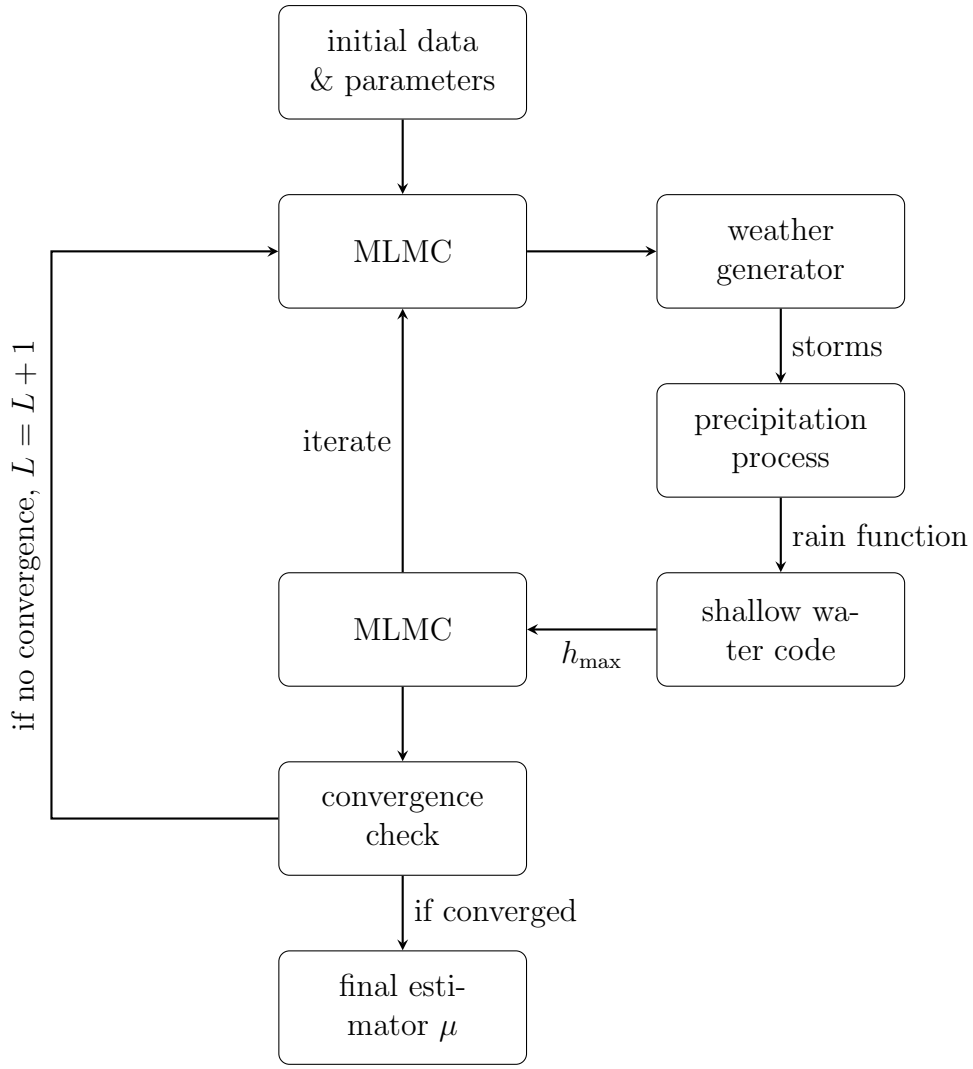

Figure 5.17: Simplified flow diagram for the application of MLMC to a coupled shallow-water/precipitation system.

To check that our stochastic processes are correct, we will output the average number of storms generated for each simulation and the average length of each storm; our expectation is that both of these values should equal 2 (noting that our final time $T = 8$, and hence we would expect 2 storms to have arrived in that time). For our multilevel inputs, we will assume an initial maximum level $L = 2$ and run 100 samples to begin with to get an initial estimate for our mean and variance. For our convergence error, we will take $\varepsilon = 0.0001$.

The outputs of our simulation will be:

- the maximum level L achieved at convergence
- the total computation time (in seconds)
- the final estimator μ_{MLMC} of our maximum water height
- the number of samples $N[0]$ and $N[L]$ computed when convergence is reached
- the average number of storms arrivals for each simulation

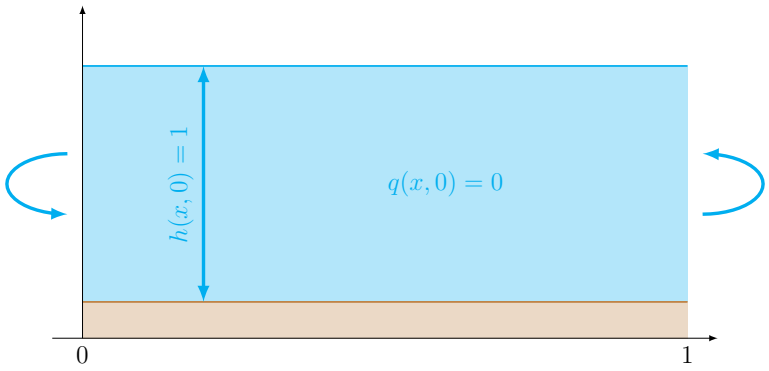

Figure 5.18: Diagram of the river conditions we are considering for our numerical simulations.

- the average duration of each storm for each simulation
- the average time the maximum water height was achieved for each simulation
- the range of times for which the maximum water height was achieved

Running this numerical test three times for the same inputs, we get the results shown in Table 5.4 and the times for the maximum water height shown in Figure 5.19.

Table 5.4: Simulation outputs from applying our multilevel method to the coupled shallow-water/precipitation system.

Outputs	**Simulation** 1	**Simulation** 2	**Simulation** 3
Maximum level L	6	8	8
Computation time (s)	84.63	217.75	263.12
Final estimator μ	2.12	1.86	1.91
$N[0]$	16735	18738	21123
$N[L]$	37	9	15
Average number of storms	1.96	2.15	1.91
Average storm duration	1.78	1.85	2.00

The results from these tests show good comparison with one another; the final estimator for each test is reasonably similar (at around double the initial water height), and the expected reduction in samples to be run at each level is also seen. We note that the results for $N[L]$ are all below the initial samples we run to calculate our mean and variance, thus suggesting we could have taken a lower value to reduce

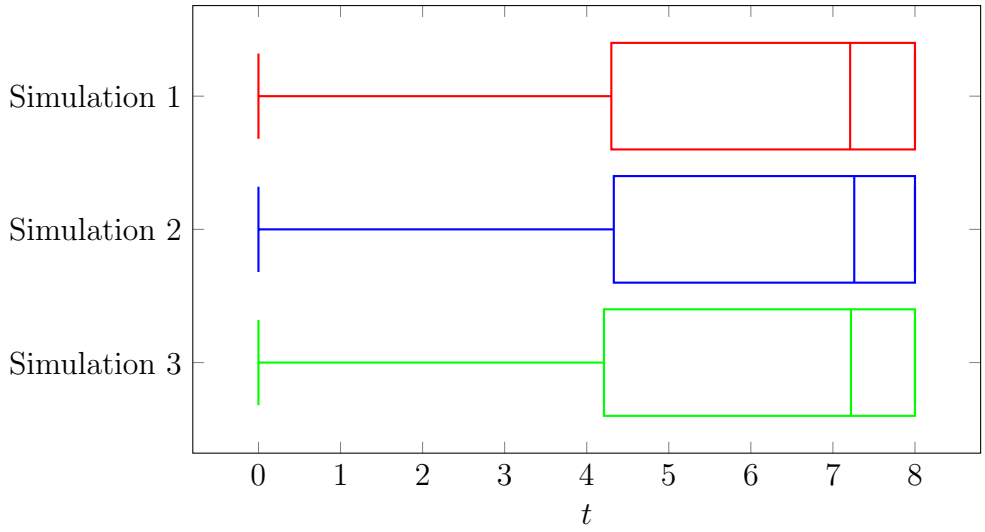

Figure 5.19: Boxplot of the times at which the maximum water height was achieved for each of the three simulations.

the computational cost further. This would, however, have the knock on effect of reducing the number of samples we are using to compute $N[l]$ to begin with, and thus any gain in cost may be balanced here.

The area where we saw the greatest difference in the outputs was in the maximum level L at which convergence was achieved and the total computation time. The first simulation seems to be an outlier in this regard, as a maximum level of $L = 6$ was only needed, compared to $L = 8$ for the other two simulations. This resulted in a large difference in the computational time to run the tests, with the second and third simulations taking around three times as long to run.

As we noted above, to check the outputs from the stochastic processes of our weather generator were correct, we measured the average number of storms and average storm duration for each simulation. The average number of storms was exactly as expected (an average of 2.01), but the average duration was somewhat lower at 1.88. This is most likely due to the fact that we are only simulating up to a final time T, and thus if the duration of a storm would go beyond this point it is reduced, and thus we get a slightly lower average than expected.

The boxplots for the times at which the maximum water height was achieved are consistent across all three simulations, with a minimum of $t = 0$ (which occurs when no storms are generated), a lower quartile of $t = [4.30, 4.33, 4.21]$, a median of $t = [7.21, 7.26, 7.22]$ and an upper quartile/maximum of $t = 8$. These results demonstrate the validity of considering the maximum water height across all times and not just at the final time T (in this case 8s); while a large number of these times were at the final time (from the data, around 40% occurred at the final time), a quarter occurred at a time less than ≈ 4.25s. From a modelling perspective, high flood waves typically cause the most damage, and so underestimating the maximum water height or overestimating the time this will occur could lead to significant miscalculations of the expected damage.

We now consider how the computation time for our Multilevel Monte Carlo compares

to a standard Monte Carlo method. We used the same conditions as above, and ran our simulations on an equivalent $L = 8$ mesh for a varying number of samples. The computation time and final estimator is shown below in Table 5.5.

Table 5.5: Simulation outputs from applying a standard Monte Carlo method to the coupled shallow-water/precipitation system.

Samples	**Computation time (s)**	**Final estimator μ**
100	40.35	2.8
1000	271.44	2.3
10000	2819.99	1.98
100000	25319.10	1.91

For 100 samples we see a reduction in the computation time, as we would expect given we used an initial 100 samples in our multilevel code, but the final estimator is quite a lot higher than for our previous simulations. The computation time for 1000 samples is comparative, but again the final estimator appears to be much higher. The results for 10000 and 100000 are in the range we saw for our multilevel method, but the computation time is significantly higher, at around 100 times as long for the final set of samples. This demonstrates the speed up we can achieve by using the multilevel, and thus motivates its usage in modelling flooding: we can achieve the same accuracy in our solution in significantly faster times using the multilevel method than using the standard Monte Carlo.

5.5 Conclusion

Our first aim in this chapter was to consider how we could formulate the precipitation term in our shallow water model as a stochastic process, enabling us to more accurately reflect the random interactions that we could not otherwise capture deterministically. The approach we took was to first consider a very simple formulation, (5.2.1.1), defining the precipitation as pure white noise, and then progressively improve upon this formulation, (5.2.1.4) and (5.2.1.6), to address certain deficiencies in each approach. The final formulation we derived, (5.2.2.1) and (5.2.2.2), represents the precipitation as a sum of distinct rain cells, whose intensity is given by a drift term derived from observation data and a diffusion term represented as a Wiener process.

The second aim was to consider how we could numerically simulate the extended shallow water system coupled with the stochastic precipitation; our particular focus was on how we could reduce the computational cost, thereby enabling multiple simulations (which would be required for an accurate solution) to be run in a reasonable time frame. The approach we settled upon was the Multilevel Monte Carlo method, and we demonstrated analytically that this method could be applied to our coupled system. We also ran several numerical tests to show the applicability of the method to modelling the coupled shallow-water/precipitation system and its comparative performance to the standard Monte Carlo, and presented an analysis of the results of these simulations.

Chapter 6

Conclusion

At the beginning of this research, we asked ourselves the following question: *how can we better model flood inundation caused by precipitation?* This question was motivated in part by a recent increase in extreme flood events in a number of countries, including Australia, Malaysia, and the United Kingdom, and concerns that, with such extreme events predicted to occur more regularly due to climate change, existing flood defence expenditure levels would not be able to manage.

In researching this problem, we endeavoured to break the problem of rain-induced flood modelling into three separate components:

(1) developing a mathematically rigorous model for the water-body flow and its interactions with precipitation and infiltration phenomena

(2) modelling the precipitation phenomena itself and capturing the stochastic behaviour that it exhibits

(3) developing a numerical simulation approach that would enable accurate results to be generated at a reasonable computational cost

One of the overarching themes within the research was ensuring the models developed could be applied to real world problems, and thus ensuring that the assumptions we make are consistent with the physical reality we wish to model. A number of approaches had been proposed in the past and were being used for industrial applications, but the methodology used in developing these techniques sometimes lacked mathematical rigour or were too general to be applied to real world problems. Our desire, therefore, was to demonstrate how mathematical rigour could be ensured by going back to the original problem, or by improving existing approaches to reflect the real-world more accurately.

6.1 Developing a shallow water model

The first topic we considered in Chapter 3 was how to improve the mathematical rigour of modelling the interaction between a water-body (such as a river) and the precipitation and infiltration phenomena. The most commonly used method for modelling water-body flow was through the shallow water equations, and existing

approaches such as Delestre et al. [2012] had adapted these equations directly to account for the meteorological phenomena.

As the shallow water system is derived as a reduction of the Navier-Stokes equations, the approach we decided to take was to go back to the original equations and adapt the boundary conditions there instead of including them after the shallow water system had been derived. This would ensure that the effect of including these additional terms would be carried through in the derivation, and thus capture additional terms that might arise that could otherwise be missed.

The approach we took in §3.1 was to incorporate the meteorological phenomena directly into the boundary conditions, leading to

$$\begin{aligned} (\boldsymbol{\sigma}[\boldsymbol{u}]\, n_\Omega) \cdot t_\Omega &= -\rho_0 \left(k(\boldsymbol{u}) - k_I\right) \boldsymbol{u} \cdot t_\Omega \\ \boldsymbol{u} \cdot n_\Omega &= I(x,t,h(x,t)) \end{aligned} \tag{6.1.0.1}$$

on the wet boundary $\mathcal{B}$, and

$$\begin{aligned} (\boldsymbol{\sigma}[\boldsymbol{u}]\, n_\Omega) \cdot t_\Omega &= -\rho_0 k_R \boldsymbol{u} \cdot t_\Omega \\ \boldsymbol{u} \cdot n_\Omega &= \frac{\partial_t H - R}{\sqrt{1 + |\partial_x H|^2}} \end{aligned} \tag{6.1.0.2}$$

on the free surface $\mathcal{F}$. The friction terms k_I and k_R in the Navier boundary condition and stress condition, respectively, model the interaction between the water droplets of the rain or water recharging from the ground and the water-body itself, and their inclusion ensures our system does not lead to non-physical solutions.

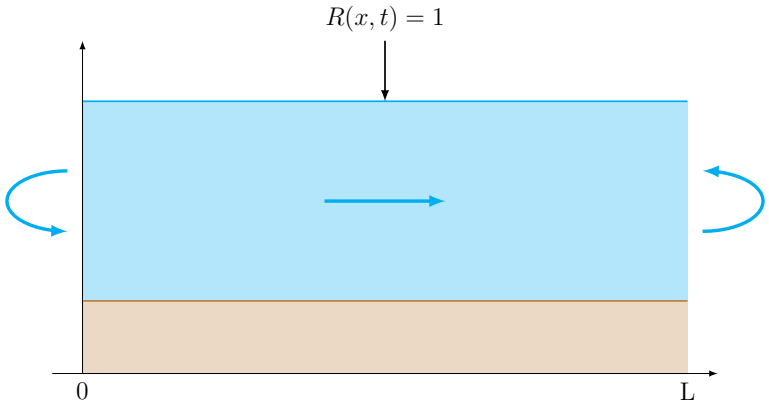

Figure 6.1: The inclusion of the friction terms ensures our system does not lead to non-physical solutions, such as when modelling a simple water-body flow with precipitation and periodic boundary conditions.

Applying a vertical averaging approach leads to the extended shallow water system

$$\begin{aligned} \partial_t h + \partial_x q &= S \\ \partial_t q + \partial_x \left[\frac{q^2}{h} + \mathrm{g}\,\frac{h^2}{2}\right] &= -\,\mathrm{g}\, h \partial_x Z + S\frac{q}{h} - \left(k_R - k_I + k_0\left(\frac{q}{h}\right)\right)\frac{q}{h}. \end{aligned} \tag{6.1.0.3}$$

The usual approach to numerical modelling of fluid flow is to use either a finite difference or finite volume method. A limitation of these methods is their inability

to preserve the *filling the lake* state, defined as

$$\partial_t h = R \text{ and } u = 0, \tag{6.1.0.4}$$

an adaptation of the standard *lake at rest* to reflect that our extended shallow water system is now a balance law instead of a conservation law. The approach we took instead in §4.1 was to consider a kinetic interpretation of the system, representing the system in terms of a *kinetic averaging weight function* χ and a *kinetic density function* M. Using the kinetic approach, in §4.2 we rewrote our shallow water system into a single *kinetic equation* given by

$$\partial_t M + \xi \partial_x M - \mathrm{g}\, \partial_x \hat{W} \partial_\xi M + \frac{SM}{\langle M \rangle_1} = Q \tag{6.1.0.5}$$

which we then solve using a finite volume approach:

$$U_i^{n+1} = U_i^n - \frac{\Delta t}{\Delta x} \left(F_{i+1/2}^n - F_{i-1/2}^n \right) + \Delta t \begin{bmatrix} S_i^n \\ S_i^n u_i^n \end{bmatrix}. \tag{6.1.0.6}$$

The rationale for doing this is that it is easier to solve the single kinetic equation than the full shallow water system, but in solving this equation we can use the definition of M and χ to retrieve our original variables (h, hu).

We note, however, the limitations of the model we have derived. Though the extended shallow water model goes some way to incorporate real-world phenomena, that it only includes one spatial dimension makes its application to modelling realistic flood inundation limited in scope, particular on very large catchments. Additionally, as we noted in §6.4.1, it is not clear that the kinetic formulation and scheme we have derived for the one-dimensional model can be extended to a second dimension, and thus an entirely new approach may be required.

6.2 Modelling the precipitation stochastically

Having established our extended shallow water system and demonstrated how it could be modelled numerically, we moved on to consider how to model the precipitation term. The decision to model the term as a stochastic process was taken to better capture the random interactions that occur in reality, and that are too complex to be described with a deterministic modelling approach.

The first approach we took in §5.2.1 was to model the precipitation very simply as a pure white noise process. This assumption, however, highlighted that there should be some degree of correlation in the rain intensity across of the grid cells, and so our next approach was to model the precipitation as a single Wiener process, given by

$$dS(x,t) = b(x,t) dW_t. \tag{6.2.0.1}$$

Since for any given sample path the value of a Wiener process at time t_{n+1} is dependent upon the intensity at time t_n, using this representation would give us good correlation between nearby cells.

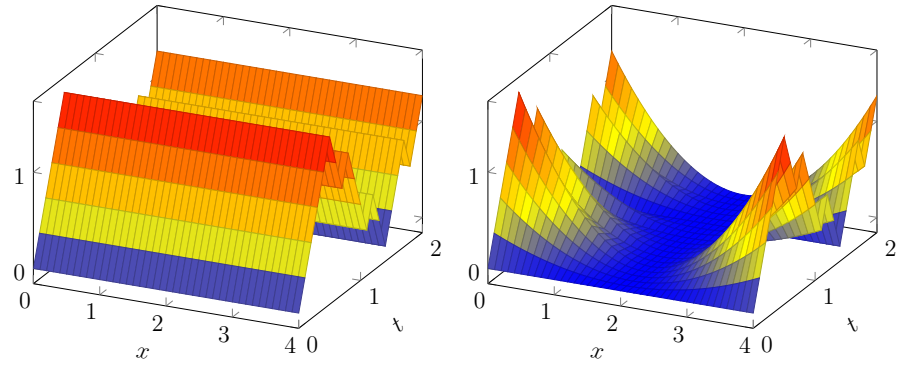

Figure 6.2: Representation of the precipitation, $S(x,t)$, as a Wiener process with both a constant and spatially-variant intensity function $b(x,t)$.

The obvious limitation of using a single Wiener process to model across the entire spatial domain is a lack of spatial variability, other than in the diffusion term $b(x,t)$. To address this issue, we decided to apply the techniques used in weather generators and model the precipitation as a collection of rain-producing storms, with the intensity for each storm given by a different Wiener process. This leads to the sum

$$dS(x,t) = \sum_{j=1}^{J} \mathbb{I}_{\Omega_j} \left(b(x,t) dW_t^{(j)} \right), \tag{6.2.0.2}$$

where $\Omega_j \in \Omega$ are the spatial-temporal domains in which each storm is located. Using this formulation, combining both the Wiener process and the weather generator approach, ensures that both of our desired properties are achieved.

The final improvement we made to our stochastic representation in §5.2.2 was to add a drift term derived from observation data, which we denote very generally by $a(\cdot)$:

$$dS(x,t) = \sum_{j=1}^{J} \mathbb{I}_{\Omega_j} \left(a(\cdot)dt + b(x,t) dW_t^{(j)} \right). \tag{6.2.0.3}$$

Looking at total monthly precipitation data from an example rain gauge with around 60 years of records, it became clear that the individual monthly values were too sporadic to be used to determine the drift term a (though we note that this sporadic nature lends some justification to considering the precipitation as a stochastic process). We cleaned up this data by calculating the average total daily precipitation for each month, and in doing so we were able to determine that the drift term could be approximated as

$$a(s) = \left(\frac{r_{\max} - r_{\min}}{2} \right) \cos \left(\frac{2\pi \left(s - s_{\max} \right)}{366} \right) + \left(\frac{r_{\max} + r_{\min}}{2} \right). \tag{6.2.0.4}$$

This approximation was chosen to ensure we capture the seasonality in the data, and the parameters $r_{\max}$ (the maximum average daily precipitation) and $r_{\min}$ (the minimum average daily precipitation) are taken from the observation data to ensure we get the correct scaling in our approximation.

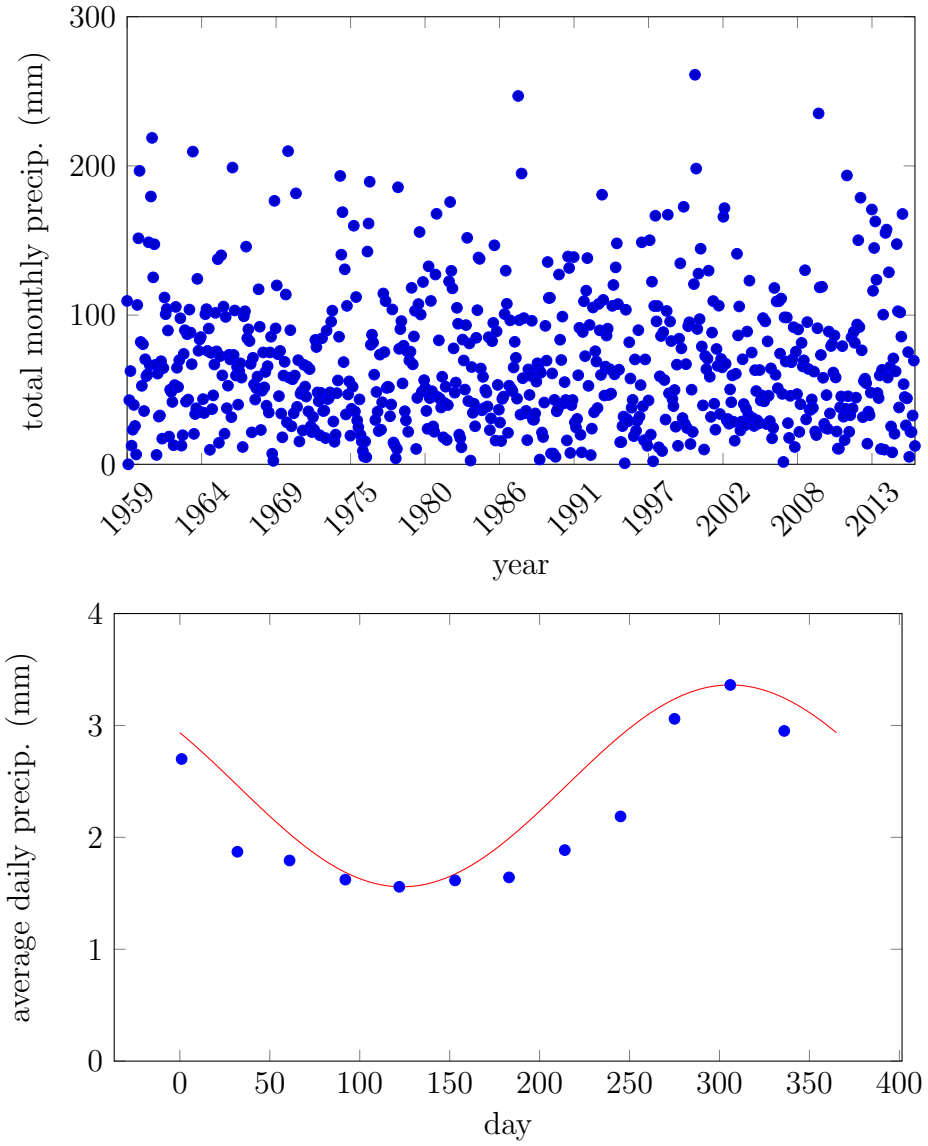

Figure 6.3: Comparison of the full observation data for the example gauge and the approximation, $a(s)$, fitted to the total average daily precipitation.

Our final stochastic precipitation equation with drift term defined from observation data is given by

$$dS(x,t,s) = \sum_{j=1}^{J} \mathbb{I}_{\Omega_j} \left(a(s)dt + b(x,t)dW_t^{(j)} \right)$$

$$a(s) = \frac{1}{\lambda}\left[\left(\frac{r_{\max} - r_{\min}}{2} \right) \cos\left(\frac{2\pi\,(s - s_{\max})}{366} \right) + \left(\frac{r_{\max} + r_{\min}}{2} \right) \right]$$

The incorporation of observation data from weather stations in our stochastic precipitation formulation was intended to ensure it reflected realistic weather patterns and seasonal changes in precipitation rate. This approach does, however, rely on such observation data being available and being of a long enough record to be viable

in determining our drift term. For some countries such data is widely and freely available, but in other locations this may not be so. If this is the case, estimations must instead be made based on expertise (which can be flawed) or data from other locations (which may have very different precipitation patterns). In applying the method we have presented to make policy decisions, consideration must therefore be made on the accuracy and viability of any observation data used.

6.3 Monte Carlo simulations

The final topic we considered in §5.3 was how to simulate the extended shallow water system with stochastic precipitation we had developed. We began by introducing the standard Monte Carlo procedure and demonstrating its application by approximating the integral of a simple equation. This helped to motivate the approach we would need to take for our shallow water system, and in particular determining the quantity of interest we wanted to calculate in the final step.

As our intended application is to modelling flooding, we decided to use the expected maximum water height, which could be estimated by the shallow water Monte Carlo estimator

$$\mathbb{E}[h_{\max}] \approx \mu_{\text{SW-MC}} = \frac{1}{N}\sum_{k=1}^{N} M_k, \tag{6.3.0.1}$$

where $M_k = \max_{i,n} h(x_i, t_n)$, i.e. the maximum water height for a single simulation.

Part of the motivation for our research was to consider how we could maximise the accuracy of our flood model at no additional cost, and so we looked at two improvements upon the standard Monte Carlo method. The first, Quasi Monte Carlo, was introduced briefly with some consideration given to how it could be applied to the sample paths ω_i we use to define our Wiener process. Our primary focus, however, was on the Multilevel Monte Carlo introduced by Giles [2006] and detailed further in Giles [2015]. We adapted the approach presented therein, first to reflect the CFL condition used in the shallow water system by taking the hierarchy of grids on the spatial rather than temporal domain, defining the grid size for each level $l = 0, \ldots, L$ as

$$\Delta x_l = DK^{-l} \quad \text{for some } K \in \{2, 3, \ldots\}, \tag{6.3.0.2}$$

and then defining the shallow water multilevel estimator as

$$\mu_{\text{SW-MLMC}} = \frac{1}{N_0}\sum_{k=1}^{N_0} P_0^0\{\Omega, \omega\}_k + \sum_{l=1}^{L}\left[\frac{1}{N_l}\sum_{k=1}^{N_l}\left(P_l^l\{\Omega, \omega\}_k - P_{l-1}^l\{\Omega, \omega\}_k\right)\right],$$

so as to reflect the weather generator approach we detailed in §5.2.1. The error approximation for the standard Multilevel Monte Carlo method is presented in the form of three lemmas, detailed in [Lord et al., 2014]. For our shallow water system, we demonstrated that the requirements for these lemmas to hold were satisfied by the drift and diffusion functions for our stochastic precipitation, and thus the computational cost for our multilevel estimator is given by

$$\text{cost}(\mu_{\text{SW-MLMC}}) = \text{O}\left(\varepsilon^{-2}|\log\varepsilon|^2\right), \tag{6.3.0.3}$$

as an improvement on the $\mathrm{O}(\varepsilon^{-3})$ cost of the standard Monte Carlo estimator.

Our final step was to run several simulations of our Multilevel Monte Carlo method on the coupled shallow-water/precipitation system. The outputs from the three simulations demonstrated good comparison with one another, with the final estimator for the maximum water height reasonably consistent across all three simulations. The reduction in the number of additional samples to be calculated for each level L was also seen, and we also looked at the statistics of the storms from the weather generator to ensure they were consistent with expectations. We also run a standard Monte Carlo method for our system with increasing number of samples, and analysed the outputs in comparison to our multilevel method; in particular, we saw the expected decrease in computational time for the multilevel method at the same level of accuracy.

We can see from the reduction in computational cost that the Multilevel Monte Carlo method improves upon the standard Monte Carlo, and thus enables us to simulate at a greater accuracy for the same cost of resources. As part of the MLMC approach, however, we made use of the shallow water Monte Carlo estimator (6.3.0.1), which fails to account for the spatial variability in maximum water height, which will be of particular interest in very large catchments. In defining our Monte Carlo approach, we proposed another estimator to address this problem, defined as

$$\mu_{\text{SW-MC}}(x_i) = \frac{1}{N}\sum_{k=1}^{N} M_k(x_i), \tag{6.3.0.4}$$

which is calculated for each grid-point rather than globally. The drawback of using this estimator is that it will significantly increase the number of computations required; if we have 1000 grid points in our domain, we will have to calculate a multilevel estimator for each of these grid points, which may not be computationally feasible. It may be possible to scale this approach back and consider the maximum water height within a certain number of subdomains of the catchment, where certain properties are homogeneous, but determining these subdomains prior to the simulation may not always be easy.

6.4 Extensions and future research

In this section we will consider some extensions of the research we have presented thus far, in particular the extendability of the approach in Chapters 3 and 4 to the two-dimensional shallow water equations, as well as some proposed avenues of future research. In doing so, we will also attempt to address some of the pitfalls that could occur and that will need to be overcome.

6.4.1 Extendability to two-dimensions

We saw above that through a simple adjustment of the boundary conditions of the Navier-Stokes equations, (3.1.1.1) and (3.1.2.1), we can rigorously derive the

one-dimensional extended shallow water system

$$\begin{aligned} \partial_t h + \partial_x [q] &= S \\ \partial_t [q] + \partial_x \left[\frac{q^2}{h} + \frac{\mathrm{g}\, h^2}{2} \right] &= -\mathrm{g}\, h \partial_x Z + S \frac{q}{h} - \left(k_R - k_I + k_0 \left(\frac{q}{h} \right) \right) \frac{q}{h}. \end{aligned} \tag{6.4.1.1}$$

where S is a source term which reflects the net amount of water added to or removed from the flow. We also demonstrated how we can derive a numerical model, (4.2.2.2), using ideas from both finite volumes and kinetic theory, and applied this model to several numerical experiments to demonstrate its viability.

A drawback of having a purely one-dimensional model is that while we can model certain real world problems (primarily when the additional spatial dimension can be ignored), for some problems the spatial complexity is too great for a one-dimensional model to give an accurate enough solution.

In §2.1, we presented two other forms of the shallow water equations without additional source terms: the one-dimensional free surface model given by

$$\begin{aligned} \partial_t A + \partial_x Q &= 0 \\ \partial_t Q + \partial_x \left[\frac{Q^2}{A} + \mathrm{g}\, I_1(x, A) \cos\theta \right] &= -\mathrm{g}\, A \sin\theta + \mathrm{g}\, I_2(x, A) \cos\theta \end{aligned} \tag{6.4.1.2}$$

where the variables of interest are A the wet area and Q the discharge, and the two-dimensional shallow water equations, given by

$$\begin{aligned} \partial_t h + \partial_x [hu] + \partial_y [hv] &= 0 \\ \partial_t [hu] + \partial_x \left[hu^2 + \frac{\mathrm{g}\, h^2}{2} \right] + \partial_y [huv] &= -\mathrm{g}\, h \partial_x Z - k_0 (u)\, u \\ \partial_t [hv] + \partial_x [huv] + \partial_y \left[hv^2 + \frac{\mathrm{g}\, h^2}{2} \right] &= -\mathrm{g}\, h \partial_y Z - k_0 (v)\, v. \end{aligned} \tag{6.4.1.3}$$

with additional spatial axis y and associated velocity v.

For the one-dimensional free surface model, considering just the added source term S we can naturally extend the system in line with our derivation to give

$$\begin{aligned} \partial_t A + \partial_x Q &= S \\ \partial_t Q + \partial_x \left[\frac{Q^2}{A} + \mathrm{g}\, I_1(x, A) \cos\theta \right] &= -\mathrm{g}\, A \sin\theta + \mathrm{g}\, I_2(x, A) \cos\theta + S \frac{Q}{A} \end{aligned} \tag{6.4.1.4}$$

For the two-dimensional shallow water system, this extension is not as trivial: we can see that the inclusion of the additional spatial dimension y does not simply add an extra equation, but also induces additional terms in the existing equations. Therefore, we cannot assume that the right-hand side of the new equation will solely be of the form

$$-\mathrm{g}\, h \partial_y Z + Sv \tag{6.4.1.5}$$

and not include, for instance, momentum effects generated by the rain in the x-spatial dimension, or indeed that our existing equations will also remain unchanged. This also holds for the friction terms k_R and k_I for both the two-dimensional system

and the free surface model, since the manner in which these terms interact with the flow will be different in two-dimensions and depend upon how the extensions to the momentum equations are achieved.

This motivates, therefore, the necessity for any derivation of the model to be mathematically rigorous, and therefore any further research into deriving the two-dimensional model with additional precipitation and infiltration effects should proceed as we considered above - by going back to the Navier-Stokes equations (or Euler equations for the free surface model) and adapting the boundary conditions to incorporate the precipitation and infiltration terms as needed.

Extending these models in this way will enable us to model systems and catchments of much greater complexity: for instance, our extended shallow water model assumes variations in the cross-section of a river can be neglected, but using the extended free surface model, we can account for instances where this no longer holds true and the cross-section is more general. The extended two-dimensional model will also enable us to consider much wider catchments and more accurately model the flood inundation away from the river, extending the level of real-world applications that our model can be applied to.

Kinetic scheme in two-dimensions

For the one-dimensional system we presented above, the development of the kinetic scheme was based on defining a kinetic density function M in terms of the variables h and u, such that when we integrated M against powers of ξ we could get back our desired variables h and $q = hu$. Given the desirable properties of the kinetic approach, it would be beneficial to have a similar numerical method for the two-dimensional system.

In our derivation of the one-dimensional model in Chapter 4, we followed the approach of Audusse et al. [2000], Perthame and Simeoni [2001], and Ersoy [2015]. Extending this approach to the two-dimensional model, the main difficulty will be in determining the correct form of M to ensure we can derive the appropriate macroscopic-microscopic relations.

Assuming that the conservation of mass equation for our two-dimensional shallow water system will be of the form

$$\partial_t h + \partial_x[hu] + \partial_y[hv] \tag{6.4.1.6}$$

if we define a velocity vector $\boldsymbol{w} = [u, v]^\intercal$, we can build the first two macroscopic-microscopic relations as

$$\int_{\mathbb{R}} \begin{bmatrix} 1 \\ \xi \end{bmatrix} M(x,t,\xi) d\xi = \begin{bmatrix} h(x,t) \\ h(x,t)\boldsymbol{w}(x,t) \end{bmatrix} \tag{6.4.1.7}$$

and derive the first part of the kinetic equation as

$$\partial_t M + \xi \nabla_{xy} M. \tag{6.4.1.8}$$

Thus, we can achieve the derivation we require for the two-dimensional system by simply extending the definition of M to include the vector $\boldsymbol{w}$, and this will also

give us the required time derivatives $\partial_t[hu]$ and $\partial_t[hv]$. The difficulty will come in getting the spatial derivatives in the conservation of mass equations, which we can write as the matrix multiplication

$$\begin{bmatrix}\partial_x & \partial_y\end{bmatrix}\begin{bmatrix}hu^2+\frac{g\,h^2}{2} & huv\\ huv & hv^2+\frac{g\,h^2}{2}\end{bmatrix}=\nabla_{xy}\begin{bmatrix}hu^2+\frac{g\,h^2}{2} & huv\\ huv & hv^2+\frac{g\,h^2}{2}\end{bmatrix}. \tag{6.4.1.9}$$

The requirement we need is therefore that

$$\int_{\mathbb{R}}\xi^2 M(x,t,\xi)d\xi=\begin{bmatrix}hu^2+\frac{g\,h^2}{2} & huv\\ huv & hv^2+\frac{g\,h^2}{2}\end{bmatrix}. \tag{6.4.1.10}$$

and there is no obvious extension of the one-dimensional formulation for M that will achieve this. Further research will be required, therefore, to ascertain if such a formulation of M is possible, or whether another approach will be required.

Spatial scales

The vertical averaging approach that we used to reduce the Navier-Stokes equations to the shallow water system in §3.2 relies on the assumption that vertical variations in height and velocity and small compared to the horizontal variations; this was achieved by postulating a *small parameter* ratio

$$\varepsilon:=\frac{D}{L}=\frac{V}{U}\ll 1, \tag{6.4.1.11}$$

where D, L, V, and U are the scales of water height, domain length, vertical fluid velocity, and horizontal fluid velocity, respectively. As we move to two-dimensions, however, this assumption breaks down in a number of cases. If we wish to model the flow in a river, for example, while the vertical variations may be small with respect to the horizontal scale in the direction of the river, they may not be with respect to the scale across the width of the river.

A possible solution, and one that could be explored in more detail in future research, is to model a catchment using both one- and two-dimensional systems: the river is modelled as a single or collection of one-dimensional objects (see Figure 6.4), whilst outside the river system, where vertical variations in water height and velocity will be small with respect to *both* horizontal scales, we can use a two-dimensional model.

This approach would of course present additional complications to be dealt with:

- how to determine beforehand the extent of the river that is modelled one-dimensionally
- how to deal with the boundary between the two models; foe example, determining the velocity of the water as it flows from the river into the catchment, which will be of particular importance in flood modelling
- how to ensure the balance of mass, momentum, and energy is maintained

One of the primary benefits, however, of modelling our catchment in this way is that we will gain in computational cost, since the one-dimensional model will be

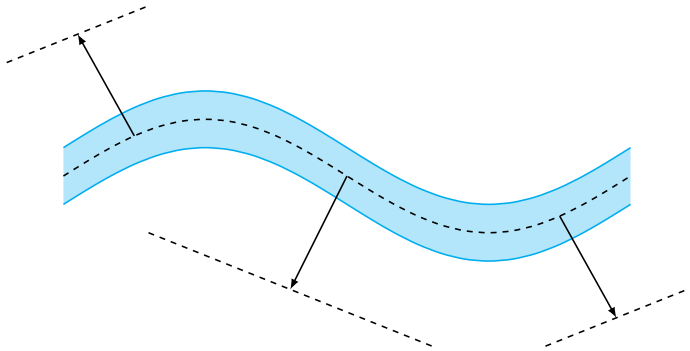

Figure 6.4: We can represent the full two-dimensional river as individual one-dimensional segments.

cheaper to compute, but minimise the loss in accuracy since the areas where we would expect to see the greatest complexity in the solution are modelled using the more accurate two-dimensional model. This also improves the application of our entire coupled model to real-world problems, since we would expect to be modelling on very large catchments where the computational cost will be very high.

6.4.2 Ensuring non-negativity of the rainfall

In §5.2.3, we demonstrated that our stochastic precipitation could be approximated numerically as

$$\begin{cases} Y_{m+1}(x,s) = Y_m(x,s) + \displaystyle\sum_{j=1}^{J} \mathbb{I}_{\Omega_j} \left(a(s)\Delta\tau_{m+1} + b(x,\tau_m)\Delta W_{m+1}^{(j)} \right) \\ \quad Y_0(x,s) = S_0(x,s). \end{cases} \tag{6.4.2.1}$$

Our formulation did not address, however, the issue of ensuring that the rainfall remains non-negative. While we will not go into too much detail here, we would like to give some discussion on how this can be achieved.

In the derivation of our extended shallow water system we presented in Chapter 3, we made explicit the difference between water being added to the system on the free surface (i.e. *rainfall*, denoted by R) and water moving across the wet boundary (i.e. *infiltration*, denoted by I), with the net flow of water being by denoted by $S = R - I$. The reason for considering these separately rather than as a single process is that each interacts with the flow in a different way, most notably the way each process produces friction in contact with the water flow. Therefore, while the net flow of water may become negative, it is important that this only occurs when the infiltration exceeds the rainfall, and not due to the rainfall itself.

In light of this, consider the simplified numerical approximation (5.2.3.5) for a single storm cell; a very simple approach to ensure non-negativity is to redefine our approximation with an intermediate step

$$\tilde{Y}_{m+1}(x,s) = Y_m(x,s) + a(s)\Delta\tau_{m+1} + b(x,\tau_m)\Delta W_{m+1} \tag{6.4.2.2}$$

and then adjust our iteration $Y_{m+1}(x,s)$ depending on the sign of (6.4.2.2) and the boundary conditions we want to use. To determine the best boundary condition to use, we note that any choice we use should have the following properties:

(1) if $\tilde{Y}_{m+1}(x,s) \geq 0$, then we should have that $Y_{m+1}(x,s) = \tilde{Y}_{m+1}(x,s)$

(2) any adjustment we make should reflect the physical reality and underlying mathematical structures of our system

Given these properties, we consider two different boundary conditions for our numerical approximation, which are visualised below in Figure 6.5: a *reflective boundary condition*, with

$$Y_{m+1}(x,s) = \max(\tilde{Y}_{m+1}(x,s), -\tilde{Y}_{m+1}(x,s)) \tag{6.4.2.3}$$

and an *absorbing boundary condition*, with

$$Y_{m+1}(x,s) = \max(\tilde{Y}_{m+1}(x,s), 0). \tag{6.4.2.4}$$

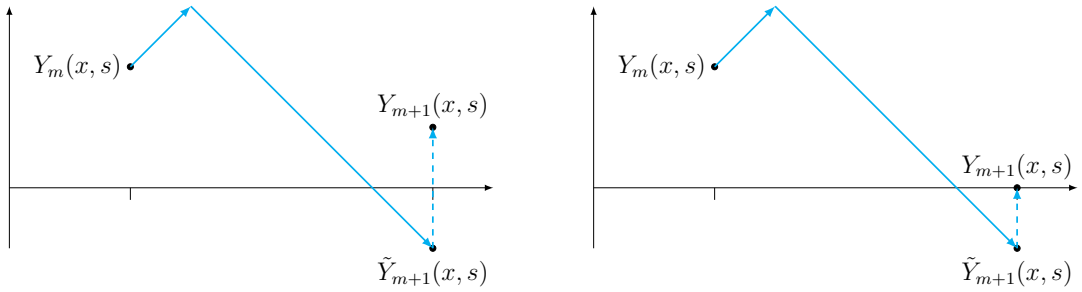

Figure 6.5: We can ensure non-negativity of the stochastic precipitation using either reflective (left) or absorbing (right) boundary conditions.

It is clear that both choices satisfy the first requirement that if $\tilde{Y}_{m+1}(x,s) \geq 0$ then no adjustment is made; deciding which choice is better will therefore rely on the second requirement. Looking at our approximation (5.2.3.5), we note that any reduction in the rainfall will come from the diffusion term $b(x,\tau_m)\Delta W_{m+1}$ since the drift term is by definition positive. The diffusion term represents the random fluctuations that can occur in the rate of precipitation, due to physical reactions between the water molecules are their surroundings. A reduction in the precipitation rate will mean a reduction in the amount of energy contained in the rainfall.

If we were to assume reflective boundary conditions, we would potentially be adjusting a reduction in energy to an increase in energy. On the other hand, if we were to assume absorbing boundary conditions, we would limit the decrease the energy to only the maximum contained in the system. Since we do not want to be adding energy to the system when it should be decreased, we conclude that absorbing boundary conditions are more consistent with the underlying physical and mathematical structures. Our numerical approximation for the single storm cell is therefore given by:

$$\begin{cases} Y_{m+1}(x,s) = \max(\tilde{Y}_{m+1}(x,s), 0) \\ \tilde{Y}_{m+1}(x,s) = Y_m(x,s) + a(s)\Delta\tau_{m+1} + b(x,\tau_m)\Delta W_{m+1} \\ \quad Y_0(x,s) = S_0(x,s). \end{cases} \tag{6.4.2.5}$$

A similar adjustment can be made for the full approximation (6.4.2.1).

6.4.3 Inclusion of infiltration effects

Infiltration plays an important role in the prediction of flood inundation, particularly during cycles of high and low rainfall. If the soil is very unsaturated, a high-intensity rainfall event may not result in flooding, as the water will infiltrate into the ground too quickly for runoff to occur; however, if this is followed by further (even low-intensity) rainfall events, the soil will become too saturated for the water to infiltrate and thus a flood event will occur.

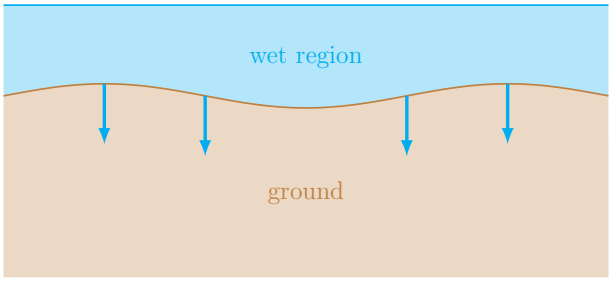

Figure 6.6: Water will infiltrate from the water body into the ground, until the ground becomes completely saturated.

The inclusion of infiltration in our system is therefore an important consideration for future research, but care must be taken in how we model this effect. The motion of water across the boundary between the flow and the ground occurs at a much quicker time scale than the groundwater flow, which itself can have increasing temporal scales as we move to deeper and deeper layers. To ensure we can accurately capture the temporal scale at which each process occurs, it makes sense to consider the system as two components: a model for the amount of water added to or subtracted from the water body, and a model for the motion of water within the ground itself.

For modelling the infiltration effect, there are a number of existing approaches, including Darcy's law [Darcy, 1856], the Richards equation [Richards, 1931], and the Green-Ampt method [Green and Ampt, 1911]. Each of these methods has there advantages and disadvantages: a downside of the Green-Ampt method, for example, is that the depth of water above the ground, h_0, is assumed to be negligible, making it difficult to use the method for modelling a coupled infiltration and shallow water system. A possible solution is to use the Richards equation in general, switching to the more accurate Green-Ampt method when the water depth $h_0 \approx 0$.

The main approach for modelling the flow of groundwater within an aquifer is with the *groundwater flow equation*, in which we perform a mass balance on the water that flows into and out of a small volume of the subsurface:

$$\frac{\partial h}{\partial t} = \alpha \left(\frac{\partial^2 h}{\partial x^2} + \frac{\partial^2 h}{\partial y^2} + \frac{\partial^2 h}{\partial z^2} \right) - \frac{G}{S_s}. \tag{6.4.3.1}$$

This formulation is used by MODFLOW, a numerical model created by the US Geological Survey for modelling groundwater flow [MODFLOW]. Modelling the subsurface flow in three dimensions, however, can be very computationally expensive to compute over a large catchment area. The formulation can be simplified using the *Dupuit-Forchheimer assumption* [Dupuit, 1863, Forchheimer, 1886], whereby we

assume that groundwater only flows in a horizontal direction, and hence

$$\frac{\partial h}{\partial z} = 0. \tag{6.4.3.2}$$

By reducing the dimension of the problem, we can significantly reduce the computational cost required to calculate the groundwater flow, and hence maintain our desired efficiency when coupling this model with our extended shallow water system.

6.5 Moving forward

Within this thesis we have demonstrated how we can derive an extended shallow water model which includes terms reflecting both precipitation and infiltration effects. The precipitation term was modelled as a stochastic equation, defined as a sum of storm cells with their own individual intensities and including a drift term derived from observation data. We then demonstrated how the system could be simulated numerically by adapting the Multilevel Monte Carlo method, which improves upon the efficiency of the standard Monte Carlo method.

$$\partial_t h + \partial_x q = S$$

$$\partial_t q + \partial_x \left[\frac{q^2}{h} + \mathrm{g}\,\frac{h^2}{2}\right] = -\,\mathrm{g}\,h\partial_x Z + S\frac{q}{h} - \left(k_R - k_I + k_0\left(\frac{q}{h}\right)\right)\frac{q}{h}$$

$$dS(x,t,s) = \sum_{j=1}^{J} \mathbb{I}_{\Omega_j}\left(a(s)dt + b(x,t)dW_t^{(j)}\right)$$

$$a(s) = \frac{1}{\lambda}\left[\left(\frac{r_{\max} - r_{\min}}{2}\right)\cos\left(\frac{2\pi\,(s - s_{\max})}{366}\right) + \left(\frac{r_{\max} + r_{\min}}{2}\right)\right]$$

$$\mu_{\mathrm{SW}} = \frac{1}{N_0}\sum_{k=1}^{N_0} P_0^0\{\Omega,\omega\}_k + \sum_{l=1}^{L}\left[\frac{1}{N_l}\sum_{k=1}^{N_l}\left(P_l^l\{\Omega,\omega\}_k - P_{l-1}^l\{\Omega,\omega\}_k\right)\right]$$

Flood modelling is a wide and varied area of research, and which we have only just begun to scratch the surface of in this thesis. What is clear, however, is that flood modelling encompasses more than just the water-body itself; the mathematical derivation that we undertook highlights that any model we develop cannot ignore how the water-body interacts with precipitation and infiltration phenomena. The addition or subtraction of water through these terms affects not only the balance of mass (in this case, the water height h) in the system but also, as we showed rigorously in our derivation, the balance of momentum, and we showed in a number of numerical tests that this addition will directly impact the extent to which the water-body will flood.

The numerical simulation approach we developed was specifically focused on how we can reduce the computational cost of predicting the expected maximum water height

of a flood (or equivalently, how we can get a more accurate expectation for the same computational cost). This was motivated by an increase in the number of extreme flood events in recent years, and predictions for the future that suggest this will only continue. If we are to face the inevitability of more and more extreme events, being able to predict what these events will look like will help to alleviate some of the potential damage. We demonstrated that the multilevel approach we considered and developed will directly reduce the computational cost of running our simulations in comparison to standard approaches, and we also discussed in §6.4.1 how we might further reduce the computational cost when moving to a two-dimensional system

Flooding due to precipitation can cause significant damage, but being able to accurately predict the level of flooding will help limit that damage and potentially prevent the loss of life. There is always more work to still be done, but we hope this thesis goes some way towards achieving that.

Bibliography

S. Abarbanel, D. Stanescu, and M. Y. Hussaini. Unsplit Variables Perfectly Matched Layers for the Shallow Water Equations with Coriolis Forces. *Computational Geosciences*, 7(4):275–294, Dec. 2003. ISSN 1420-0597, 1573-1499. doi: 10.1023/B:COMG.0000005245.72694.13. URL https://link-springer-com.ezproxy.sussex.ac.uk/article/10.1023/B:COMG.0000005245.72694.13.

E. Audusse, M. Bristeau, and B. Perthame. Kinetic schemes for Saint-Venant equations with source terms on unstructured grids. Technical Report RR-3989, INRIA, 2000.

O. Bennett and S. Hartwell-Naguib. Flood defence spending in England. *House of Commons Library*, 2014.

D. Bernoulli. *Danielis Bernoulli ... Hydrodynamica : sive De viribus et motibus fluidorum commentarii : Opus academicum ab auctore, dum Petropoli ageret, congestum.* Argentorati : sumptibus Johannis Reinholdi Dulseckeri : typis Joh. Henr. Deckeri, 1738., 1738. URL https://search.library.wisc.edu/catalog/999567710102121.

M. Besson and O. Lakkis. Finite volume code 1D Saint Venant. Sourceforge Library, August 2013. URL http://sourceforge.net/projects/finitevolumecode1dsaintvenant/.

F. Black and M. Scholes. The Pricing of Options and Corporate Liabilities. *Journal of Political Economy*, 81(3):637–654, 1973. doi: 10.1086/260062. URL https://doi.org/10.1086/260062.

C. Bourdarias, M. Ersoy, and S. Gerbi. A kinetic scheme for transient mixed flows in non uniform closed pipes: a global manner to upwind all the source terms. *J. Sci. Comput.*, 48(1-3):89–104, 2011. ISSN 0885-7474. doi: 10.1007/s10915-010-9456-0. URL http://dx.doi.org/10.1007/s10915-010-9456-0.

C. Bourdarias, M. Ersoy, and S. Gerbi. A model for unsteady mixed flows in non uniform closed water pipes: a Full Kinetic Approach. *Numer. Math.*, 128(2):217–263, 2014.

G. E. P. Box and M. E. Muller. A Note on the Generation of Random Normal Deviates. *Ann. Math. Statist.*, 29(2):610–611, 06 1958. doi: 10.1214/aoms/1177706645. URL http://dx.doi.org/10.1214/aoms/1177706645.

Z. Brzezniak and T. Zastawniak. *Basic stochastic processes*. Springer Undergraduate Mathematics Series. Springer-Verlag London, 1999. ISBN 978-1-4471-0533-6. doi: 10.1007/978-1-4471-0533-6.

CCRA. Climate Change Risk Assessment 2017. 2017.

P. Cowpertwait, D. Ocio, G. Collazos, O. de Cos, and C. Stocker. Regionalised spatiotemporal rainfall and temperature models for flood studies in the Basque Country, Spain. *Hydrology and Earth System Sciences*, 17(2):479–494, 2013. doi: 10.5194/hess-17-479-2013. URL https://www.hydrol-earth-syst-sci.net/17/479/2013/.

H. Darcy. Les fontaines publiques de la ville de Dijon. 1856.

G. A. M. de Almeida, P. Bates, J. E. Freer, and M. Souvignet. Improving the stability of a simple formulation of the shallow water equations for 2-d flood modeling. *Water Resources Research*, 48(5):n/a–n/a, 2012. ISSN 1944-7973. doi: 10.1029/2011WR011570. URL http://dx.doi.org/10.1029/2011WR011570. W05528.

A.-J.-C. B. de Saint-Venant. Théorie du mouvement non-permanent des eaux, avec application aux crues des rivières at à l'introduction des marées dans leur lit. *Comptes rendus hebdomadaires des séances de l'Académie des sciences*, 73:147–154, 1871. URL http://catalogue.bnf.fr/ark:/12148/cb343481087.

O. Delestre and F. James. SIMULATION OF RAINFALL EVENTS AND OVERLAND FLOW. 35:125–135, Sept. 2008. URL https://hal.archives-ouvertes.fr/hal-00426694.

O. Delestre, S. Cordier, F. James, and F. Darboux. Simulation of Rain-Water Overland-Flow. In J.-G. L. E. Tadmor and A. Tzavaras, editors, *12th International Conference on Hyperbolic Problems*, volume 67 of *Proceedings of Symposia in Applied Mathematics*, pages 537–546, College Park, United States, June 2008. American Mathematical Society. URL https://hal.archives-ouvertes.fr/hal-00343721.

O. Delestre, S. Cordier, F. Darboux, and F. James. A limitation of the hydrostatic reconstruction technique for shallow water equations. *Comptes Rendus Mathematique*, 350(13):677–681, 2012.

O. Delestre, F. Darboux, F. James, C. Lucas, C. Laguerre, and S. Cordier. FullSWOF: A free software package for the simulation of shallow water flows. *ArXiv e-prints*, Jan. 2014.

A. Delis and T. Katsaounis. Numerical solution of the two-dimensional shallow water equations by the application of relaxation methods. *Applied Mathematical Modelling*, 29(8):754 – 783, 2005. ISSN 0307-904X. doi: http://dx.doi.org/10.1016/j.apm.2004.11.001. URL http://www.sciencedirect.com/science/article/pii/S0307904X04001647.

J. Dupuit. Études théoriques et pratiques sur le mouvement des eaux dans les canaux découverts et a travers les terrains perméables avec des considérations relatives au régime des grandes eaux, au débouché a leur donner, et a la marche des alluvions dans les rivieres a fond mobile. 1863.

A. Einstein. Über die von der molekularkinetischen Theorie der Wärme geforderte Bewegung von in ruhenden Flüssigkeiten suspendierten Teilchen. *Annalen der Physik*, 322:549–560, 1905. doi: 10.1002/andp.19053220806.

M. Ersoy. A free surface model for incompressible pipe and open channel flow. Technical report, 2013. URL http://hal.archives-ouvertes.fr/hal-00908961.

M. Ersoy. Dimension reduction for incompressible pipe and open channel flow including friction. In *Conference Applications of Mathematics 2015, in honor of the 90th birthday of Ivo Babuška and 85th birthday of Milan Práger and Emil Vitásek* , pages 17–33, Prague, France, Nov. 2015. J. Brandts and S. Korotov and M. Krizek and K. Segeth and J. Sistek and T. Vejchodsky. URL https://hal.archives-ouvertes.fr/hal-00908961.

M. Esteves, X. Faucher, S. Galle, and M. Vauclin. Overland flow and infiltration modelling for small plots during unsteady rain: numerical results versus observed values. *Journal of hydrology*, 228(3):265–282, 2000.

P. Forchheimer. Über die Ergiebigkeit von Brunnen-Anlagen und Sickerschlitzen. *Z. Architekt. Ing.-Ver.*, 32:539–563, 1886.

J.-F. Gerbeau and B. Perthame. Derivation of viscous Saint-Venant system for laminar shallow water; numerical validation. *Discrete Cont. Dyn. Syst. Ser. B*, 1 (1):89–102, 2001.

M. Giles. Multi-level Monte Carlo path simulation. online preprint NA-06/03, Oxford University Computing Laboratory, Parks Road, Oxford, U.K., May 2006. URL http://people.maths.ox.ac.uk/gilesm/files/NA-06-03.pdf.

M. B. Giles. Multilevel Monte Carlo methods. *Acta Numerica*, 24:259–328, 2015.

M. B. Giles, F. Y. Kuo, I. H. Sloan, and B. J. Waterhouse. Quasi-Monte Carlo for finance applications. *ANZIAM J.*, 50(C):C308–C323, 2008. ISSN 1446-1811.

R. Grace and P. S. Eagleson. The modeling of overland flow. *Water Resources Research*, 2(3):393–403, 1966.

I. Graham, F. Kuo, J. Nichols, R. Scheichl, C. Schwab, and I. Sloan. Quasi-Monte Carlo finite element methods for elliptic PDEs with log-normal random coefficient. online preprint 2013-14, Seminar for Applied Mathematics, ETH Zürich, Switzerland, 2013. URL /sam_reports/reports_final/reports2013/2013-14.pdf.

I. G. Graham, F. Y. Kuo, D. Nuyens, R. Scheichl, and I. H. Sloan. Quasi-Monte Carlo methods for elliptic PDEs with random coefficients and applications. *J. Comput. Phys.*, 230(10):3668–3694, 2011. ISSN 0021-9991. doi: 10.1016/j.jcp.2011.01.023. URL http://dx.doi.org/10.1016/j.jcp.2011.01.023.

W. H. Green and G. A. Ampt. Studies in soil physics. Part I. The flow of air and water through soils. *The Journal of Agricultural Science*, 4:1–24, 1911.

A. Kebaier. Statistical Romberg extrapolation: A new variance reduction method and applications to option pricing. *Ann. Appl. Probab.*, 15(4):2681–2705, 11 2005. doi: 10.1214/105051605000000511. URL http://dx.doi.org/10.1214/105051605000000511.

F. C. Klebaner. *Introduction to Stochastic Calculus with Applications*. Imperial College Press, 2012.

P. E. Kloeden and E. Platen. *Numerical solution of stochastic differential equations*, volume 23 of *Applications of Mathematics (New York)*. Springer-Verlag, Berlin, corrected 3rd printing edition, 1999. ISBN 3-540-54062-8.

D. Kröner. *Numerical schemes for conservation laws*. Wiley, 1997.

C. Lawless. Constrained Random Walks, 2013. URL http://cnr.lwlss.net/ConstrainedRandomWalk/.

R. J. LeVeque. *Numerical methods for conservation laws*, volume 132. Springer, 1992.

R. J. LeVeque. *Finite volume methods for hyperbolic problems*. Cambridge Texts in Applied Mathematics. Cambridge University Press, Cambridge, 2002. ISBN 0-521-81087-6; 0-521-00924-3. doi: 10.1017/CBO9780511791253. URL http://dx.doi.org/10.1017/CBO9780511791253.

R. J. LeVeque, D. L. George, and M. J. Berger. Tsunami modelling with adaptively refined finite volume methods. *Acta Numerica*, 20:211–289, 2011. doi: 10.1017/S0962492911000043.

J. S. Liu. *Monte Carlo Strategies in Scientific Computing*. Springer Series in Statistic. Springer-Verlag New York, 2004. ISBN 978-0-387-76369-9. doi: 10.1007/978-0-387-76371-2.

G. J. Lord, C. E. Powell, and T. Shardlow. *An introduction to computational stochastic PDEs*. Number 50. Cambridge University Press, 2014.

T. Luo, A. Maddocks, C. Iceland, P. Ward, and H. Winsemius. World's 15 countries with the most people exposed to river floods, 2015. URL http://www.wri.org/blog/2015/03/world's-15-countries-most-people-exposed-river-floods.

R. C. Merton. Theory of Rational Option Pricing. *The Bell Journal of Economics and Management Science*, 4(1):141–183, 1973. ISSN 00058556. URL http://www.jstor.org/stable/3003143.

Met Office. UK climate - historic station data, 2017. URL http://www.metoffice.gov.uk/public/weather/climate-historic/.

S. Mishra, C. Schwab, and J. Šukys. Multilevel Monte Carlo Finite Volume Methods for Shallow Water Equations with Uncertain Topography in Multi-dimensions. *SIAM J. Sci. Comput.*, 34(6):761–784, 2012. URL https://doi.org/10.1137/110857295.

MLMC research. Multilevel Monte Carlo research. URL http://people.maths.ox.ac.uk/gilesm/mlmc_community.html.

MODFLOW. USGS MODFLOW and related programs. URL http://water.usgs.gov/ogw/modflow/.

H. Niederreiter. *Random Number Generation and Quasi-Monte Carlo Methods*. Society for Industrial and Applied Mathematics, Philadelphia, PA, USA, 1992. ISBN 0-89871-295-5.

C. Onof, R. E. Chandler, A. Kakou, P. Northrop, H. S. Wheater, and V. Isham. Rainfall modelling using Poisson-cluster processes: a review of developments. *Stochastic Environmental Research and Risk Assessment*, 14(6):384–411, 2000. URL http://link.springer.com/article/10.1007/s004770000043.

B. Perthame and C. Simeoni. A kinetic scheme for the Saint-Venant system with a source term. *Calcolo*, 38(4):201–231, 2001.

S. Priestley and T. Rutherford. Flood risk management and funding. *House of Commons Library*, 2017.

L. A. Richards. Capillary conduction of liquids through porous mediums. *Physics*, 1 (5):318–333, 1931. doi: 10.1063/1.1745010. URL http://dx.doi.org/10.1063/1.1745010.

M. Rousseau, O. Cerdan, A. Ern, O. Le Maitre, and P. Sochala. Study of overland flow with uncertain infiltration using stochastic tools. *Advances in Water Resources*, 38:1–12, 2012.

P. Sayers, M. Horritt, E. Penning-Rowsell, and A. McKenzie. Climate Change Risk Assessment 2017: Projections of future flood risk in the UK. 2015.

J. Singh, M. S. Altinakar, and Y. Ding. Numerical modeling of rainfall-generated overland flow using nonlinear shallow-water equations. *Journal of Hydrologic Engineering*, 20(8), 2015. doi: 10.1061/(ASCE)HE.1943-5584.0001124. URL https://ascelibrary.org/doi/abs/10.1061/.

P. Sochala. *Numerical methods for subsurface flows and coupling with surface runoff*. PhD thesis, Ecole des Ponts ParisTech, 2008.

R. Srikanthan and T. A. McMahon. Stochastic generation of annual, monthly and daily climate data: A review. *Hydrology and Earth System Sciences Discussions*, 5(4):653–670, 2001. URL https://hal.archives-ouvertes.fr/hal-00304639.

E. F. Toro. *Riemann solvers and numerical methods for fluid dynamics: a practical introduction*. Springer Science & Business Media, 2009.

M. von Smoluchowski. Zur kinetischen Theorie der Brownschen Molekularbewegung und der Suspensionen. *Annalen der Physik*, 326(14):756–780, 1906. ISSN 1521-3889. doi: 10.1002/andp.19063261405. URL http://dx.doi.org/10.1002/andp.19063261405.

S. Weill, E. Mouche, and J. Patin. A generalized Richards equation for surface/subsurface flow modelling. *Journal of Hydrology*, 366(1):9–20, 2009.

D. A. Woolhiser and J. A. Liggett. Unsteady, one-dimensional flow over a plane – the rising hydrograph. *Water Resources Research*, 3(3):753–771, 1967.

K. Xu. A well-balanced gas-kinetic scheme for the shallow-water equations with source terms. *Journal of Computational Physics*, 178(2):533 – 562, 2002. ISSN 0021-9991. doi: https://doi.org/10.1006/jcph.2002.7040. URL http://www.sciencedirect.com/science/article/pii/S0021999102970403.

W. Zhang and T. W. Cundy. Modeling of two-dimensional overland flow. *Water Resources Research*, 25(9):2019–2035, 1989. ISSN 1944-7973. doi: 10.1029/WR025i009p02019. URL http://dx.doi.org/10.1029/WR025i009p02019.

B. Øksendal. *Stochastic Differential Equations*. Springer-Verlag Berlin Heidelberg, 2003. ISBN 978-3-642-14394-6. doi: 10.1007/978-3-642-14394-6.